

TURBULENT BOUNDARY LAYERS AND  
SEDIMENT SUSPENSION ABSENT MEAN  
FLOW-INDUCED SHEAR

A Dissertation

Presented to the Faculty of the Graduate School

of Cornell University

in Partial Fulfillment of the Requirements for the Degree of

Doctor of Philosophy

by

Blair Anne Johnson

August 2016

© 2016 Blair Anne Johnson  
ALL RIGHTS RESERVED

TURBULENT BOUNDARY LAYERS AND SEDIMENT SUSPENSION  
ABSENT MEAN FLOW-INDUCED SHEAR

Blair Anne Johnson, Ph.D.

Cornell University 2016

We perform an experimental study to investigate turbulent boundary layers in the absence of mean shear at both stationary solid and mobile sediment boundaries. High Reynolds number ( $Re_\lambda \sim 300$ ) horizontally homogeneous isotropic turbulence is generated via randomly actuated synthetic jet arrays (RASJA - Variano & Cowen 2008). Each of the arrays is controlled by a spatio-temporally varying algorithm, which in turn minimizes the formation of secondary flows or mean shear. One array consists of an  $8 \times 8$  grid of jets, while the other is a  $16 \times 16$  array. By varying the operational parameters of the RASJA, we also find that we are able to control the turbulence levels, including integral length scales and dissipation rates, by changing the mean on-times in the jet algorithm.

Acoustic Doppler velocimetry (ADV) and particle image velocimetry (PIV) measurements are used to study the isotropic turbulent region and the boundary layer formed beneath it as the turbulence encounters the bottom boundary. Time-lapsed photography is used to monitor large-scale bed morphology of the sediment. The flow is characterized by statistical metrics including the mean flow and turbulent velocities, turbulent kinetic energy, temporal spectra, integral scales of the turbulence, and terms in the turbulent kinetic energy transport equation including energy dissipation rates, production, and turbulent transport. We evaluate the implications of assuming isotropy in computing dissipation by comparing several methods commonly used in measurements, includ-

ing second-order structure functions, spatial spectra, scaling arguments, and direct computations. With our dissipation results, we calculate the empirical constant in the Tennekes (1975) model of Eulerian frequency spectra. This model allows for the determination of dissipation from temporally resolved single-point velocity measurements when there is no mean flow.

We compare our boundary layer characterizations to prior literature that addresses mean shear free turbulent boundary layers via grid-stirred tank (GST) experiments, moving bed experiments, rapid distortion theory (RDT), and direct numerical simulations (DNS) in a forced turbulent box. We draw comparisons between an impermeable flat boundary, a flat permeable sediment boundary, and a rippled sediment boundary. In experiments examining turbulence above a sediment boundary, we observe sediment suspension primarily via vortical pick-up and splats. Additionally, we observe the development of ripple patterns in the sediment, which is unexpected in a facility absent mean shear or oscillations. We find a relationship between the integral length scale of the turbulent flow with the ripple spacing, suggesting a link between the turbulence levels and sediment transport. Because traditional viscous stresses due to mean velocity gradients suggest no bed friction or sediment transport, we develop a method for considering Reynolds stresses over short time periods as a surrogate for understanding the importance of bed stress in a zero mean shear environment.

## BIOGRAPHICAL SKETCH

The author was raised in Kingsville, MD, with many summer trips to the beach in Ocean City. At the beach, she often played with her sisters in the swash zone, the region of the beach that is continually covered and uncovered by wave runup. She studied the waves carefully to identify the perfect location to build drip castles, which require enough runup to fill a small pool of water to have a constant supply of fluidized sand, but not so much runup to wash the castle to oblivion.

Little could she imagine how significant these preliminary field experiments would become many years later, when she moved to Ithaca, NY, to study swash-inspired turbulence and sediment transport in the DeFrees Hydraulic Laboratory at Cornell University. She has enjoyed opportunities to travel during graduate school, including a research “sabbatical” at IH Cantabria in Santander, Spain, a brief English teaching position in Pasto, Colombia, and workshops and conferences galore. She cherishes her time conducting research and teaching during graduate school and, at the time of writing, is thrilled to see what awaits in the world of academia beyond Cornell.

This dissertation is dedicated to the students who have yet to embark on a path through academia. May you find many mentors, role models, and supporters in unexpected places to guide you on your way.

## ACKNOWLEDGEMENTS

There are not enough pages to describe the impact my colleagues, friends, and family have had on my experiences in graduate school. My parents, sisters, and brothers-in-law have encouraged me from day one by helping me to find my passions and to excel at them. I am grateful to my college advisor, Tony Dalrymple, for motivating me to pursue this field and for continuing to provide guidance and support.

Cornell's EFMH group is truly unique, as we inspire each other to grow as conscientious citizens as well as scientists and engineers. I feel lucky and honored to have worked with such a fantastic group. My lab mates PJ Rusello and Rafael Tinoco taught me most of what I know in the laboratory and have provided career guidance on countless occasions. I am also grateful to PJ for introducing me to outrigger canoeing. Allie King and Seth Schweitzer have provided support and companionship, in addition to teaching me how fascinating lake dynamics can be. Evan Variano, my predecessor, has entertained and fostered many conversations about turbulence and working with jet arrays. I have had the opportunity to mentor three undergraduate women - Zoe Shiveley, Claire DeVoe, and Bonnie Powell. Each of them has helped tremendously in the lab and with data analysis, and I am grateful for their curiosity and creativity.

I have discussed many life philosophies behind the door of Hollister 114 with Jose Maria Gonzales Ondina, Pato Winckler, Nimish Pujara, Mahmoud Sadek, Qi Zhou, Sumedh Joshi, Veronica Citerone, Vicki List, Diego Muriel, Gustavo Rivera, Ignacio Sepulveda, and others. A huge thanks to Jorge Escobar-Vargas for routinely sharing his theories on the conspiracy of the universe and for being a constant support system.

In the laboratory and tool shop, Paul Charles and Tim Brock have taught

me many lessons about design, construction, and materials. I am grateful for Paul's dedication to my project and for spending so much time learning about Arduino programming and circuit board design, among other tasks. Cameron Willkens has solved dozens of computer and technical problems, one of which included drilling through an external hard drive to allow communication between new and ancient devices. Thanks also to Francois Guimbretiere, who was instrumental in designing the electronics of the new jet array.

I have had constant support by my committee members Jim Jenkins and Michel Louge, who have opened my eyes to the complexity of sediment transport. Peter Diamessis and Zellman Warhaft have also provided stimulating turbulence chats and life guidance as I continue to navigate academia.

I could not have asked for a more supportive or motivating advisor than I found in Todd Cowen. His unstoppable energy and ability to turn any situation into a positive learning experience has helped me keep things in perspective and continue to see the light at the end of the tunnel. I will be forever grateful for the dedication, patience, and care with which he has treated me as an advisee.

I am thankful for the research funding provided by the CBET Division of Chemical, Bioengineering, Environmental, and Transport Systems of the U.S. National Science Foundation (Award #1233842). The DeFrees Family Fellowship has supported me for several years, and the Cornell Graduate School has provided many conference and travel grants.

And finally, I thank my fiance, Andrew Waxman. He never lost confidence in me even when I wanted to throw in the towel at times. I am grateful for his enthusiasm for PIV and laser safety, and for keeping me company during late experiments in the lab. More than anything he has helped me to always put my best foot forward and inspired me to succeed.

# CONTENTS

Biographical Sketch . . . . .	iii
Dedication . . . . .	iv
Acknowledgements . . . . .	v
Contents . . . . .	vii
List of Figures . . . . .	x
List of Tables . . . . .	xvi
<b>1 Introduction</b>	<b>1</b>
1.1 Motivation . . . . .	1
1.2 Background . . . . .	2
1.2.1 Turbulence Absent Mean Shear . . . . .	2
1.2.2 Sediment Suspension . . . . .	5
1.3 Research Objectives . . . . .	8
<b>2 Experimental Facility</b>	<b>11</b>
2.1 Apparatus . . . . .	11
2.1.1 8 x 8 RASJA . . . . .	13
2.1.2 16 x 16 RASJA . . . . .	15
2.1.3 Jet-Monitoring System . . . . .	18
2.2 Measurement Techniques . . . . .	20
2.2.1 Acoustic Doppler Velocimetry . . . . .	20
2.2.2 Particle Image Velocimetry . . . . .	23
2.2.3 Time-Lapsed Photography . . . . .	34
<b>3 Exploration of the RASJA Algorithm to Control Turbulence</b>	<b>36</b>
3.1 Mean and Fluctuating Velocities . . . . .	37
3.1.1 8 x 8 RASJA . . . . .	37
3.1.2 16 x 16 RASJA . . . . .	42
3.2 Turbulent Kinetic Energy . . . . .	43
3.2.1 8 x 8 RASJA . . . . .	44
3.2.2 16 x 16 RASJA . . . . .	46
3.3 Integral Scales . . . . .	47
3.3.1 Integral Length Scale - Exponential Curve Fit . . . . .	47
3.3.2 Integral Length Scale - Bessel Function . . . . .	50
3.3.3 Integral Length Scale - Scaling Law . . . . .	51
3.3.4 Integral Length Scale Results . . . . .	52
3.3.5 Integral Time Scale - Autocorrelation . . . . .	54
3.3.6 Integral Time Scale - Scaling . . . . .	54
3.4 Structure of Turbulence Facility . . . . .	57
3.4.1 Boundary Layer and Tank Structure . . . . .	57
3.4.2 Decay of Turbulence away from the Source . . . . .	60

<b>4</b>	<b>Turbulent Kinetic Energy Balance</b>	<b>63</b>
4.1	Dissipation . . . . .	64
4.1.1	Scaling Law . . . . .	64
4.1.2	Second-Order Structure Function . . . . .	64
4.1.3	Direct Method . . . . .	66
4.1.4	Spatial Spectra . . . . .	67
4.1.5	Eulerian Frequency Spectra . . . . .	69
4.2	Production . . . . .	73
4.3	Turbulent Transport . . . . .	76
4.4	Advection . . . . .	77
4.5	Viscous Transport . . . . .	77
4.6	Pressure Diffusion . . . . .	78
4.7	Turbulence Statistics . . . . .	78
<b>5</b>	<b>Boundary Layer Results - Solid Boundary</b>	<b>82</b>
5.1	Fluctuating Velocities and Turbulent Kinetic Energy . . . . .	82
5.1.1	8 x 8 RASJA . . . . .	84
5.1.2	16 x 16 RASJA . . . . .	86
5.2	Integral Length Scale . . . . .	88
5.3	Dissipation Comparisons with RDT . . . . .	90
<b>6</b>	<b>Sediment Dynamics</b>	<b>95</b>
6.1	Bed Stress Analysis . . . . .	96
6.1.1	Viscous vs. Reynolds Stresses . . . . .	96
6.1.2	Short Time Scale Analysis . . . . .	96
6.2	Mechanisms of Sediment Suspension . . . . .	101
6.3	Ripple Dynamics . . . . .	104
6.3.1	Development of Ripples . . . . .	105
6.3.2	Ripple Spacing . . . . .	109
6.3.3	Additional Comments on Bedforms . . . . .	109
<b>7</b>	<b>Boundary Layer Results - Sediment Boundary</b>	<b>112</b>
7.1	Fluctuating Velocities and Turbulent Kinetic Energy . . . . .	113
7.1.1	Flat Sediment Boundary - 8 x 8 RASJA . . . . .	113
7.1.2	Rippled Sediment Boundary - 8 x 8 RASJA . . . . .	114
7.1.3	Smooth Sediment Boundary - 16 x 16 RASJA . . . . .	114
7.2	Dissipation . . . . .	117
7.2.1	Sediment Boundary - 8 x 8 RASJA . . . . .	117
7.2.2	Sediment Boundary - 16 x 16 RASJA . . . . .	118
7.3	Integral Length Scale . . . . .	119
<b>8</b>	<b>Conclusions</b>	<b>122</b>
8.1	Summary . . . . .	122
8.2	Future Directions . . . . .	125

<b>Appendix A - RASJA Operating Codes</b>	<b>128</b>
<b>Appendix B - Median Smoothing Filter</b>	<b>155</b>
<b>Bibliography</b>	<b>157</b>

## LIST OF FIGURES

1.1	Boundary layer definitions and setup used in rapid distortion theory. Image reproduced from Hunt & Graham (1978). . . . .	5
1.2	Shields curve, reproduced from van Rijn (1984). . . . .	6
2.1	Schematic drawing of the turbulence facility with the 8 x 8 RASJA suspended above a glass bed. . . . .	12
2.2	Photo of tank with 8 x 8 RASJA. . . . .	14
2.3	Photo of jet mountings for 8 x 8 RASJA. . . . .	14
2.4	Photo of inline jet array for 16 x 16 RASJA. . . . .	16
2.5	Design of pump control circuit board for 16 x 16 RASJA. . . . .	17
2.6	Design of circuit "quad" board to integrate Arduino controls on existing 8x8 RASJA control boards. . . . .	18
2.7	Photo of 8 x 8 RASJA monitor circuit board. . . . .	19
2.8	Design of monitor circuit board. . . . .	19
2.9	Temporal spectra from ADV measurements at $z = 12.0$ cm above the bed. $S_{uu}$ (X), $S_{vv}$ (.), $S_{uww}$ (O). $T_{on} = 4$ s, $\Phi_{on} = 6.25\%$ , 8 x 8 RASJA. . . . .	22
2.10	Timing code of mirror scan (solid line), shutter (dotted line), and integration time of first image collected by Bobcat camera (dashed line). . . . .	24
2.11	Image of ruler for spatial calibration of PIV images. Colorbar represents image intensity, out of a maximum of 4095. . . . .	27
2.12	Profiles of invalid vector counts as a function of $\Delta T$ . 4 ms (+), 5 ms (o); 6 ms (x); 7 ms ( $\triangleleft$ ); 8 ms ( $\star$ ); 9 ms ( $\square$ ); 10 ms (*). . . . .	28
2.13	Turbulent kinetic energy profiles as a function of $\Delta T$ . See previous figure for legend. . . . .	29
2.14	Sample background image computed for 1 minute of data, $\Phi_{on} = 6.25\%$ , $T_{on} = 3$ s, zoomed to bottom 25% of image. Intensities up to 1000 are shown, out of possible maximum saturation illumination of 4095. . . . .	30
2.15	Superposition of mask onto sample background image (same as in previous figure). Black points denote bed location at illuminated ripple crests; white points denote interpolated bed location in shadowed regions. . . . .	31
2.16	Sample profiles of cumulative filtering methods: unconverged vector removal (O), AGW filter (+), local median filter ( $\triangleright$ ). 16 x 16 RASJA, $\Phi_{on} = 3.1\%$ , $T_{on} = 0.8$ s. . . . .	33
2.17	Ripple evolution observed at initial state, then 15 minutes, 30 minutes, 1 hour, 2 hours, 4 hours, 8 hours, and 12 hours into turbulence generation above an initially flat bed. $T_{on} = 3$ s, $\Phi_{on} = 12.5\%$ , 8 x 8 RASJA. . . . .	35

3.1	Temporally averaged flows $\langle U \rangle$ (left) and $\langle W \rangle$ (right). Colorbar denotes velocity in cm/s. $T_{on} = 4$ s, $\Phi_{on} = 6.25\%$ , 8 x 8 RASJA. . . . .	39
3.2	Dependence of $u'$ and $w'$ on $T_{on} = 4$ s ( $u' = +$ , $w' = \diamond$ ), 6 s ( $u' = \star$ , $w' = \star$ ), 8 s ( $u' = \triangleright$ , $w' = \triangleleft$ ) for $\Phi_{on} = 6.25\%$ (left) and $\Phi_{on} = 6.25\%$ ( $u' = +$ , $w' = \square$ ), 7.7% ( $u' = \star$ , $w' = \circ$ ), 9.1% ( $u' = *$ , $w' = \diamond$ ), 10.5% ( $u' = \triangleright$ , $w' = \star$ ), 12.5% ( $u' = \times$ , $w' = \triangle$ ) for $T_{on} = 4$ s (right); 8 x 8 RASJA. . . . .	40
3.3	Dependence of $u'$ and $w'$ on $T_{on} = 0.8$ s ( $u' = *$ , $w' = \square$ ), $T_{on} = 1.0$ s ( $u' = \times$ , $w' = \circ$ ), $T_{on} = 1.2$ s ( $u' = +$ , $w' = \diamond$ ), $T_{on} = 1.4$ s ( $u' = \nabla$ , $w' = \triangle$ ), $T_{on} = 1.6$ s ( $u' = \star$ , $w' = \star$ ). $\Phi_{on} = 3.1\%$ , 16 x 16 RASJA. . . . .	42
3.4	Turbulent kinetic energy profiles for $\Phi_{on} = 6.25\%$ , $T_{on} = 4$ s (+), 6 s ( $\star$ ), 8 s ( $\triangleright$ ), 8 x 8 RASJA. . . . .	44
3.5	Turbulent kinetic energy profiles for $\Phi_{on} = 3.1\%$ , $T_{on} = 0.8$ s (*), 1.0 s (x), 1.2 s (+); 1.4 s ( $\nabla$ ), 1.6 s ( $\star$ ). 16 x 16 RASJA. . . . .	46
3.6	Exponential curve fit to autocorrelation function $a_{11,1}$ (*). $T_{on} = 4$ s, $\Phi_{on} = 6.25\%$ , $z = 13.02$ cm, 8 x 8 RASJA. . . . .	48
3.7	Fit of spatial transverse autocorrelation data $a_{33,1}(r)$ ( $\circ$ ) to model fit. Sample data for $T_{on} = 4$ s, $\Phi_{on} = 6.25\%$ , $z = 13.02$ cm, 8 x 8 RASJA. . . . .	49
3.8	Profiles of $\mathcal{L}_L$ (*) and $\mathcal{L}_T$ ( $\circ$ ) with 95% confidence intervals for $T_{on} = 4$ s, $\Phi_{on} = 6.25\%$ , 8 x 8 RASJA. . . . .	49
3.9	Bessel function (solid line) and exponential curve fit (dash-dotted line) to autocorrelation function $a_{11,1}$ (*). $T_{on} = 4$ s, $\Phi_{on} = 6.25\%$ , $z = 13.02$ cm, 8 x 8 RASJA. . . . .	51
3.10	Integral length scale profile comparison between Bessel function and exponential curve fit. . . . .	51
3.11	Sample temporal autocorrelation function from ADV data; 9 ensemble averages. . . . .	55
3.12	Sample temporal autocorrelation function from ADV data; 99 ensemble averages. . . . .	55
3.13	Comparison of experimental $u'$ data. $T_{on} = 4$ s, $\Phi_{on} = 6.25\%$ , 8 x 8 RASJA (*), $T_{on} = 0.8$ s, $\Phi_{on} = 3.1\%$ , 16 x 16 RASJA (x) with Brumley & Jirka (1987) GST data ( $\square$ ), Hopfinger & Toly (1976, dash-dot), and Hunt & Graham (dashed line). Vertical axis normalized by jet height $H = 71$ cm and $H = 65$ cm for 8 x 8 and 16 x 16 RASJAs, respectively; horizontal axis normalized to average 1 at $\frac{z}{H} = 24\%$ , as in Brumley & Jirka (1987). . . . .	61
3.14	Profiles of experimental $w'$ data. $T_{on} = 4$ s, $\Phi_{on} = 6.25\%$ , 8 x 8 RASJA ( $\diamond$ ), $T_{on} = 0.8$ s, $\Phi_{on} = 3.1\%$ , 16 x 16 RASJA (+). See previous figure for legend of remaining data. . . . .	62

4.1	Turbulent kinetic energy balance in a turbulent boundary layer driven by a mean flow on a flat plate, normalized by $2k$ , reproduced from Spalart (1988). Dissipation (dash-dotted line), production (o-), turbulent diffusion (solid line), viscous diffusion (dashed line), pressure (dotted line). . . . .	64
4.2	Second-order structure functions $D_{LL}$ (*) and $D_{NN}$ (○) plotted against $2/3$ slope. $T_{on} = 4s$ , $\Phi_{on} = 6.25\%$ , $z=10.45cm$ , $8 \times 8$ RASJA. . . . .	65
4.3	Compensated one-side spatial spectra. $G_{uu}$ (*), $G_{ww}$ (○). Example for $T_{on} = 4s$ , $\Phi_{on} = 6.25\%$ , $8 \times 8$ RASJA. . . . .	69
4.4	Increase in dissipation estimate resulting from interpolating in data via Delaunay triangulation. Profiles are normalized by un-interpolated data via the same method (i.e. $D_{LL}$ ratio is $D_{LL}$ (interpolated) to $D_{LL}$ (un-interpolated)). $D_{LL}$ (*), $D_{NN}$ (o), direct method (x). Sample profiles shown for $T_{on} = 4s$ , $\Phi_{on} = 6.25\%$ , $8 \times 8$ RASJA. . . . .	70
4.5	Method comparison of dissipation profiles. Scaling law (square), $D_{LL}$ (*), $D_{NN}$ (o), direct method (x), $S_{uu}$ (+), $S_{ww}$ (◇). Sample profiles shown for $T_{on} = 4s$ , $\Phi_{on} = 6.25\%$ , $8 \times 8$ RASJA. . . . .	70
4.6	Frequency spectra from 100 Hz ADV measurement at $z = 12$ cm, 200 ensemble averages. $T_{on} = 4s$ , $\Phi_{on} = 6.25\%$ , $8 \times 8$ RASJA. . . . .	71
4.7	Eulerian frequency spectrum of vertical velocity from 100 Hz ADV measurement at $z = 12$ cm, 80 ensemble averages. $T_{on} = 4s$ , $\Phi_{on} = 6.25\%$ , $8 \times 8$ RASJA. . . . .	72
4.8	Profiles of $\overline{u_i u_j}$ terms in the production equation. $\overline{uu}$ (+), $\overline{uw}$ (o), $\overline{ww}$ (◇) $T_{on} = 4s$ , $\Phi_{on} = 6.25\%$ , $8 \times 8$ RASJA. . . . .	74
4.9	Contributions from mean velocity gradients in the production equation. $\frac{\partial \langle U \rangle}{\partial x}$ (□), $\frac{\partial \langle U \rangle}{\partial z}$ (o), $\frac{\partial \langle W \rangle}{\partial x}$ (+), $\frac{\partial \langle W \rangle}{\partial z}$ (x). $T_{on} = 4s$ , $\Phi_{on} = 6.25\%$ , $8 \times 8$ RASJA. . . . .	74
4.10	Sample profile for which production contributes minimally to turbulent kinetic energy balance. $T_{on} = 4s$ , $\Phi_{on} = 6.25\%$ , $8 \times 8$ RASJA. . . . .	75
4.11	Sample profile for which production is not negligible. $T_{on} = 4s$ , $\Phi_{on} = 7.7\%$ , $8 \times 8$ RASJA. . . . .	75
4.12	Contributions of triple correlation terms, $\frac{\partial \overline{u_j u_i u_i}}{\partial x_i}$ , to turbulent transport. $T_{on} = 4s$ , $\Phi_{on} = 6.25\%$ , $8 \times 8$ RASJA. . . . .	76
4.13	Production, advection, and viscous transport, normalized by median production, for $T_{on} = 4s$ , $\Phi_{on} = 6.25\%$ . . . . .	77
4.14	Dissipation (☆), Triple correlations (median-filtered for smoothing, ◇), Production (median-filtered for smoothing, *), and estimated Pressure (□). Non-dimensionalized by $\epsilon_m$ from direct method. $T_{on} = 4s$ , $\Phi_{on} = 6.25\%$ , $8 \times 8$ RASJA. . . . .	79

5.1	Comparison of $u'/u'_m, w'/w'_m$ with Hunt & Graham (1978) inviscid theory and Thomas & Hancock (1977) experimental moving bed data at $x/M = 25$ (●), $x/M = 13$ (▲). Present cases are for $\Phi_{on} = 6.25\%$ and $T_{on} = 4$ s (☆, ◇), 6 s (+, ★), 8 s (X, □) . . . . .	85
5.2	Viscous (-) and source (-) regions of $u'/u'_m$ . See previous figure for legend. . . . .	85
5.3	Comparison of $k/k_m$ with Hunt & Graham (1978) inviscid theory. See figure 5.1 for legend. . . . .	86
5.4	Comparison of $u'/u'_m, w'/w'_m$ with Hunt & Graham (1978) inviscid theory and Thomas & Hancock (1977) experimental moving bed data at $x/M = 25$ (●), $x/M = 13$ (▲). Present cases are for $\Phi_{on} = 3.1\%$ and $T_{on} = 0.8$ s (*, □), 1.0 s (X, ○), 1.2 s (☆, ◇), 1.4 s (∇, △), 1.6 s (+, ★). 16 x 16 RASJA. . . . .	87
5.5	Viscous (-) and source (-) regions of $u'/u'_m$ . See previous figure for legend. . . . .	87
5.6	Comparison of $k/k_m$ with Hunt & Graham (1978) inviscid theory. See figure 5.4 for legend. . . . .	88
5.7	Longitudinal integral length scale comparison with Hunt & Graham (1978) and Thomas & Hancock (1977) Present cases are for $\Phi_{on} = 6.25\%$ and $T_{on} = 4$ s (☆), 6 s (+), 8 s (x). 8 x 8 RASJA. . . . .	89
5.8	Longitudinal integral length scale comparison with Hunt & Graham (1978) and Thomas & Hancock (1977) Present cases are for $\Phi_{on} = 3.1\%$ and $T_{on} = 0.8$ s (*), 1.0 s (x), 1.2 s (☆), 1.4 s (∇), 1.6 s (+). 16 x 16 RASJA. . . . .	89
5.9	Transverse integral length scale comparison with Thomas & Hancock (1977). 8 x 8 RASJA. See figure 5.7 for legend. . . . .	90
5.10	Transverse integral length scale comparison with Thomas & Hancock (1977). 16 x 16 RASJA. See figure 5.8 for legend. . . . .	90
5.11	$\epsilon_{11}$ comparison to Teixeira & Belcher (2000) (solid line - $\frac{\sqrt{kt}}{\mathcal{L}^*} = 0$ , viscous; dash-dot - $\frac{\sqrt{kt}}{\mathcal{L}^*} = 0.10$ ), Perot & Moin (1995b) (dots - $\frac{\sqrt{kt}}{\mathcal{L}^*} = 2.0$ , $Re^*=134$ ) (x - 8 x 8, ○ - 16 x 16). . . . .	92
5.12	$\epsilon_{33}$ comparison to Teixeira & Belcher (2000) (solid line - $\frac{\sqrt{kt}}{\mathcal{L}^*} = 0$ ; dash-dot - $\frac{\sqrt{kt}}{\mathcal{L}^*} = 0.10$ ), Perot & Moin (1995b) (dots - $\frac{\sqrt{kt}}{\mathcal{L}^*} = 2.0$ , $Re^*=134$ ) (+ - 8 x 8, □ - 16 x 16). . . . .	92
5.13	Comparison of total dissipation profiles between 8 x 8 RASJA (*) and 16 x 16 RASJA (□). . . . .	93
6.1	Maximum magnitude of production obtained with varying time intervals. . . . .	97
6.2	Histogram of $\tau_v$ (at 7 s intervals) measured at $z = 3$ mm. $\Phi_{on} = 6.25\%$ , $T_{on} = 4$ s, 8 x 8 RASJA. . . . .	98

6.3	Magnitude of maximum $\overline{uw}$ computed over 7 second increments. $\Phi_{on} = 6.25\%$ , $T_{on} = 4$ s, 8 x 8 RASJA. . . . .	99
6.4	Histogram of $\tau_{Re}$ (at 7 s intervals) measured at $z = 1$ cm. $\Phi_{on} = 6.25\%$ , $T_{on} = 4$ s, 8 x 8 RASJA. . . . .	99
6.5	Image of sediment suspension generated by bed-attached sand vortices. $\Phi_{on} = 3.1\%$ , $T_{on} = 1.6$ s, 16 x 16 RASJA. . . . .	102
6.6	Image of sediment transport in a turbulent splat. $\Phi_{on} = 3.1\%$ , $T_{on} = 1.6$ s, 16 x 16 RASJA. . . . .	103
6.7	Evolution of a cloud of suspended sediment. Each panel, from left to right, shows the progression of the sediment cloud at 1 s intervals. $\Phi_{on} = 3.1\%$ , $T_{on} = 1.6$ s, 16 x 16 RASJA. . . . .	105
6.8	Resulting sand ripples after 12 hours. $\Phi_{on} = 6.25\%$ , $T_{on} = 4$ s, 8 x 8 RASJA. . . . .	106
6.9	Resulting sand ripples after 6 hours. $\Phi_{on} = 3.15\%$ , $T_{on} = 0.8$ s, 16 x 16 RASJA. . . . .	108
6.10	Relationship between sand ripple spacing and integral length scale. (*) denotes tests with 8 x 8 RASJA; (o) denotes tests with 16 x 16 RASJA. . . . .	110
7.1	Profiles of $u'$ and $w'$ above solid (*, $\circ$ ), flat sediment (x, $\diamond$ ), and rippled sediment (+, $\square$ ) boundaries. $\Phi_{on} = 6.25\%$ , $T_{on} = 4$ s, 8 x 8 RASJA. . . . .	114
7.2	Profiles of $k$ above solid (*), flat sediment (x), and rippled sediment (+) boundaries. $\Phi_{on} = 6.25\%$ , $T_{on} = 4$ s, 8 x 8 RASJA. . . . .	115
7.3	Profiles of $u'$ and $w'$ above solid (*, o) and sediment (x, $\diamond$ ) boundaries. $\Phi_{on} = 3.1\%$ , $T_{on} = 0.8$ s, 16 x 16 RASJA. . . . .	116
7.4	Profiles of $k$ above solid (*) and sediment (x) boundaries. $\Phi_{on} = 3.1\%$ , $T_{on} = 0.8$ s, 16 x 16 RASJA. . . . .	116
7.5	Spatial spectra comparison above solid and sediment boundaries. glass, $G_{uu}$ - solid line; glass, $G_{ww}$ - dashed line; sand, $G_{uu}$ - dash-dotted line; sand, $G_{ww}$ - dotted line. $z = 11.9$ cm. $\Phi_{on} = 3.1\%$ , $T_{on} = 0.8$ s, 16 x 16 RASJA. . . . .	117
7.6	Spatial spectra comparison above solid and sediment boundaries. glass, $G_{uu}$ - solid line; glass, $G_{ww}$ - dashed line; sand, $G_{uu}$ - dash-dotted line; sand, $G_{ww}$ - dotted line. $z = 4.0$ cm. $\Phi_{on} = 3.1\%$ , $T_{on} = 0.8$ s, 16 x 16 RASJA. . . . .	118
7.7	Profiles of dissipation above solid (*), flat sediment (x), and rippled sediment (o) boundaries. Figure on left shows results for $\Phi_{on} = 6.25\%$ , $T_{on} = 4$ s, 8 x 8 RASJA. Figure on right shows results for $\Phi_{on} = 6.25\%$ , $T_{on} = 8$ s, 8 x 8 RASJA. . . . .	119
7.8	Dissipation profiles above solid (*) and sediment (o) boundaries. $\Phi_{on} = 3.1\%$ , $T_{on} = 0.8$ s, 16 x 16 RASJA. . . . .	120

7.9 Profiles of longitudinal integral length scale above solid (\*), flat sediment (x), and rippled sediment (o) boundaries. Figure on left shows results for  $\Phi_{on} = 6.25\%$ ,  $T_{on} = 4$  s, 8 x 8 RASJA. Figure on right shows results for  $\Phi_{on} = 6.25\%$ ,  $T_{on} = 8$  s, 8 x 8 RASJA. . . 121

## LIST OF TABLES

2.1	Sand grain distribution analysis. . . . .	11
2.2	Sample RASJA control parameters. . . . .	15
3.1	Mean flows in the 8 x 8 RASJA. All values shown are the mean value of the statistic in the mixed region from PIV data. . . . .	38
3.2	Secondary flows in the 8 x 8 RASJA. All values shown are the mean value of the statistic in the mixed region from PIV data. . . . .	41
3.3	Mean flows in the 16 x 16 RASJA. All values shown are the mean value of the statistic in the mixed region from PIV data. . . . .	43
3.4	Secondary flows in the 8 x 8 RASJA. All values shown are the mean value of the statistic in the mixed region from PIV data. . . . .	43
3.5	Turbulent (RMS) velocities and turbulent kinetic energy. All values shown are the mean value of the statistic in the mixed region from PIV data. 8 x 8 RASJA. . . . .	45
3.6	Turbulent (RMS) velocities and turbulent kinetic energy. All values shown are the mean value of the statistic in the mixed region from PIV data. 16 x 16 RASJA. . . . .	46
3.7	Integral length scale results, 8 x 8 RASJA. . . . .	53
3.8	Integral length scale results, 16 x 16 RASJA. . . . .	53
3.9	Resulting $T_{int}$ based on varying ensemble averaging intervals. Note: * denotes that $r(t)$ did not cross zero, so the integral was taken to the minimum of $r(t)$ . . . . .	55
3.10	Integral time scale results, 8 x 8 RASJA. . . . .	56
3.11	Integral time scale result, 16 x 16 RASJA. . . . .	56
4.1	Resulting dissipation values computed from various methods, averaged in the mixed region, 8 x 8 RASJA. . . . .	68
4.2	Kolmogorov and Taylor scales, 8 x 8 RASJA. . . . .	79
4.3	Kolmogorov and Taylor scales, 16 x 16 RASJA. . . . .	80
4.4	Reynolds numbers and Peclet number, 8 x 8 RASJA. . . . .	81
4.5	Reynolds numbers and Peclet number, 16 x 16 RASJA. . . . .	81
6.1	Percentiles of Reynolds stress distribution and corresponding friction velocities. $\Phi_{on} = 6.25\%$ , $T_{on} = 4$ s, 8 x 8 RASJA. . . . .	100
6.2	Lower bounds of tails of friction velocity $u_*$ (cm/s) distribution for three RASJA settings. . . . .	101
7.1	Comparison of integral length scale measurements above solid and sediment boundaries. 16 x 16 RASJA. . . . .	121

# CHAPTER 1

## INTRODUCTION

### 1.1 Motivation

Classic shear-driven turbulent boundary layers have been studied extensively, dating back to the canonical work of von Karman (1930), who presented significant contributions to boundary layer characterizations that are still used today. While such boundary layers are well-understood and are of obvious importance in environmental and industrial flows, relatively little is known about boundary layers in which turbulence is dominant and mean shear is minimal. When turbulence levels are in excess of those that are generated by wall-bounded mean shear stress, for example, in bore-advected turbulence in coastal zones (Cowen et al. 2003), the boundary layers vary greatly with respect to canonical shear-driven models.

It is vital to consider the case of stress on a boundary with active turbulence but little or no mean shear. Even in absence of mean shear, local and intermittent turbulent events can generate strong viscous shear stresses that contribute to sediment pick-up. Furthermore, pressure gradients and fluctuations associated with these flows can cause fluidization of the bed and sediment motion not expected by shear alone (Musa et al. 2014, Foster et al. 2006). As a gap remains in the literature regarding how to identify these extreme events when mean statistics of the flow are not sufficient to generate strong shear or initiate sediment transport, we choose to focus on the characterization of turbulence in the absence of mean shear to understand the unique boundary layer formed and the generation of stress in a mean shear free environment.

## 1.2 Background

### 1.2.1 Turbulence Absent Mean Shear

A variety of studies have been performed to address turbulence in the absence of mean shear via two main turbulence generation models: turbulent boxes and moving beds. Experimentally, the former primarily encompasses grid-stirred tanks (GSTs), in which interacting wakes from an oscillating grid stir ambient fluid into homogeneous isotropic turbulent flow away from the grid. In numerical models, this is typically achieved by inserting non-turbulent boundaries, solid or otherwise, into a shear-free turbulent flow. Moving-bed experiments are characterized by the advection of grid-generated turbulence over a boundary moved at the mean flow speed in order to eliminate mean boundary shear.

GSTs were initially developed to investigate mixing and entrainment rates in low mean flow environments (Rouse & Dodu 1955). Without additional flow forcing or damping mechanisms present in GSTs, it was generally assumed that mean flows were not present, and thus, the GST became popular for studying mean shear free turbulent boundary layers throughout the latter half of the 20th century.

Early studies explored the dependence of root mean square (RMS) velocities and turbulent kinetic energy upon grid characteristics and the parameters prescribing the grid's motion. The dependence was studied as a function of the mesh size of the grid, as well as the driving amplitude and frequency of the oscillations. Away from boundaries, RMS velocities were found to decay with distance from the grid throughout the tank as  $\alpha z^{-1}$  (Thompson

& Turner 1975, among others). Hopfinger & Toly (1976) found the relationship  $u_{RMS} = 0.25fS^{1.5}M^{0.5}z^{-1}$  to characterize the strength of boundary-parallel velocity fluctuations, where  $f$ ,  $S$ , and  $M$ , the frequency, stroke, and mesh spacing, are all fixed parameters of the grid. This leads to a constant decay in both boundary-normal and boundary-parallel RMS velocities with distance from the turbulence generating mechanism.

GSTs have also been used to study turbulent boundary layers absent mean shear at free surfaces by, *inter alia*, Brumley & Jirka (1987), who found the depth of the surface-influenced layer to scale with integral length scale, whereas the turbulence of the surface-influenced layer scales with depth and with dissipation. They also observed an increase in tangential RMS velocities at the free surface that is not predicted by decay relationships (Hopfinger & Toly 1976), which should not be applied near boundaries. GSTs have become popular for investigating sediment entrainment due to turbulence, as entrained sediment concentrations can be related to RMS velocities through relatively straight-forward methods (Tsai & Lick 1986, Medina et al. 2001, among others). However, GSTs have not been used to characterize turbulent boundary layers absent mean shear at a solid interface.

Despite widespread usage of GSTs and accompanying assumptions of negligible mean flow, several experimentalists questioned their reliability and have since observed significant secondary motions (Hopfinger & Toly 1976, McDougall 1979). McKenna (2000) found that the mean flow strength, or the ratio of mean velocities to RMS velocities, was commonly as high as 25%, and that the presence of mean secondary circulations is inherent to GSTs, due to the spatially symmetric forcing of the oscillating grids.

Motivated by an interest in generating highly turbulent flows absent shear, Variano et al. (2004) developed a facility with a spatio-temporally varying randomly actuated synthetic jet array (RASJA) to reduce secondary flows common to GSTs. Studies have been performed to research the effect of the spatial layout of the jets on turbulence generated away from the source, and it was shown that a random algorithm without spatially-correlated jet firing produced highly turbulent flows with negligible mean flows (Perez-Alvarado et al. 2016). Random jet arrays have been used to study mean shear free turbulence at a free surface (Variano & Cowen 2008) but not at a solid or sediment boundary. This is our method of choice for generating turbulent boundary layers and it is summarized in Chapter 2.

Moving-bed experiments were first performed by Uzkan & Reynolds (1967) and Thomas & Hancock (1977) in water and air, respectively. While the former found damping of turbulence at the wall that scaled with a viscous length scale, the latter observed an increase in turbulence at the moving wall, due to kinematic “blocking” effects that increase tangential RMS velocities (Perot & Moin 1995a). Hunt & Graham (1978) used rapid-distortion theory (RDT) to explore these particular flows. Importantly, they defined regions of the boundary layer as shown in figure 1.1, including an outer “source region,” the thickness of which scales with the integral length scale of the turbulence, and an inner “viscous region” that is dependent upon the free stream flow velocity and distance downstream, although much of the boundary layer theory developed is for the inviscid case.

Teixeira & Belcher (2000) extended Hunt & Graham (1978)’s RDT analysis to account for viscosity and to include dissipation estimates at both a solid wall

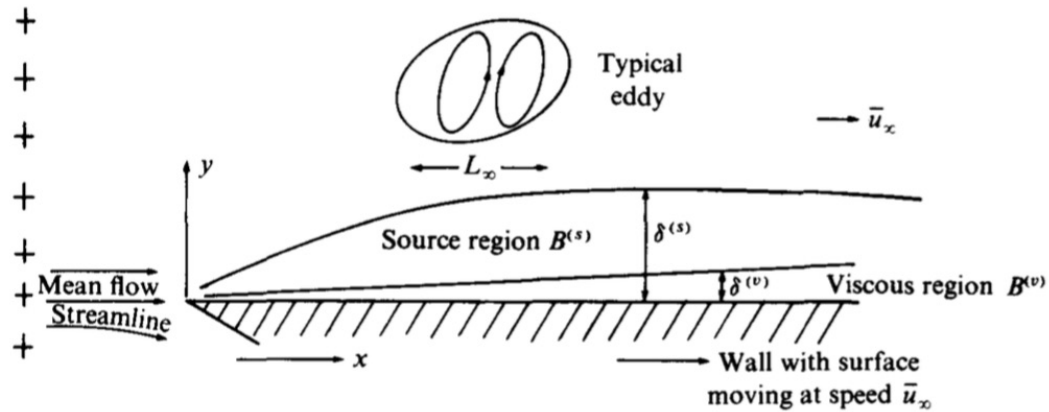


Figure 1.1: Boundary layer definitions and setup used in rapid distortion theory. Image reproduced from Hunt & Graham (1978).

and free surface by inserting a flat plate boundary into stationary turbulence. Their findings of increased tangential RMS velocities and dissipation due to the viscous no-slip condition at a solid wall agree well with the direct numerical simulations (DNS) of Perot & Moin (1995a,b) that investigated intercomponent energy transfer, Reynolds stresses, and dissipation rates at a stationary permeable wall, free surface, and solid wall. Teixeira & Belcher (2000) observed enhanced dissipation of bed-parallel RMS velocities at a solid wall, which is also shown in the RDT extension of Teixeira & da Silva (2012), who carefully examine near-bed contributions of dissipation from three-component velocity derivatives.

## 1.2.2 Sediment Suspension

In 1936, A. F. Shields examined non-cohesive sediment transport in flows dominated by mean shear. His work culminated in the famous Shields curve,

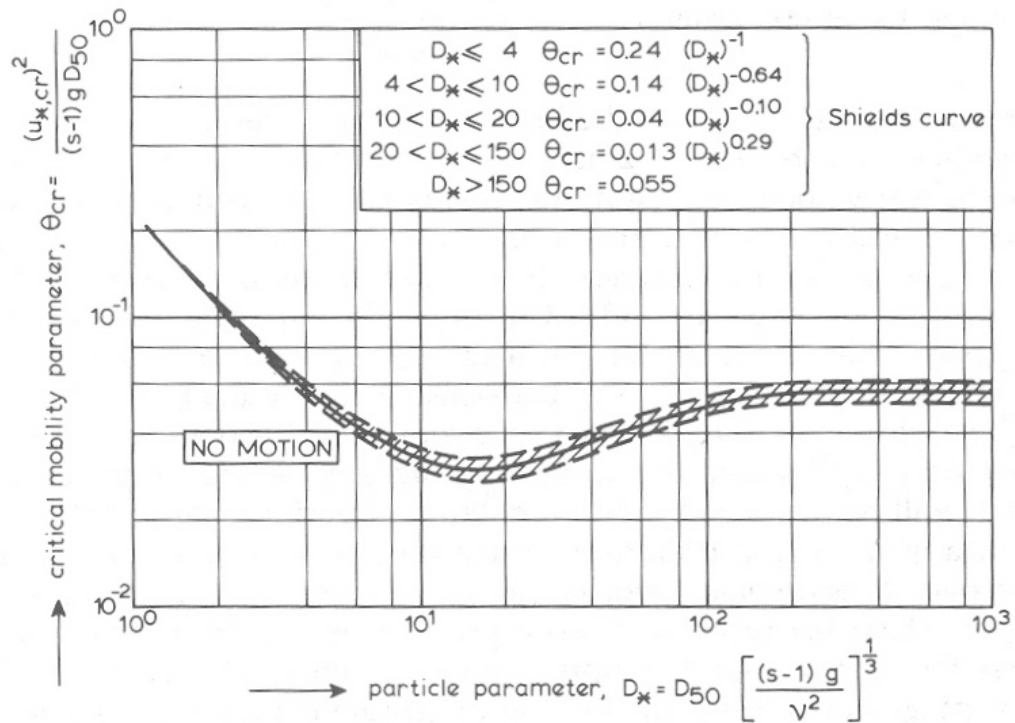


Figure 1.2: Shields curve, reproduced from van Rijn (1984).

shown in figure 1.2, which summarizes the requisite critical bed shear stress for incipient particle motion for sediments of various grain sizes and specific weights. This parameterization of critical shear stresses is used as a threshold for sediment motion in a wide variety of applications, though recent studies (Clark et al. 2015) also include parameters such as the packing structure of the bed to generate a more accurate, if complex, means for predicting sediment motion.

The work of Tsai & Lick (1986) is the first to study sediment transport in mean shear free turbulence through their experiment studies in GSTs. Sediment cores from the field were placed directly into the GSTs. Tests were run until sediment in the GST was consistently suspended and entrained into the flow, and

resulting suspended sediment concentrations were then calibrated to sediment concentrations generated in a flume where the bed shear stresses were determined by the driving parameters of the facility. Sediment concentrations were found to vary with the forced grid oscillation frequency, though flow measurements inside of the GST were not made.

Sanchez & Redondo (1998) recognized strengths of the GST to study sediment suspension, in particular, the likelihood of sediment to remain entrained in flow following resuspension from the bed. They considered suspended sediment concentrations that they calibrated to images of known sediment concentrations to determine the mass flux possible from a given turbulent root mean square velocity. The root mean square velocity was calculated from prior formulae developed by Turner (1968) based on the physical geometry of the GST and driving parameters of the oscillating grid.

Medina et al. (2001) continued the work with the GST to study initiation of sediment motion due to turbulence to determine whether the turbulent root mean square velocity compared with the critical velocities identified by the Shields curve. By placing a thin layer of uniform sand at the bed of the GST and altering the forced flow conditions until sediment was in suspension, they determined the turbulent root mean square velocity for sediment resuspension. The sediment was already in suspension when the root mean square velocity was determined, and so incipient motion was not necessarily the standard for selecting the critical GST parameters from which root mean square velocities were determined for each sediment grain size. Furthermore, velocities were not measured directly, but were instead computed from the driving frequency and geometry of the GST assuming decay of turbulence away from the grid.

In comparing these critical turbulent root mean square velocities of sediment suspension with expected critical Shields velocities for incipient sediment motion, the Shields velocities are consistently higher than GST root mean square velocities by 25-50%.

Redondo et al. (2001) developed the work further, comparing prior laboratory investigations to experiments with field sediment cores that they tested in both the GST and in a channel with turbulent shear flow. Again, turbulent root mean square velocities considered for resuspension were notably less than velocities required for incipient particle motion due to shear. The authors stated that for the GST, isotropy was an important factor in using such a facility to study this fundamental process; however, a verification of isotropy in the given GST was not presented.

### **1.3 Research Objectives**

To better understand the role of turbulence in a mean shear free environment, we have elected to perform laboratory experiments in a facility designed to generate homogeneous isotropic turbulence in absence of mean shear. We modified the facility introduced in Variano et al. (2004) by suspending the RASJA above a water tank with downward-facing jets, whose wakes merge to stir the surrounding fluid into horizontally homogeneous isotropic turbulence with negligible mean flow. We have also constructed an additional RASJA, increasing the number of jets from 64 in the original to 256 in the new array, with 4 times the density of jets. This allows more flexibility in the levels of turbulence produced and also produces a non-dimensionally deeper tank, with respect to the jet spac-

ing of each array. The algorithm that controls the individual jet activity, termed the “sunbathing” algorithm, is described in Variano & Cowen (2008) and it significantly reduces mean flows in comparison with GSTs. We explore details of this algorithm to development of turbulence in the facility, with particular focus on controlling the integral length scale with jet activity.

We perform experiments with two different bed conditions: a rigid impermeable glass plate, and a mobile sand bed. This allows exploration into the response of the flow to each imposed boundary condition. Through these experiments, we make comparisons between our facility and the aforementioned experimental and theoretical works involving grid-stirred tanks, moving beds, and temporally-evolving numerical turbulent/non-turbulent interfaces. Due to the different boundary conditions in each of these setups, we are uniquely positioned to evaluate the assumptions made in each prior facility given our experiments with a stationary bed and negligible secondary flows.

With data collected via acoustic Doppler velocimetry (ADV) and particle image velocimetry (PIV), we characterize flows in the tank, with emphasis on the region in which the flow is nearly isotropic and the near-bed region where assumptions of isotropy begin to break down. We examine mean and secondary flows, RMS velocities, turbulent kinetic energy, integral scales, and spectra, and we explore the relationship between the sunbathing algorithm and these parameters. Because higher order statistics such as dissipation can often depend on assumptions of isotropy, we explore several methods of computing dissipation, both in isotropic and anisotropic regions of the flow, in order to evaluate the implications of such assumptions. We also evaluate terms in the turbulent kinetic energy balance such as production, turbulent transport, and pressure

diffusion to understand how this unique mean shear free boundary layer compares to traditional shear driven boundaries.

As mean shear stresses are negligible in this facility, we explore alternate methods of understanding bed stress by considering Reynolds stresses computed over short time scales. In tests with a sediment boundary, we observe sediment transport in the forms of sediment suspension and ripple development. We aim to characterize the relationships between bed stresses and observed suspension. Although ripples are typically a result of mean or oscillatory flows, we observe them in absence of such driving forces and instead correlate the spacing of the ripples with the integral length scale of the turbulence.

CHAPTER 2  
EXPERIMENTAL FACILITY

## 2.1 Apparatus

Experiments are conducted in the DeFrees Hydraulics Laboratory at Cornell University in a 1.000 m tall water tank with a 0.800 m by 0.800 m horizontal cross-sectional area. Turbulence is generated by RASJAs suspended above the facility. A 1.27 cm thick glass plate is mounted into the bottom of the facility to provide a stable rigid bed. The top of the glass is located 8 cm above the base of the tank for adequate optical access. For experiments above a sediment bed, the glass is replaced with an 8 cm deep layer of Everlast commercial playsand. All of the sand was initially shaken through a #30 sieve with 600  $\mu\text{m}$  openings to eliminate stones and debris, and it is frequently washed to remove fines. The sand is narrowly graded with a mean diameter,  $D_{50}$ , of 260  $\mu\text{m}$ , according to a linear interpolation of the distribution generated a sieve analysis shown in table 2.1. It is filled to a depth of 8 cm, and so the underlying solid acrylic bottom of the tank can be neglected on account of having a solid boundary influence.

Prior to experiments, the sand bed is raked and flattened at the sediment-water interface to diminish prominent peaks, ripples, and scour holes that de-

Diameter ( $\mu\text{m}$ )	Percent passing
75	0.1
106	1.6
212	45.6
425	93.1
600	100

Table 2.1: Sand grain distribution analysis.

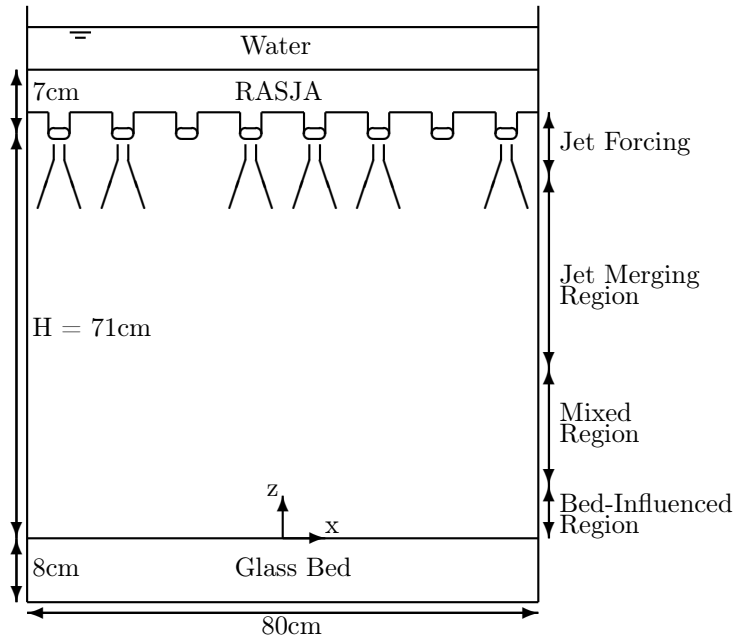


Figure 2.1: Schematic drawing of the turbulence facility with the 8 x 8 RASJA suspended above a glass bed.

velop during previous tests or experimental set-up procedures. Although the surface of the sediment is often not perfectly flat, imperfections in the initial state of less than 1 cm in height tend to disappear quickly after the jets are turned on.

The coordinate system is shown in figure 2.1, with  $z = 0$  at the top of the bed increasing upwards to  $H$ , the height of the jet orifices relative to the bed. At the lateral center of the facility,  $x = 0$  and  $y = 0$ , each orthogonal to the side walls and following the right-hand rule. Velocity components  $U$ ,  $V$ , and  $W$  follow the  $x$ -,  $y$ -, and  $z$ - directions, respectively.

### 2.1.1 8 x 8 RASJA

The original RASJA, pictured in figure 2.2, consists of 64 jets arranged on an 8 x 8 square grid with a spacing,  $J$ , of 10.0 cm from jet orifice center-to-center. A close up photo of the jet array is shown in figure 2.3. Each jet is generated by a 12 V 2.1 Amp Rule 360 g.p.h. bilge pump with a 2.19 cm diameter PVC elbow to direct the pump flow downward with an outlet velocity of 100 cm/s, as calculated by the flow rate in the specifications and jet diameter. The jet Reynolds number of each individual jet is  $Re_{jet} = 22,000$ . The jets are mounted to an acrylic support panel that has several holes for instrument access above. The water is filled a minimum of 3 cm above the panel.

All experiments with the 8 x 8 RASJA reported herein were performed with the jet orifice plane at  $H = 71.0$  cm above the bed, which is the maximum height to which the jets can be raised in this configuration. This is a sufficient height for the jet wakes to merge into homogeneous turbulence above the bed, as it was shown in Variano & Cowen (2008) and Perez-Alvarado et al. (2016) that this mixing is achieved for  $\frac{H}{J} > 6$ . As shown in figure 2.1, the fully-submerged RASJA is suspended from the top of the tank with downward-facing jets. Each jet simultaneously intakes the same volume of water that it expels; thus, the jets are termed “synthetic” in that they inject momentum, but no net mass, into the flow. The pump intake plane is 7.0 cm above the orifice plane.

The on-off states of the jets are controlled in Mathworks MATLAB via a Mea-



Figure 2.2: Photo of tank with 8 x 8 RASJA.

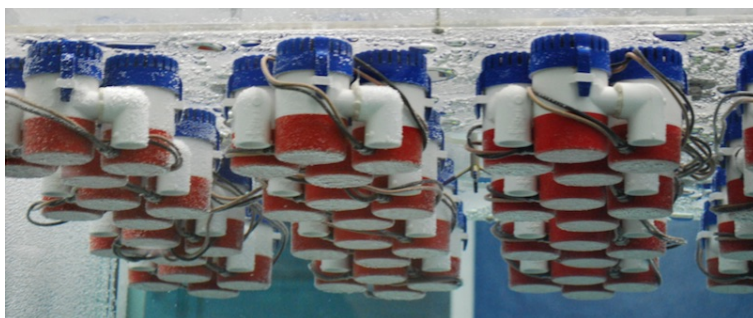


Figure 2.3: Photo of jet mountings for 8 x 8 RASJA.

surement Computing 96 channel digital output card (PCI-DIO96H) that connects to 4 custom printed control circuit boards via a series of ribbon cables. Each board controls 16 pumps, with the digital signal sent to all 16 pumps via two integrated circuits (STMicroelectronics M74HCT541B1). The signals trigger solid-state relays (CRYDOM CMX60D5) to activate the pumps. The top circuit board pictured in figure 2.7 is one of the control boards.

The sunbathing algorithm is updated at a 10 Hz output frequency. The al-

$\Phi_{on}$ (%)	$T_{on}$ (s)	$T_{off}$ (s)	$\sigma_{on}$ (s)	$\sigma_{off}$ (s)
6.25	4.0	60.0	1.3	20.0
6.25	8.0	120.0	2.7	40.0
12.5	4.0	28.0	1.3	9.3
12.5	8.0	56.0	2.7	18.7

Table 2.2: Sample RASJA control parameters.

gorithm randomly selects instantaneous on-times from Gaussian distributions given user-input operation parameters  $T_{on}$ , the mean on-time of each jet, and  $\Phi_{on}$ , the mean percentage of jet activity. Table 2.2 shows an example of how these parameters are set.  $\Phi_{on}$  is ultimately determined by the ratio of  $\frac{T_{on}}{T_{on}+T_{off}}$ , and standard deviations  $\sigma_{on}$  and  $\sigma_{off}$  are set to one-third the value of  $T_{on}$  and  $T_{off}$ , respectively, in the Gaussian distribution, with limits set to prevent negative on-times. Given the work of Variano & Cowen (2008), who found maximum turbulent kinetic energy for  $6\% < \Phi_{on} < 25\%$  (see Variano & Cowen 2008) at  $T_{on} = 3$  s, we control the turbulence levels by varying the sunbathing parameters through the ranges  $6.25\% < \Phi_{on} < 12.5\%$  and  $2 \text{ s} < T_{on} < 8 \text{ s}$ . Mean on-times longer than 8 s can cause direct impingement of the jets onto the bed in this facility with the 8 x 8 RASJA.

### 2.1.2 16 x 16 RASJA

The new facility consists of 256 jets arranged on a square 16 x 16 grid with  $J = 5.0$  cm. The jets are generated by 12 V 2.8 Amp Rule il200 submersible in-line pumps. Each pump has a specified flow rate of 168 g.p.h. through an 8.0 mm downward nozzle. This produces an outlet velocity of 350 cm/s with a jet Reynolds number  $Re_{jet}$  of 28,000. The jets are suspended at  $H = 65.0$  cm above the bed, resulting in a nondimensional jet height  $\frac{H}{J} = 13$ , nearly twice the value



Figure 2.4: Photo of inline jet array for 16 x 16 RASJA.

obtained in the 8 x 8 RASJA. There is an intake plane 12.9 cm above the jet orifice plane. There is no lid on the facility, and the water is filled approximately 8 cm above the suction plane to ensure air does not enter the pumps. With a significant increase in  $Re_{jet}$  and an increase in the number of jets by a factor of 4, we explore much lower values of  $T_{on}$  and  $\Phi_{on}$ , with a  $0.8 \text{ s} < T_{on} < 1.6 \text{ s}$  and  $\Phi_{on}$  of 3.1% .

The jets are mounted in a custom designed PVC cage-like structure that is uniform across the entire  $x - y$  plane, pictured in figure 2.4, whereas the jets in the 8 x 8 RASJA are clustered in groups of 4, as shown in figure 2.3. The RASJA is suspended above the tank from an aluminum 80/20 frame connected to the existing steel tank frame. The mounting includes a precise hand winch (Shelby Industries 5312) for easy raising and lowering of the jets by a single user. The jets are secured in place with two 80/20 linear bearings (2RCJ9) with L-brake handles (2RCP2).

The entire 16 x 16 RASJA is controlled via a single Arduino Mega 2560 mi-

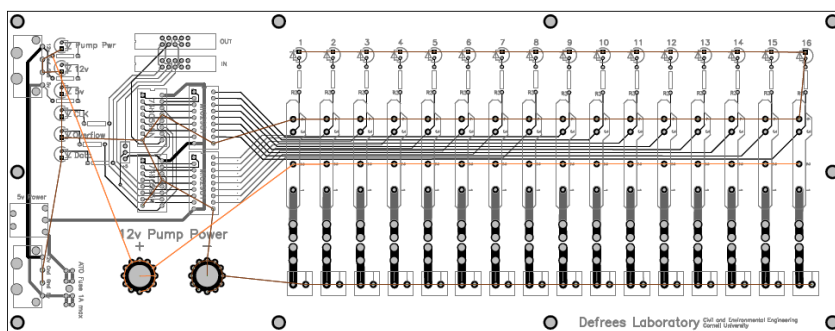


Figure 2.5: Design of pump control circuit board for 16 x 16 RASJA.

controller rather than the MATLAB digital input/output card that controlled the 8 x 8 array. Because the instantaneous on/off states are selected from Gaussian distributions, MATLAB is necessary to select the on/off states. MATLAB transmits instantaneous on/off states to the Arduino through serial communication. Timing is controlled by MATLAB, but rather than using the DIO toolbox, timing is controlled via carefully selected pauses in the scripts, as shown in Appendix A. The Arduino, which operates at 16 MHz, efficiently sends on/off signals to the 256 jets by passing 32 bytes to shift registers (Texas Instruments SN74HC595N) and integrated circuit driver arrays (MIC2981/82YN) on the new pump control boards; 1 byte contains the on/off states of 8 individual jets. Only 12 new control boards (figure 2.5) were designed; the original 4 control boards are integrated into the new system by connecting each board to the “quad board” shown in figure 2.6. The quad board uses shift registers to convert the Arduino signal into digital inputs that can be read by the 8-bit Buffer/Driver (M74HCT541B1) on the original control boards.

Because of the increased number of jets and the increase in current demand of each inline jet, the new circuit boards are designed with increased safety features to prevent overloading the individual boards or the pump power supply.

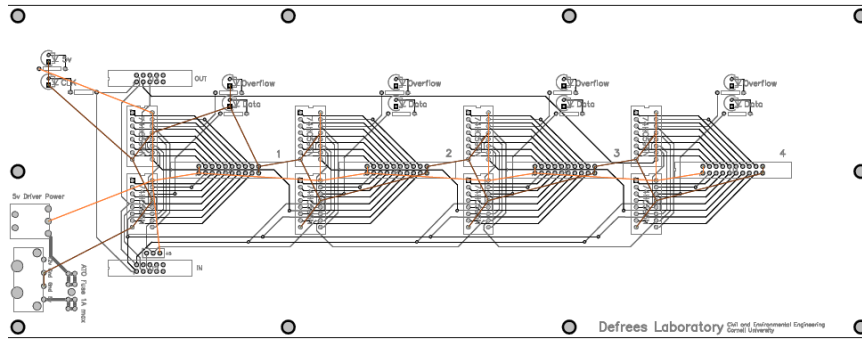


Figure 2.6: Design of circuit “quad” board to integrate Arduino controls on existing 8x8 RASJA control boards.

For example, no more than 4 jets on a single circuit board (of 16 jets) may be on simultaneously. Although the power supply operates safely up to 160 Amps, a typical current reading is lower than 100 Amps. Timing is controlled in MATLAB such that the pump states are updated on a 10 Hz output frequency; this prevents buffering errors that can occur if the timing is controlled by the Arduino.

### 2.1.3 Jet-Monitoring System

To ensure each individual jet operates at full capacity, we designed and installed a jet monitoring system to read the voltage across each pump and verify that it falls within the proper operational range. The system consists of 4 monitor circuit boards that are paired with the original 4 control circuit boards, as shown in figure 2.7. Each monitor circuit board contains an Arduino Mega 2560 microcontroller, 16 shunt resistors (Caddock MP2060), and 4 operational amplifiers (Texas Instruments OPA4241PA), as the primary components. The blueprint of the monitor circuit board is shown in figure 2.8.

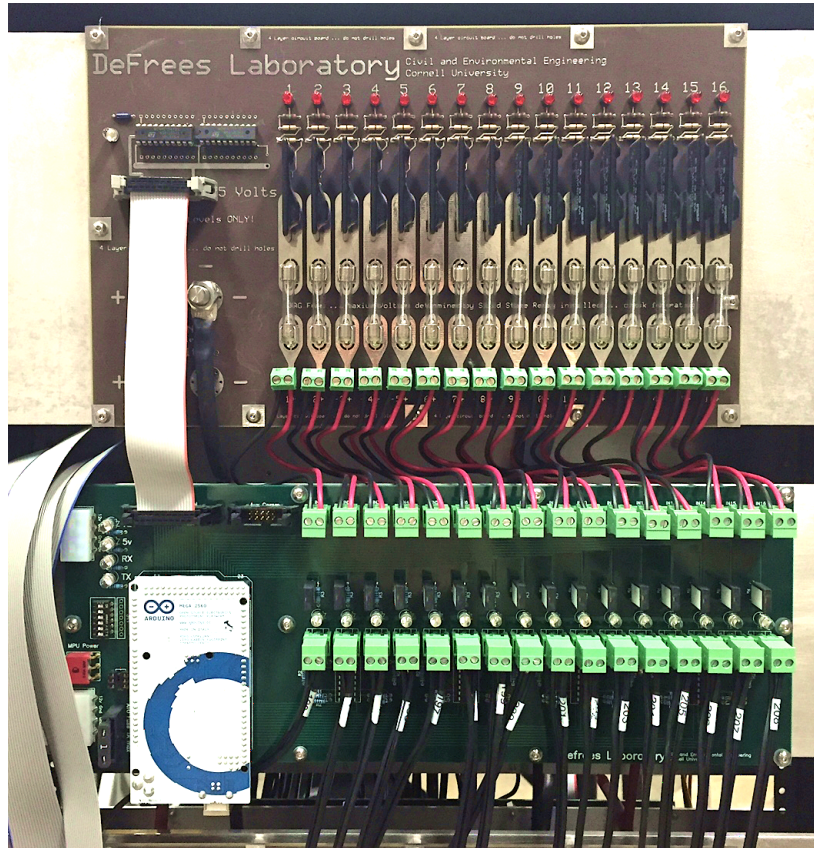


Figure 2.7: Photo of 8 x 8 RASJA monitor circuit board.

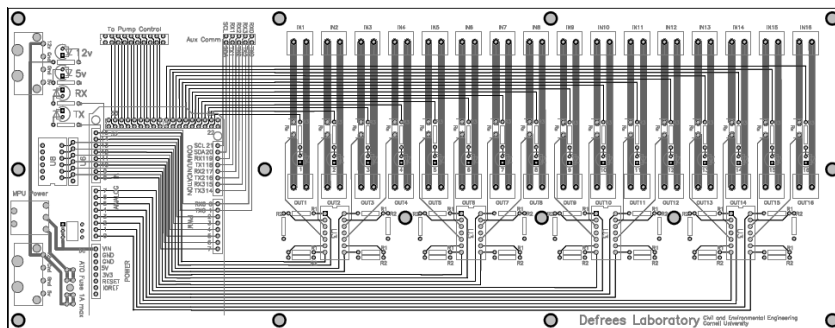


Figure 2.8: Design of monitor circuit board.

In the original design of the RASJA controls, a red LED on the control circuit board is illuminated when a pump is activated via a MATLAB digital input/output card (PCI-DIO96H). There is one red LED per pump. The light turns on after receiving a signal from MATLAB even if the pump is disconnected or does not turn on due to a blown fuse, faulty wire, dead motor, or a variety of other issues that can cause the circuit to fail. In the updated monitoring system, each of the jet control wires passes through the monitor circuit boards prior to connecting to the pump. When the pump is activated, the voltage drop in the line is measured across the shunt resistor and amplified by the operational amplifier for a more reliable voltage reading. The signal is then read by the analog input pins of the Arduino microcontroller and into MATLAB in real time via a USB 2.0 connection. If the recorded voltage drop is in the range 450-600 mV, this signifies that the current through the line is sufficient to power the pump and a green LED is illuminated.

## **2.2 Measurement Techniques**

### **2.2.1 Acoustic Doppler Velocimetry**

Acoustic Doppler velocimetry (ADV) measurements are made using a Nortek Vectrino with “plus” firmware to record three components of velocity at a single point location. All results shown herein are located 12.0 cm above the bed at the lateral center of the tank, as shown in figure 2.2. The instrument is mounted vertically, with the  $z$ -axis of the ADV aligned with the  $z$ -axis of the tank, and the instrument  $x$ - and  $y$ -axes orthogonal to the tank walls. Measurements are

recorded at a sampling frequency of 100 Hz with a sampling volume length of 7.0 mm and transmit length of 1.8 mm. To ensure convergence of turbulence statistics, data records are at least 30 minutes long. An adaptive Gaussian (AGW - now available at <https://github.com/eacowen/AGW>) filter (Cowen & Monismith 1997) is applied to data to eliminate spurious measurements due to instrument noise and/or instantaneously low seeding density. Less than 1% of the data is eliminated through this method. Filtered data points are linearly interpolated to compute frequency spectra as they require a complete temporal record.

### **Seeding Particles**

Arkema Group ORGASOL (R) 2002 ES 3 Nat 3 Polyamide 12 nylon particles are used to seed the flow for accurate ADV measurements. These particles feature an average batch diameter of 29.4  $\mu\text{m}$ , with 5% less than 20  $\mu\text{m}$  and 8% greater than 40  $\mu\text{m}$ . With a specific gravity of 1.03, they are effectively neutrally buoyant. For all flow cases considered, the Stokes number  $St = \frac{\tau_R}{\tau_\mu}$  in which  $\tau_\mu$  represents the Kolmogorov time scale (details presented in Chapter 4) and  $\tau_R = \frac{(S)D_p^2}{18\nu}$  is a relaxation time scale, we find values of  $St$  consistently less than 0.001. We assume water at 20° C to determine kinematic viscosity  $\nu$ . With  $St \ll 1$ , we conclude that the particles passively follow the flow and serve as passive tracers.

### **Preliminary Measurements**

With our ADV data, we can explore isotropy and symmetry in the facility. We compute temporal frequency spectra, an example of which is shown in figure

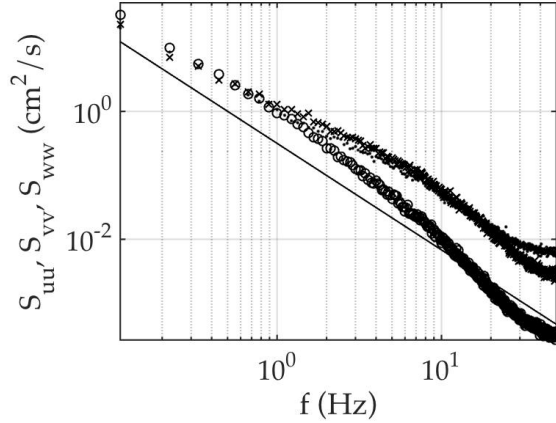


Figure 2.9: Temporal spectra from ADV measurements at  $z = 12.0$  cm above the bed.  $S_{uu}$  ( $\times$ ),  $S_{vv}$  ( $\cdot$ ),  $S_{uvw}$  ( $\circ$ ).  $T_{on} = 4$  s,  $\Phi_{on} = 6.25\%$ ,  $8 \times 8$  RASJA.

2.9, in which we see the expected  $-\frac{5}{3}$  slope in the inertial subrange. As expected with acoustic instruments in the orientation used, there is higher noise along the  $x$ - and  $y$ -axes (ADV stem-orthogonal plane) than along the  $z$ -axis (ADV stem-axis plane). This difference is likely due to geometry effects of the ADV. In the tails, the noise in  $v$  is slightly elevated above the noise in  $u$ , though otherwise the spectra are nearly identical when computed from  $u$  and  $v$ .

As the integration of the spectra give the variance of the velocity record, we also expect nearly equivalent values of bed parallel and bed normal RMS velocity  $u' = \sqrt{\overline{u'^2}}$  (and likewise for  $v'$  and  $w'$ ). Indeed, we find a ratio of  $\frac{v'}{u'}$  of 1.047 across all 30 tests, where the 5% disparity likely comes from elevated noise along the  $y$ -axis. With this, we conclude that the tank is radially symmetric, with flows along the  $y$ -axis statistically equivalent to flows along the  $x$ -axis. From the ADV, we find the ratio of  $\frac{w'}{u'} = 1.05$  and  $\frac{w'}{v'} = 1.11$ .

## 2.2.2 Particle Image Velocimetry

### Image Collection

Particle image velocimetry (PIV) is used to record spatio-temporal data in the lateral center of the tank, in the  $x - z$  plane, at the bottom boundary. Measurements are collected using an Imperx Bobcat IGV-2020 camera with 2056 by 2060 pixel resolution and either a Nikkor 50 mm lens or Nikon 60 mm lens, each with  $f/2.8$ . Illumination is provided by a Coherent Innova 90 Argon Ion laser operated at approximately 3 W power with a wavelength of 488 nm and 514.5 nm in multi-line mode. The beam, which is 1.4 mm in diameter, passes through a 2.5 mm diameter mechanical shutter (NM technologies LS200) and is scanned through the planar field of view (FOV) with a mirror (Cambridge Technologies 6M8505X-V) attached to a galvanometer (Cambridge Technologies 6860). Each scan is completed within 5 ms, and the time,  $\Delta T$ , between the scans is 8 ms. Additional details on the selection of  $\Delta T$  are included in the following sub-section.

The shutter, mirror, and camera are synchronized using a National Instruments analog output card (PCI-6711) controlled by MATLAB, as shown in figure 2.10. The Bobcat camera operates at a maximum frequency of 16 Hz, so double-exposure mode must be activated for image collection in PIV for which the time between images,  $\Delta T$ , is less than 63 ms, as is the case in our tests. In double-exposure mode, the integration time of the first image is set by the user and is triggered by MATLAB. For the first image, the camera begins to integrate 4.5 ms prior to the opening of the shutter to ensure that it is fully open and to allow some ambient light to enter the camera in order to balance the second image slightly. The camera begins to record the second image immediately after

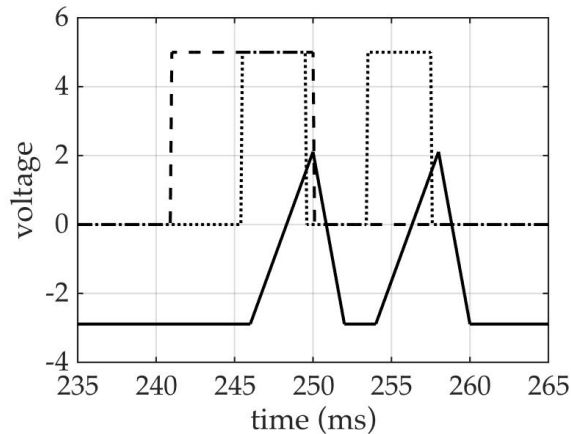


Figure 2.10: Timing code of mirror scan (solid line), shutter (dotted line), and integration time of first image collected by Bobcat camera (dashed line).

the first image finishes. The integration time of the second image is equivalent to the amount of time necessary for the camera to transfer the data from the first image, which is closer to 60 ms. Thus, it is imperative to have a dark environment so as not to contaminate the second image with ambient light. PIV data presented in this dissertation are for experiments performed at night.

Nylon ORGASOL particles are also used for PIV measurements, though PIV and ADV data are not collected simultaneously. Velocity fields are acquired at a sampling frequency  $f_s$  of 1 Hz to ensure independence of samples. Results reported herein are for tests of 30 minutes in duration, which was found to be a sufficient period of time for statistics to converge to the same levels as if tests were run over a 24 hour period (Variano & Cowen 2008).

Image analysis is performed in MATLAB using a sub-pixel cross-correlation peak locating PIV algorithm developed by Liao & Cowen (2005). This accurately determines particle displacements between image pairs separated by a time  $\Delta T$ , with a spectral continuous subwindow shifting method to improve subpixel

particle displacements. In order to reduce error caused by tracer particles that are highly sheared due to the energy of the turbulent flow, we artificially expand the illuminated tracer particles by convolving the images with a  $4 \times 4$  Gaussian kernel using MATLAB's `imfilter` function, as is described in Variano (2007).

Before analyzing the images, we perform pre-processing to remove background noise introduced by uniform ambient light and reflections off of the glass bed. We looked temporally across all pixels in the first image of every pair and computed the minimum light intensity to compile a single background image. We repeat this process to compute a background image for all of the second images. The second image in each pair tends to be brighter than the first image. These background images are subtracted from all of the raw images.

An initial interrogation is completed with  $64 \times 64$  pixel subwindows with 50% overlap in order to determine a first estimate for particle displacements across the FOV. There are 6 iterations for the algorithm to converge upon pixel displacements in each subwindow; unconverged vectors, marked as zero in the algorithm, are then replaced with a value of NaN. The resulting converged vectors from the initial pass are smoothed using a function `mediannan` (see Appendix B), which is similar to MATLAB's `medfilt2` function, in which vectors are smoothed according to the median of valid vectors with a  $3 \times 3$  array of neighboring subwindows. Unconverged vectors are not smoothed and are replaced with zero following the smoothing. The results of the median filter smoothing of valid particle displacements are then used to guide a more refined grid with  $32 \times 32$  pixel subwindow interrogation of the images, again with 50% overlap, to obtain the final particle displacements.

## Spatial Calibration of Images

To convert pixel displacements computed in the PIV analysis routine to physical space, we collect a series of images of a ruler. We place a metal ruler through a hole in the center of the RASJA and place it into the FOV. Because there is limited physical access to the interior of the tank through the RASJA and the ruler can pass in and out of the plane of the FOV, we illuminate the ruler in the same way that we illuminated the flow during data collection, synchronizing the mirror scan of the laser beam with image collection of the ruler. This way, we can ensure that the ruler is in the FOV when it is brightly illuminated by the laser.

We select 5 to 10 images of the ruler to perform spatial calibration, choosing images that show the ruler brightly illuminated and vertically oriented. By zooming in on the ruler, we can identify which pixel corresponds to measurement locations along the ruler. For example, in figure 2.11, the tick mark at 20 cm corresponds to pixel 211 on the vertical axis, while the 5 cm tick mark corresponds to pixel 1531. We then compute a calibration coefficient to relate pixels to distance; in this example, the resulting resolution is 0.011 cm/pixel.

Given the resulting PIV analysis grid generated by 32 x 32 pixel subwindows at 50% overlap, the resulting spatial resolutions for the various tests range from 1.58 mm to 1.76 mm from subwindow center-to-center, depending on the particular experiment and location of the camera. The tests all have a FOV of approximately 20 cm x 20 cm.

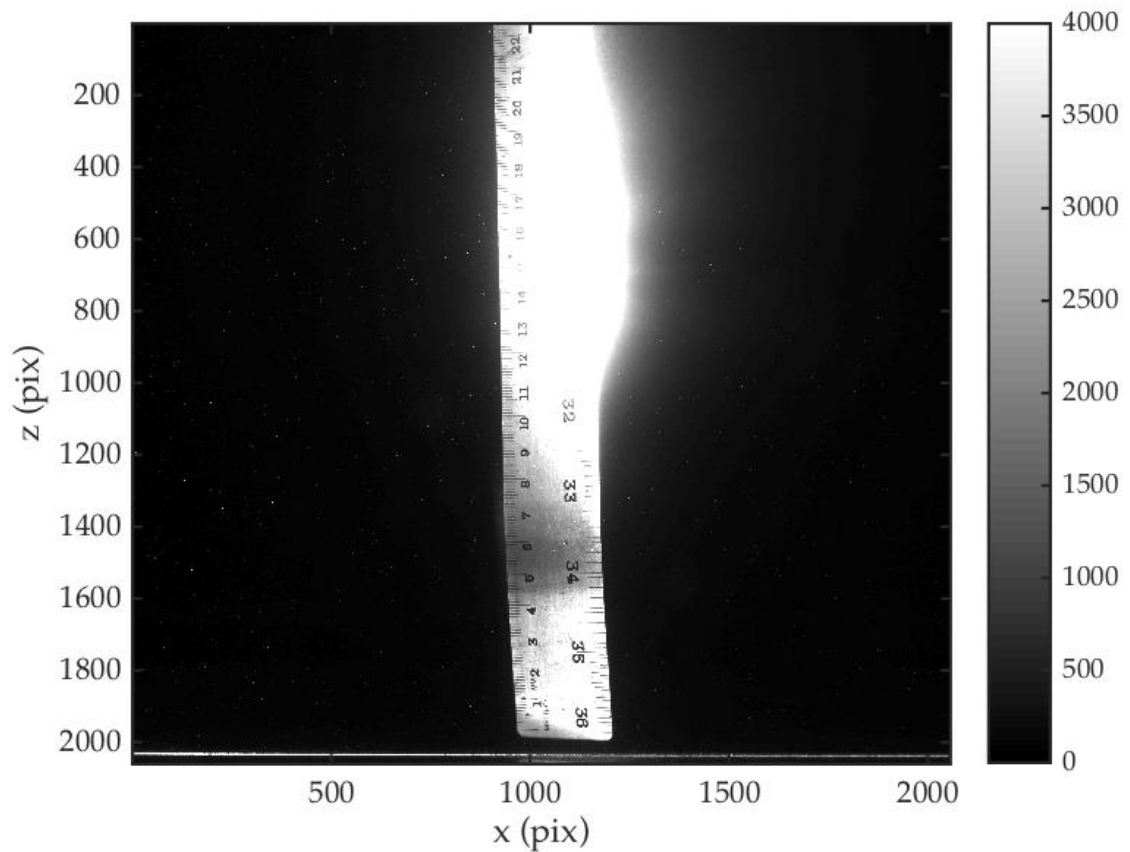


Figure 2.11: Image of ruler for spatial calibration of PIV images. Colorbar represents image intensity, out of a maximum of 4095.

### Selection of $\Delta T$

In flows with a uniform mean velocity, it is relatively straightforward to select  $\Delta T$  for reliable velocity measurements. However, as the turbulent flow generated in these experiments is highly sheared in different directions, it is challenging to determine the optimal  $\Delta T$ . With too short a  $\Delta T$ , we find we may not be able to capture the full energy of this flow via particle displacements and accuracy is sacrificed. However, too long of a  $\Delta T$  allows particles to travel out of the plane of the FOV, resulting in unmatched particles. Furthermore, as  $\Delta T$

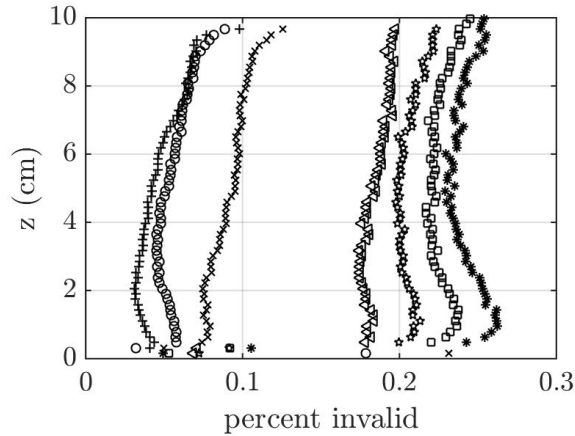


Figure 2.12: Profiles of invalid vector counts as a function of  $\Delta T$ . 4 ms (+), 5 ms (o); 6 ms (x); 7 ms ( $\triangleleft$ ); 8 ms ( $\star$ ); 9 ms ( $\square$ ); 10 ms (\*).

increases, we see lower valid vector counts due to strong shear.

To determine the optimal  $\Delta T$  for these experiments, we run trials varying  $\Delta T$  from 4 ms to 10 ms. We note that these are only 10 minute experiments, so the statistics are not fully converged, but are sufficient to show trends. As is expected, our valid vector counts drop with increasing  $\Delta T$ , as is shown in figure 2.12. Note that the maximum  $z$  is limited to 10 cm due to the limited range of motion of the galvanometer for a  $\Delta T$  of 4 ms, whereas a  $\Delta T$  of 7 ms is a long enough period of time to scan the full 20 cm FOV at the maximum scan speed of the device. Considering profiles of turbulent kinetic energy,  $k$ , (to be defined and discussed in the following chapter) shown in figure 2.13, we observe increasing values of turbulent kinetic energy with  $\Delta T$  for  $\Delta T < 8$  ms. For  $\Delta T > 8$  ms,  $k$  remains constant. Thus, we selected  $\Delta T$  of 8 ms to preserve optimal particle correlations with  $k$  independent of  $\Delta T$ . The results obtained with PIV for  $\Delta T = 8$  ms are consistent with ADV measurements as well.

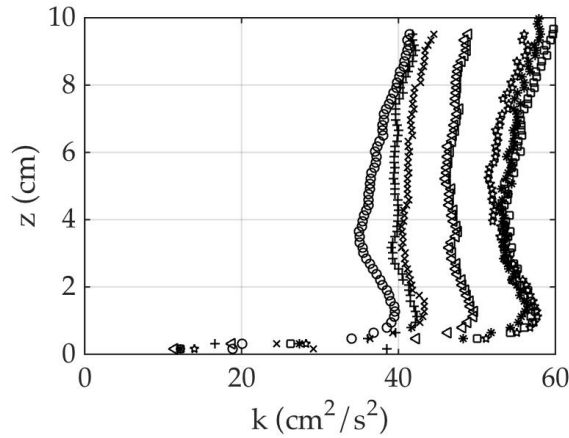


Figure 2.13: Turbulent kinetic energy profiles as a function of  $\Delta T$ . See previous figure for legend.

### Identifying the Location of the Bed

Before images can be interrogated to identify particle displacements, the location of the bed must be properly identified. Above a flat plate, this is very simple, as the bed is uniformly illuminated across the width of the FOV. By computing a profile of average intensity, we look for the start of the peak intensity and mark the bed as one pixel location higher than that. For example, if illumination peaks at pixel 2001, images are interrogated up to the 2000th pixel, with pixel 1 at the top of the image and pixel index increasing downward. The bottom of the lowest subwindow is located at that pixel.

At a sand bed, this procedure is more complicated. Because the bed is not uniform in  $x$ , we create a mask, which is a spatial array of zeros and ones, to apply to each image. At pixel locations at and below the surface of the bed, the mask contains zeros, while pixels located above the bed are denoted by ones in the mask matrix. Once the mask is generated, it is simply multiplied by the original image so that only particles above the bed are kept for image interro-

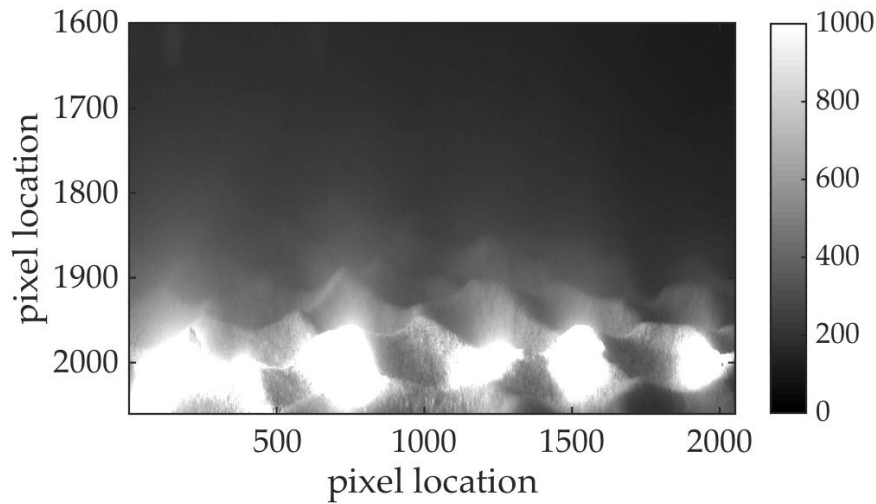


Figure 2.14: Sample background image computed for 1 minute of data,  $\Phi_{on} = 6.25\%$ ,  $T_{on} = 3$  s, zoomed to bottom 25% of image. Intensities up to 1000 are shown, out of possible maximum saturation illumination of 4095.

gation. Beneath the bed, low magnitude random noise is added to the image because a correlation of zero with zero causes our analysis routine to fail.

To identify the location of the bed and create the mask, the data is first divided into 30 one-minute increments. The bed does not move appreciably during one minute, so one mask can be created for each minute of data. Computing masks instantaneously is troublesome as the masks are easily contaminated by noise such as bright particles. A background image is computed for each minute of data by finding the minimum value at each pixel. This effectively removes brightly illuminated particles, so that the remaining bright regions are only found at the bed.

Although out-of-plane ripples are also partially illuminated and remain visible after the background is computed, as shown in figure 2.14, they are not as bright as the laser reflections off of the sand particles at the bed in the FOV,

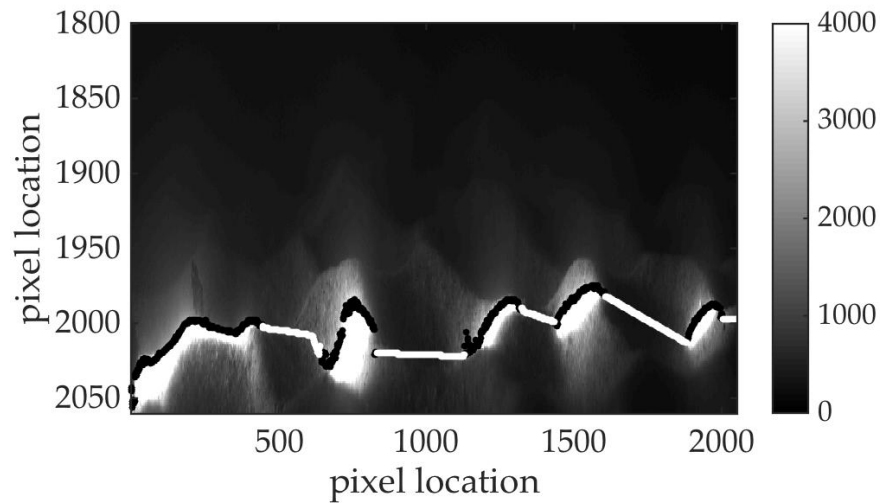


Figure 2.15: Superposition of mask onto sample background image (same as in previous figure). Black points denote bed location at illuminated ripple crests; white points denote interpolated bed location in shadowed regions.

which are typically fully saturated with light intensities of 4095 in 12-bit images. The images are scanned for the uppermost pixel with an intensity of 4095. The bed is located at this surface. Because shadows cast by the ripples prevent the entire bed from being illuminated, gaps are filled in via linear interpolation. Figure 2.15 shows the surface of the mask superimposed on the image, highlighting the resulting bed in the FOV.

Following PIV analysis above a sediment bed, a coarse mask is again applied to the resultant velocity fields to remove vectors that resulted from erroneous correlations due to the random noise applied beneath the bed. The original 2056 x 2060 pixel image is cropped slightly and translated onto an equivalent grid of subwindows (for example, a 125 x 129 grid of 32 x 32 pixel subwindows with 50% overlap). There are subwindows along the bed for which only part of the image was kept (*i.e.* consisted of ones in the original mask) and the remaining portion fell beneath the bed. If more than 2/3 of the pixels in a given subwin-

dow were originally ones in the mask, then the subwindow is sufficiently above the bed and the velocity vector for that subwindow remains valid. If fewer than the set threshold were originally ones, then the vector is replaced with a zero to signify that it is beneath the bed and is not a reliable data point.

### **Filtering & Interpolation**

Several post-processing filters are applied to reduce spurious velocity vectors from the measurements. The first filter removes unconverged vectors, which result when the PIV algorithm does not converge on a solution within 6 iterations on the refined grid, shown as a zero displacement. An AGW filter is then applied to remove the uniformly distributed spurious vectors that lie outside the statistical bounds of the assumed Gaussian distributed turbulence measurements. This is performed across all time at given subwindow heights above the bed. Finally, a 5 by 5 local median filter, with a threshold determined by the user (Westerweel 1994, Cowen & Monismith 1997) is applied to remove spurious data within an instantaneous image that lies within the statistical bounds of the assumed Gaussian distributed turbulence measurements. Between 80% and 97% of data is declared valid, with regions of high shear contributing to fewer valid vectors. Figure 2.16 shows an example of the cumulative results of each of these filters.

For computations that require full spatio-temporal data, such as spectra, Delaunay triangulation is used with linear interpolation to replace filtered data. Implications of interpolation are discussed in Section 4.1.

Velocity data is decomposed such that  $U(x, y, z, t) = \langle U(x, y, z) \rangle + u(x, y, z, t)$

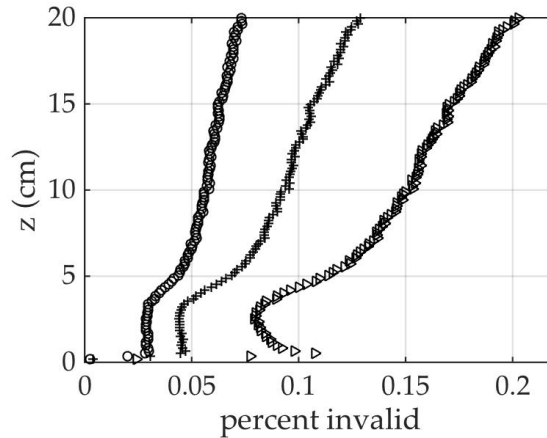


Figure 2.16: Sample profiles of cumulative filtering methods: unconverged vector removal ( $\circ$ ), AGW filter ( $+$ ), local median filter ( $\triangle$ ).  $16 \times 16$  RASJA,  $\Phi_{on} = 3.1\%$ ,  $T_{on} = 0.8\text{s}$ .

and likewise for  $V$  and  $W$ . The angle brackets denote a temporal average and lower case letters represent fluctuations. The flow is radially symmetric about the  $z$ -axis (see section 3.1 for details), thus we only measure and report PIV statistics along the  $x-z$  plane. Lateral variations across the 20 cm FOV are sufficiently small to allow us to invoke horizontal homogeneity. We use an overbar to indicate averages that include time and space (*i.e.*, the horizontal average of  $\langle U \rangle$  is  $\overline{U}$ ).

We use the bootstrap method (Efron & Tibshirani 1993) to construct 95% confidence intervals of the turbulence statistics to compute our error bounds. With our assumptions of convergence and horizontal homogeneity, the bootstrap analyses presented typically utilize between 1,800 and 225,000 data points, resampled 1,000 times, with replacement, to generate ordered random samples. The 95% confidence interval is determined by the 97.5 percentile and 2.5 percentile statistic. We make note when significantly fewer points are available for particular confidence intervals.

### 2.2.3 Time-Lapsed Photography

In order to monitor the evolution of large bedforms (*i.e.* ripples spanning 2-6 cm from crest to crest), we used time-lapsed photography. A single Nikon D40 camera was mounted beside the tank to capture still photos of the bed. The camera was controlled using the application Sofortbild. Images were captured in set time increments over periods up to 24 hours. A selection of these images is shown in figure 2.17.

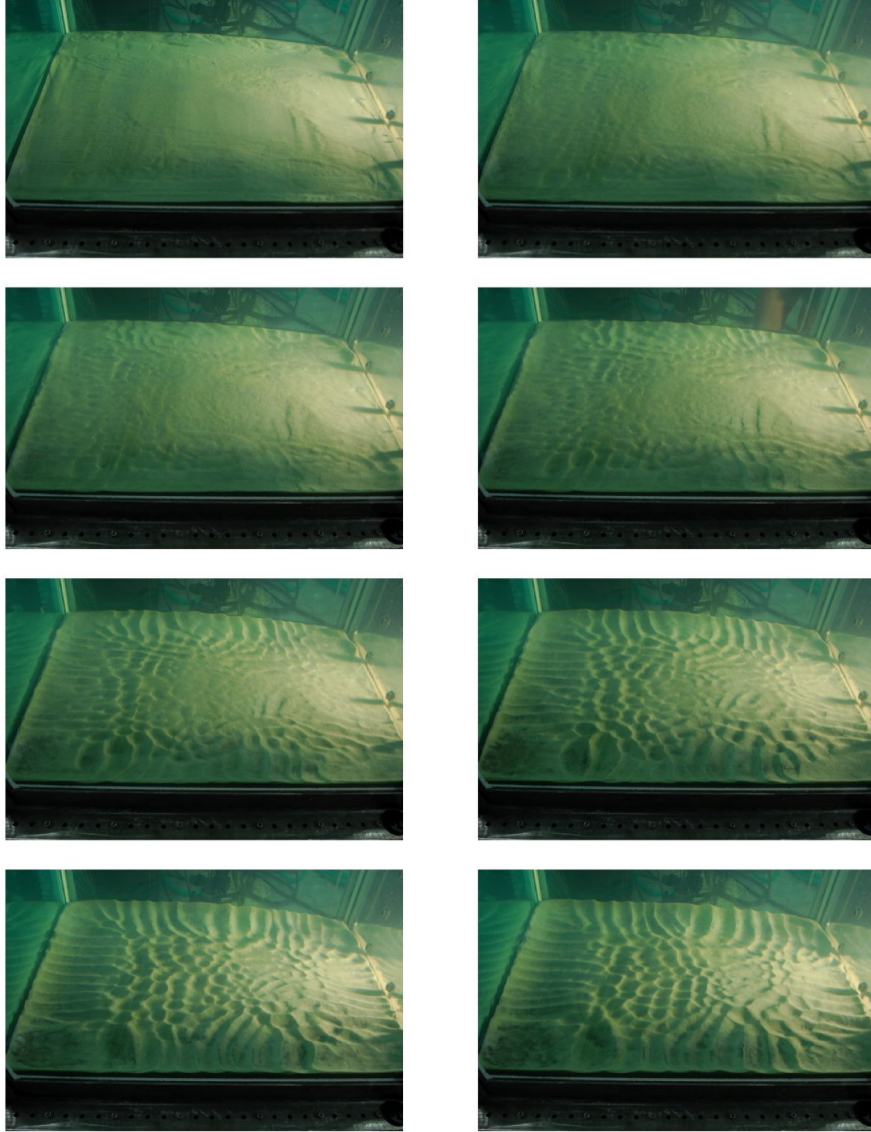


Figure 2.17: Ripple evolution observed at initial state, then 15 minutes, 30 minutes, 1 hour, 2 hours, 4 hours, 8 hours, and 12 hours into turbulence generation above an initially flat bed.  $T_{on} = 3$  s,  $\Phi_{on} = 12.5\%$ , 8 x 8 RASJA.

### CHAPTER 3

## EXPLORATION OF THE RASJA ALGORITHM TO CONTROL TURBULENCE

We first aim to characterize flows in this unique facility by exploring simple metrics such as mean velocities, turbulent velocity fluctuations, and secondary flows. This allows us to see how the flow varies with distance from the jets and proximity to the bed. It also provides a first-order understanding of the energetics of the turbulence and the relative strength of mean flows to turbulent fluctuations.

Based on the cartoon in figure 2.1, we will use this analysis to identify the region of the tank in which the wakes from jet activity are fully stirred, our “mixed region.” In our facility, the bed-influenced region, consists of both a “source region,” similar to that observed in Hunt & Graham (1978), figure 1.1, and a kinematic boundary region, which sees turbulence levels viscously decay at the bed from their peak energy levels.

Furthermore, we explore the effect of altering the sunbathing parameters  $T_{on}$  and  $\Phi_{on}$  for the turbulence generated, characterized by the aforementioned statistics. Because the integral length scale of turbulence is typically thought to depend on the geometry of the tank, we also consider whether we can control the integral length scale of the turbulence by varying  $T_{on}$  within each facility and  $J$  between facilities. All analysis in this chapter is for turbulence above a solid boundary.

## 3.1 Mean and Fluctuating Velocities

### 3.1.1 8 x 8 RASJA

As expected, temporally-averaged flow fields show near-zero mean velocity profiles. The vertical forcing of the jets induces a weak mean decaying downward flow in the center of the tank, with return flows at the walls. In the tests considered in the 8 x 8 RASJA, we find the strongest downward velocities in the upper half of the FOV, for  $z > 10$  cm, with a mean magnitude of  $\bar{W}$  is 0.80 cm/s across all cases of  $T_{on}$  and  $\Phi_{on}$ . Magnitudes of  $\bar{U}$  of approximately 0.13 cm/s, which are low relative to the turbulent velocity fluctuations we will examine in the following paragraph, are observed in this region, for all  $T_{on}$  and  $\Phi_{on}$ , as summarized in table 3.1. Figure 3.1 shows example time-averaged velocity fields across the entire FOV.

We define the RMS velocities as measures of the turbulence intensity, not to be confused with the traditional non-dimensional definition of turbulence intensity in which RMS velocities are normalized by mean velocities, as this metric would not be meaningful in our facility given the low mean flows. Figure 3.2 explores the influence of  $T_{on}$  (left) and  $\Phi_{on}$  (right) on RMS velocities  $u'$  and  $w'$ . Whereas  $\Phi_{on}$  has a relatively negligible impact on  $u'$  and  $w'$ , we observe a strong dependence upon  $T_{on}$ . As subsequent statistical analyses also show a greater dependence upon  $T_{on}$  rather than  $\Phi_{on}$ , we present the remaining statistical analyses controlled only by varying  $T_{on}$  for a selected  $\Phi_{on}$  of 6.25%.

As in the literature review of Variano et al. (2004), we consider  $M_1$  and  $M_3$ , the ratios of mean velocity to RMS velocity in the bed-parallel and bed-normal

$\Phi_{on}$ (%)	$T_{on}$ (s)	$\bar{U}$ ( $\frac{cm}{s}$ )	95% CI	$\bar{W}$ ( $\frac{cm}{s}$ )	95% CI
6.25	2	-0.13	[-0.14, -0.11]	0.97	[0.96, 0.99]
6.25	3	-0.08	[-0.09, -0.06]	0.76	[0.74, 0.78]
6.25	4	-0.17	[-0.18, -0.15]	0.32	[0.29, 0.34]
6.25	5	-0.10	[-0.12, -0.08]	0.88	[0.85, 0.90]
6.25	6	-0.14	[-0.16, -0.12]	-0.06	[-0.09, -0.04]
6.25	8	0.29	[0.27, 0.32]	0.38	[0.35, 0.38]
7.7	2	0.03	[0.02, 0.04]	1.27	[1.25, 1.29]
7.7	3	-0.17	[-0.19, -0.15]	0.78	[0.76, 0.80]
7.7	4	-0.19	[-0.21, -0.17]	0.92	[0.90, 0.94]
7.7	5	0.01	[0.00, 0.03]	1.00	[0.98, 1.03]
7.7	6	-0.19	[-0.21, -0.17]	0.35	[0.32, 0.38]
7.7	8	0.49	[0.47, 0.51]	0.36	[0.33, 0.40]
9.1	2	-0.09	[-0.11, -0.08]	1.07	[1.06, 1.09]
9.1	3	-0.08	[-0.10, -0.06]	1.47	[1.44, 1.49]
9.1	4	-0.17	[-0.19, -0.15]	0.58	[0.55, 0.60]
9.1	5	-0.09	[-0.11, -0.07]	0.81	[0.79, 0.84]
9.1	6	-0.06	[-0.08, -0.04]	0.53	[0.50, 0.56]
9.1	8	-0.21	[-0.24, -0.19]	0.40	[0.37, 0.43]
10.5	2	0.06	[0.05, 0.07]	1.57	[1.55, 1.58]
10.5	3	-0.17	[-0.19, -0.15]	1.27	[1.25, 1.29]
10.5	4	0.00	[-0.02, 0.02]	0.60	[0.57, 0.63]
10.5	5	-0.18	[-0.20, -0.15]	1.23	[1.20, 1.26]
10.5	6	0.01	[-0.01, 0.03]	0.42	[0.39, 0.45]
10.5	8	-0.05	[-0.08, -0.03]	0.51	[0.48, 0.54]
12.5	2	-0.10	[-0.12, -0.09]	1.49	[1.47, 1.50]
12.5	3	-0.20	[-0.21, -0.18]	1.73	[1.71, 1.75]
12.5	4	0.08	[0.06, 0.10]	0.72	[0.69, 0.73]
12.5	5	-0.15	[-0.17, -0.13]	0.68	[0.65, 0.70]
12.5	6	-0.09	[-0.12, -0.07]	0.28	[0.25, 0.31]
12.5	8	0.12	[0.10, 0.15]	0.63	[0.60, 0.66]

Table 3.1: Mean flows in the 8 x 8 RASJA. All values shown are the mean value of the statistic in the mixed region from PIV data.

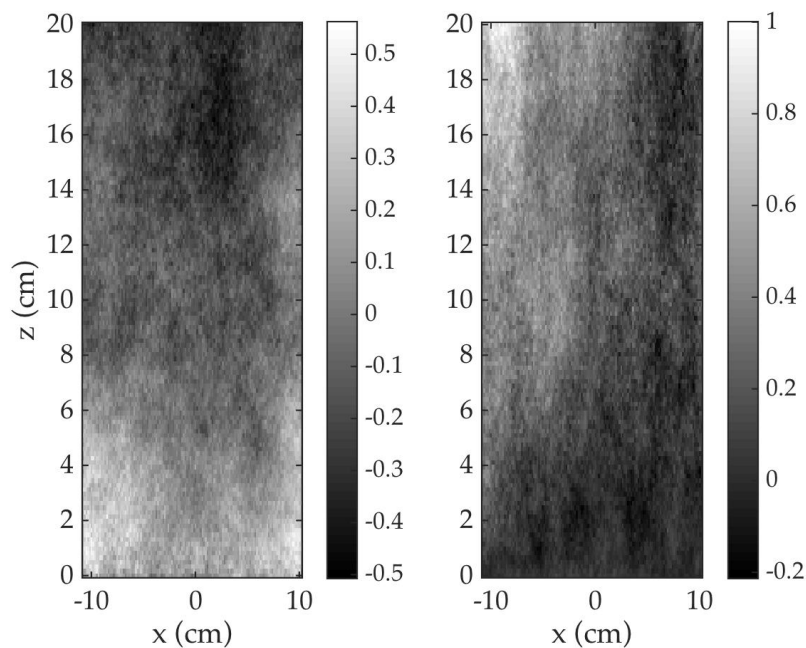


Figure 3.1: Temporally averaged flows  $\langle U \rangle$  (left) and  $\langle W \rangle$  (right). Colorbar denotes velocity in cm/s.  $T_{on} = 4$  s,  $\Phi_{on} = 6.25\%$ ,  $8 \times 8$  RASJA.

directions, respectively, to evaluate the strength of secondary flows. Clearly, if averaged over the entire facility, both  $M_1$  and  $M_3$  tend to zero, as any flow must be balanced by a return flow in another location. Because of this, we consider temporally averaged values of  $M_1$  and  $M_3$  across the entire FOV before computing  $M_1 = \frac{\langle U \rangle}{\langle u' \rangle}$  and  $M_3 = \frac{\langle W \rangle}{\langle w' \rangle}$  to ensure that averaging along the  $x$ -axis accurately represents typical values across the entire FOV. Additionally, we consider a relative mean flow strength  $M^*$ , defined as the ratio of the mean kinetic energy ( $\langle U \rangle^2 + \frac{1}{2} \langle W \rangle^2$ ) to the turbulent kinetic energy,  $k = (u'^2 + \frac{1}{2} w'^2)$ . Secondary flows were found to be negligible for flows in which  $M_1$  and  $M^*$  do not exceed 5% in Variano & Cowen (2008).

Results from PIV data for the 30 cases of varying  $\Phi_{on}$  and  $T_{on}$  in the  $8 \times 8$  RASJA are shown in table 3.2. Note that only the magnitudes of mean velocities

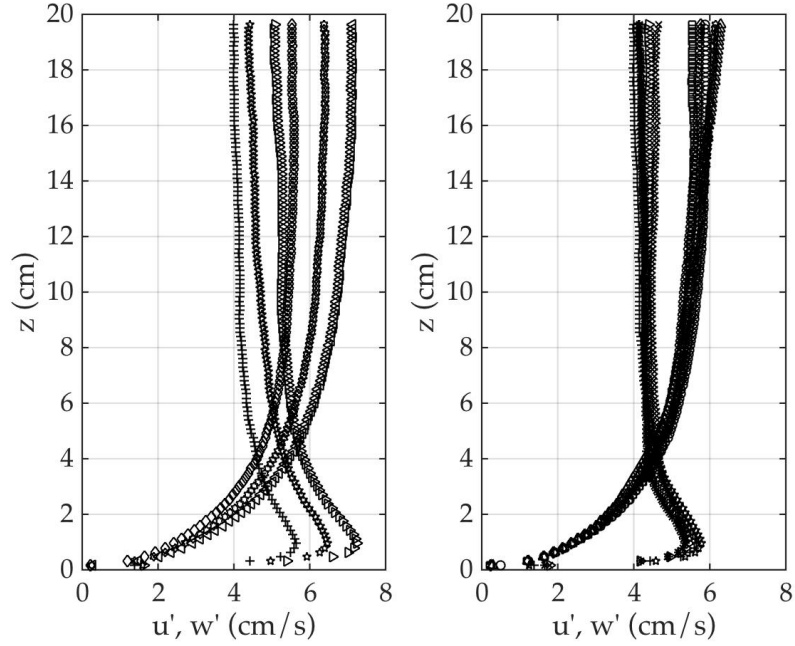


Figure 3.2: Dependence of  $u'$  and  $w'$  on  $T_{on} = 4$  s ( $u' = +$ ,  $w' = \diamond$ ), 6 s ( $u' = \star$ ,  $w' = \blackstar$ ), 8 s ( $u' = \triangleright$ ,  $w' = \triangleleft$ ) for  $\Phi_{on} = 6.25\%$  (left) and  $\Phi_{on} = 6.25\%$  ( $u' = +$ ,  $w' = \square$ ), 7.7% ( $u' = \star$ ,  $w' = \circ$ ), 9.1% ( $u' = *$ ,  $w' = \diamond$ ), 10.5% ( $u' = \triangleright$ ,  $w' = \blackstar$ ), 12.5% ( $u' = \times$ ,  $w' = \triangle$ ) for  $T_{on} = 4$  s (right); 8 x 8 RASJA.

and secondary flows are shown, though there is a net downward flow in the center of the tank. Because the 15 trials for which  $T_{on} = 4$  s, 6 s, or 8 s show considerably lower values of  $M_1$ ,  $M_3$ , and  $M^*$  than the cases for which  $T_{on} = 2$  s, 3 s, or 5 s, we are only continuing analysis for the former trials. The latter were performed on an alternate date and it was realized later that the RASJA was slightly tilted in the facility, which may account for the presence of secondary flows. For the 15 cases we are keeping, we find  $M^*$  consistently less than 3% throughout the 20 cm FOV for the cases considered. We find typical values of  $M_1$  around 4%, and typical values of  $M_3$  around 7%.

$\Phi_{on}$ (%)	$T_{on}$ (s)	$\overline{M}_1$ (%)	$\overline{M}_3$ (%)	$\overline{M}^*$ (%)
6.25	2	2.54	22.74	4.50
6.25	3	1.81	15.00	1.95
6.25	4	2.83	5.39	0.38
6.25	5	2.00	16.11	2.72
6.25	6	1.39	0.62	0.18
6.25	8	6.38	4.76	0.76
7.7	2	3.16	30.40	7.69
7.7	3	4.20	14.90	2.25
7.7	4	2.61	14.35	2.08
7.7	5	0.95	17.33	2.77
7.7	6	4.33	4.68	0.39
7.7	8	12.69	4.82	0.99
9.1	2	0.18	24.76	5.18
9.1	3	2.54	30.55	7.80
9.1	4	1.68	9.45	0.97
9.1	5	1.25	12.27	1.49
9.1	6	1.07	8.26	0.91
9.1	8	2.72	6.23	0.46
10.5	2	3.42	41.58	13.75
10.5	3	4.61	26.36	5.94
10.5	4	2.24	9.26	0.89
10.5	5	4.19	18.38	3.44
10.5	6	3.32	6.44	0.70
10.5	8	4.60	7.27	0.76
12.5	2	0.26	40.28	12.18
12.5	3	4.34	35.66	10.31
12.5	4	3.35	11.78	1.38
12.5	5	1.33	12.67	1.52
12.5	6	0.12	4.25	0.33
12.5	8	4.88	8.83	0.89

Table 3.2: Secondary flows in the 8 x 8 RASJA. All values shown are the mean value of the statistic in the mixed region from PIV data.

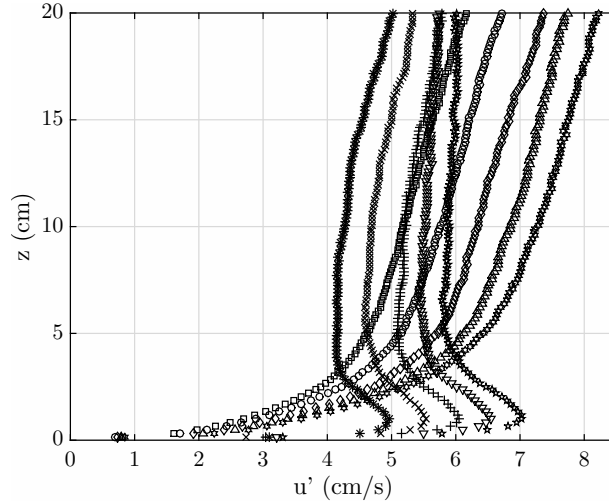


Figure 3.3: Dependence of  $u'$  and  $w'$  on  $T_{on} = 0.8$  s ( $u' = *$ ,  $w' = \square$ ),  $T_{on} = 1.0$  s ( $u' = \times$ ,  $w' = \circ$ ),  $T_{on} = 1.2$  s ( $u' = +$ ,  $w' = \diamond$ ),  $T_{on} = 1.4$  s ( $u' = \nabla$ ,  $w' = \triangle$ ),  $T_{on} = 1.6$  s ( $u' = \star$ ,  $w' = \star$ ).  $\Phi_{on} = 3.1\%$ ,  $16 \times 16$  RASJA.

### 3.1.2 16 x 16 RASJA

Given the relative independence of the turbulent velocity fluctuations on  $\Phi_{on}$  observed with the  $8 \times 8$  RASJA, we select a single  $\Phi_{on}$  of 3.1% with which to perform tests on the  $16 \times 16$  RASJA. Results from varying  $T_{on}$  are summarized in figure 3.3 and tables 3.3 and 3.4. Similar trends are observed between the  $8 \times 8$  and  $16 \times 16$  RASJAs, with a clear relationship between the RMS velocities and  $T_{on}$ . Because the RMS velocities are similar for the  $8 \times 8$  RASJA trial for  $\Phi_{on} = 6.25\%$ ,  $T_{on} = 4$  s and the  $16 \times 16$  RASJA trial for  $\Phi_{on} = 3.1\%$ ,  $T_{on} = 0.8$  s, we use these two cases for many sample plots in the remainder of this dissertation to draw comparisons.

$\Phi_{on}$ (%)	$T_{on}$ (s)	$\overline{U}$ ( $\frac{cm}{s}$ )	95% CI	$\overline{W}$ ( $\frac{cm}{s}$ )	95% CI
3.1	0.8	0.11	[0.09, 0.13]	-0.69	[-0.72, -0.67]
3.1	1.0	0.10	[0.07, 0.12]	-0.26	[-0.29, -0.23]
3.1	1.2	-0.13	[-0.16, -0.11]	-0.51	[-0.54, -0.48]
3.1	1.4	-0.19	[-0.22, -0.17]	0.29	[0.25, 0.32]
3.1	1.6	-0.03	[-0.06, 0.00]	0.11	[0.08, 0.15]

Table 3.3: Mean flows in the 16 x 16 RASJA. All values shown are the mean value of the statistic in the mixed region from PIV data.

$\Phi_{on}$ (%)	$T_{on}$ (s)	$\overline{M}_1$ (%)	$\overline{M}_3$ (%)	$\overline{M}^*$ (%)
3.1	0.8	7.33	15.59	2.41
3.1	1.0	4.72	7.76	0.88
3.1	1.2	2.34	10.75	1.17
3.1	1.4	0.38	0.42	0.12
3.1	1.6	3.33	2.71	0.18

Table 3.4: Secondary flows in the 8 x 8 RASJA. All values shown are the mean value of the statistic in the mixed region from PIV data.

### 3.2 Turbulent Kinetic Energy

By computing  $k$ , we can understand the total strength of turbulent velocity fluctuations. Recall that we invoke radial symmetry to compute  $k$  from PIV data as  $k = \frac{1}{2}(2u'^2 + w'^2)$ . This allows us to analyze how the energy described by the RMS velocities along individual coordinate directions interacts in the mixed turbulent flow and in the boundary layer. As expected from the RMS velocity results,  $k$  increases with  $T_{on}$  in the turbulence facility using either the 8 x 8 RASJA or the 16 x 16 RASJA.

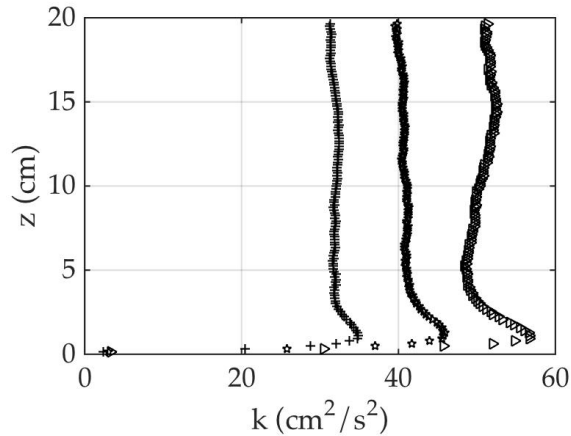


Figure 3.4: Turbulent kinetic energy profiles for  $\Phi_{on} = 6.25\%$ ,  $T_{on} = 4$  s (+), 6 s (☆), 8 s (▷), 8 x 8 RASJA.

### 3.2.1 8 x 8 RASJA

Turbulence generated by the 8 x 8 RASJA produces relatively constant  $k$  throughout most of the FOV, as shown in figure 3.4. As  $z$  decreases towards the bed, we observe a sharp increase in  $k$  until it peaks, approximately 1 cm above the bed. Below this height,  $k$  steeply approaches zero, consistent with observations of RMS velocity profiles and the no-slip boundary condition. This “bump” in  $k$  suggests that there is perhaps a local increase in pressure or other terms that are acting as an additional source of turbulence at the stationary bed, as even strong intercomponent energy transfer can (and typically does) result in constant turbulent kinetic energy. We will explore the possibility of such contributions in chapter 5. A summary of  $u'$ ,  $w'$ , and  $k$  are shown in table 3.5. Statistics are averaged across the mixed region, which will be characterized in Section 3.4.

$\Phi_{on}$ (%)	$T_{on}$ (s)	$u'$ ( $\frac{cm}{s}$ )	95% CI	$w'$ ( $\frac{cm}{s}$ )	95% CI	$k$ ( $\frac{cm^2}{s^2}$ )	95% CI
6.25	2	3.22	[3.21, 3.23]	3.88	[3.86, 3.89]	17.91	[17.82, 18.00]
6.25	3	3.74	[3.72, 3.75]	4.58	[4.56, 4.60]	24.46	[24.33, 24.58]
6.25	4	4.08	[4.06, 4.09]	5.53	[5.51, 5.55]	31.95	[31.79, 32.12]
6.25	5	4.16	[4.15, 4.18]	5.61	[5.59, 5.63]	33.11	[32.94, 33.28]
6.25	6	4.54	[4.52, 4.56]	6.32	[6.29, 6.34]	40.57	[40.37, 40.77]
6.25	8	5.19	[5.17, 5.21]	7.01	[6.98, 7.03]	51.47	[51.22, 51.73]
7.7	2	3.25	[3.23, 3.26]	3.86	[3.85, 3.88]	18.03	[17.93, 18.11]
7.7	3	3.81	[3.79, 3.82]	4.89	[4.87, 4.91]	26.45	[26.32, 26.59]
7.7	4	4.25	[4.24, 4.27]	5.82	[5.80, 5.84]	35.07	[34.90, 35.24]
7.7	5	4.39	[4.38, 4.41]	5.65	[5.63, 5.68]	35.31	[35.13, 35.49]
7.7	6	4.55	[4.53, 4.56]	6.37	[6.35, 6.40]	40.99	[40.78, 41.20]
7.7	8	5.00	[4.99, 5.02]	7.07	[7.04, 7.09]	50.04	[49.78, 50.29]
9.1	2	3.37	[3.36, 3.38]	3.89	[3.88, 3.90]	18.97	[18.87, 19.06]
9.1	3	3.86	[3.85, 3.88]	4.69	[4.67, 4.70]	25.94	[25.81, 26.08]
9.1	4	4.23	[4.21, 4.24]	5.57	[5.55, 5.59]	33.38	[33.21, 33.55]
9.1	5	4.48	[4.47, 4.50]	5.95	[5.93, 5.97]	37.80	[37.61, 37.99]
9.1	6	4.72	[4.70, 4.73]	6.54	[6.51, 6.56]	43.62	[43.40, 43.85]
9.1	8	4.99	[4.97, 5.01]	6.80	[6.78, 6.83]	48.07	[47.82, 48.32]
10.5	2	3.16	[3.15, 3.17]	3.61	[3.59, 3.62]	16.55	[16.46, 16.63]
10.5	3	3.96	[3.94, 3.97]	4.81	[4.80, 4.83]	27.26	[27.13, 27.40]
10.5	4	4.36	[4.34, 4.37]	5.88	[5.86, 5.90]	36.29	[36.11, 36.47]
10.5	5	4.57	[4.56, 4.59]	6.08	[6.06, 6.10]	39.42	[39.22, 39.62]
10.5	6	4.67	[4.65, 4.69]	6.41	[6.39, 6.43]	42.38	[42.16, 42.60]
10.5	8	5.14	[5.13, 5.16]	6.92	[6.90, 6.95]	50.43	[50.20, 50.67]
12.5	2	3.18	[3.16, 3.19]	3.51	[3.49, 3.52]	16.27	[16.19, 16.35]
12.5	3	3.92	[3.91, 3.94]	4.58	[4.57, 4.60]	25.93	[25.80, 26.06]
12.5	4	4.56	[4.54, 4.57]	5.85	[5.83, 5.87]	37.88	[37.69, 38.08]
12.5	5	4.59	[4.57, 4.61]	5.78	[5.76, 5.80]	37.81	[37.62, 38.01]
12.5	6	4.95	[4.93, 4.96]	6.41	[6.38, 6.43]	45.00	[44.77, 45.24]
12.5	8	5.15	[5.13, 5.17]	6.76	[6.74, 6.79]	49.42	[49.17, 49.68]

Table 3.5: Turbulent (RMS) velocities and turbulent kinetic energy. All values shown are the mean value of the statistic in the mixed region from PIV data.  $8 \times 8$  RASJA.

$\Phi_{on}$ (%)	$T_{on}$ (s)	$u'$ ( $\frac{cm}{s}$ )	95% CI	$w'$ ( $\frac{cm}{s}$ )	95% CI	$k$ ( $\frac{cm^2}{s^2}$ )	95% CI
3.1	0.8	4.61	[4.59, 4.63]	5.68	[5.66, 5.70]	37.49	[37.30, 37.69]
3.1	1.0	5.03	[5.01, 5.05]	6.25	[6.23, 6.27]	44.89	[44.65, 45.13]
3.1	1.2	5.51	[5.49, 5.53]	6.86	[6.84, 6.89]	53.99	[53.69, 54.29]
3.1	1.4	5.64	[5.62, 5.67]	7.33	[7.30, 7.35]	58.74	[58.41, 59.06]
3.1	1.6	5.97	[5.95, 6.00]	7.78	[7.75, 7.81]	65.98	[65.61, 66.34]

Table 3.6: Turbulent (RMS) velocities and turbulent kinetic energy. All values shown are the mean value of the statistic in the mixed region from PIV data. 16 x 16 RASJA.

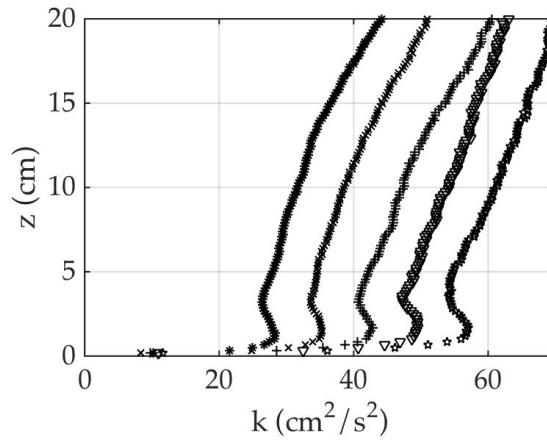


Figure 3.5: Turbulent kinetic energy profiles for  $\Phi_{on} = 3.1\%$ ,  $T_{on} = 0.8$  s (\*), 1.0 s (x), 1.2 s (+); 1.4 s ( $\nabla$ ), 1.6 s ( $\star$ ). 16 x 16 RAJSA.

### 3.2.2 16 x 16 RASJA

When using the 16 x 16 RASJA, similar behaviors are observed with the inter-component energy balance and structure of the turbulent kinetic energy profiles, as shown in figure 3.5. Interestingly, we no longer observe  $k$  independent of  $z$  in the FOV, and instead  $k$  decreases with  $z$  throughout much of the profile. The regions near the bed, however, behave very similarly to those observed with the 8 x 8 RASJA. We will revisit these observations throughout this chapter. A summary of  $u'$ ,  $w'$ , and  $k$  are shown in table 3.6.

### 3.3 Integral Scales

We compute the integral length scale,  $\mathcal{L}$ , as the characteristic length scale of the largest eddies of our turbulent flow. Although we discuss several available methods, our data lends itself best to the first, where an exponential curve fit is the basis for computing longitudinal and transverse integral length scales.

#### 3.3.1 Integral Length Scale - Exponential Curve Fit

Using PIV data at every height above the bed, we compute the spatial longitudinal autocorrelation function

$$a_{11,1}(r) = \frac{\langle u'(x_c - \frac{r}{2})u'(x_c + \frac{r}{2}) \rangle}{\left( \langle u'(x_c - \frac{r}{2})^2 \rangle \langle u'(x_c + \frac{r}{2})^2 \rangle \right)^{\frac{1}{2}}}$$

such that  $r$  is the spatial separation along the horizontal axis, as presented in Variano & Cowen (2008). Similarly, the transverse autocorrelation  $a_{33,1}(r)$  is computed as a function of  $w'$ . For sufficiently large measurement regions,  $a(r)$  converges to zero with increasing  $r$ , and the integral length scale can be computed directly as  $\mathcal{L}_L = \int a_{11,1}(r) dr$  at every height in the FOV. However, our FOV is too narrow to consistently capture this convergence, so we instead fit an exponential curve  $a_L(r) = e^{-\frac{r}{\mathcal{L}_L}}$  to the longitudinal autocorrelation data, as shown in figure 3.6, to determine the fit parameter  $\mathcal{L}_L$  in  $a_L(r)$  that best matches  $a_{11,1}(r)$ . This modeled curve fit consistently shows coefficient of determination  $R^2$  values of 0.99 between  $a_L(r)$  and  $a_{11,1}(r)$ , which demonstrates an excellent match to the autocorrelation data.

By assuming isotropy to address the transverse autocorrelation, we invoke

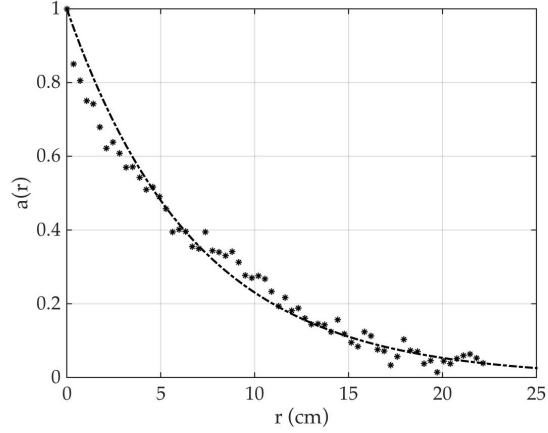


Figure 3.6: Exponential curve fit to autocorrelation function  $a_{11,1}$  (\*).  $T_{on} = 4s$ ,  $\Phi_{on} = 6.25\%$ ,  $z = 13.02$  cm,  $8 \times 8$  RASJA.

the relationship

$$a_{33,1}(r) = a_{11,1}(r) + \frac{1}{2}r \frac{\partial}{\partial r} a_{11,1}(r)$$

which is modeled as  $a_T(r) = e^{-\frac{r}{\mathcal{L}^*}} \left(1 - \frac{r}{2\mathcal{L}^*}\right)$  according to the exponential fit for  $a_L(r)$ . Using this model, we solve for  $\mathcal{L}^*$ , as  $\mathcal{L}_T = \frac{1}{2}\mathcal{L}^*$  from isotropy (Pope 2000). Although this is an appropriate assumption in the mixed region of the flow (to be discussed further in Section 3.4), this assumption is violated near the bed, in particular below the crossing point where  $u' > w'$  due to the kinematic boundary condition. However, the effect of using isotropy relationships near the bed remains unclear. The modeled curve fit, an example of which is shown in figure 3.7, has  $R^2$  values of 0.99. Summary longitudinal and transverse integral length scale profiles are shown in figure 3.8.

We consider the integral length scale of the turbulent flow to be equivalent to the longitudinal integral length scale, or  $\mathcal{L} = \mathcal{L}_{L,m}$ . In the mixed region, we consider the ratio of the longitudinal integral length scale to the transverse integral length scale to evaluate our assumption of isotropy. Having invoked the relationship between the transverse and longitudinal spatial autocorrelations

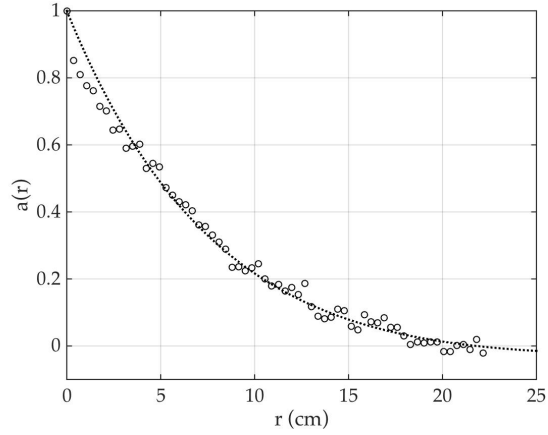


Figure 3.7: Fit of spatial transverse autocorrelation data  $a_{33,1}(r)$  ( $\circ$ ) to model fit. Sample data for  $T_{on} = 4\text{s}$ ,  $\Phi_{on} = 6.25\%$ ,  $z = 13.02\text{ cm}$ ,  $8 \times 8$  RASJA.

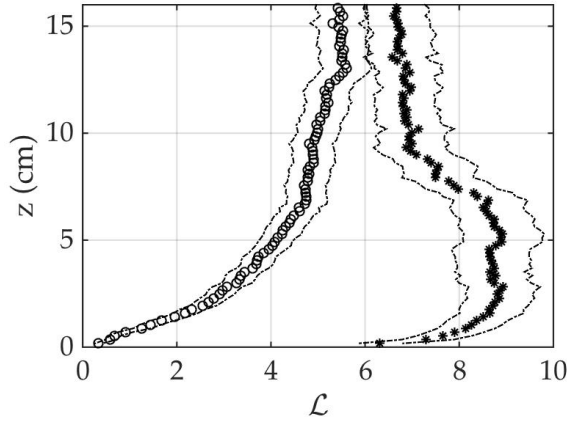


Figure 3.8: Profiles of  $\mathcal{L}_L$  (\*) and  $\mathcal{L}_T$  ( $\circ$ ) with 95% confidence intervals for  $T_{on} = 4\text{s}$ ,  $\Phi_{on} = 6.25\%$ ,  $8 \times 8$  RASJA.

as described, our assumption of isotropy at both small and energy-containing scales ought to lead us to the relationship  $\mathcal{L}_L/\mathcal{L}_T = 2$  (Pope 2000). However, the data produce a relationship of approximately  $\mathcal{L}_L/\mathcal{L}_T = 1.29$  in the mixed region across the 15 cases considered in the  $8 \times 8$  RASJA, which is consistent with the ratio of 1.19 reported in Variano & Cowen (2008).

### 3.3.2 Integral Length Scale - Bessel Function

An alternate method for finding  $\mathcal{L}$  again invokes the spatial autocorrelation. Instead of fitting an exponential curve to the autocorrelation, the modified Bessel function of the second-kind more accurately describes the theoretical shape of the expected curve, as described in Variano & Cowen (2013) and Bellani & Variano (2014). The fit

$$a(r) = \frac{2}{\Gamma\left(\frac{p-1}{2}\right)} \left( \frac{\sqrt{\pi}}{2} \frac{\Gamma\left(\frac{p}{2}\right)}{\Gamma\left(\frac{p-1}{2}\right)} \frac{r}{\mathcal{L}} \right)^{\frac{p-1}{2}} K_{\frac{p-1}{2}} \left( \sqrt{\pi} \frac{\Gamma\left(\frac{p}{2}\right)}{\Gamma\left(\frac{p-1}{2}\right)} \frac{r}{\mathcal{L}} \right)$$

relates  $\mathcal{L}$ ,  $a(r)$ , spectral slope  $p$ , modified Bessel function  $K$ , and gamma function  $\Gamma$ .

The Bessel function curve fit only applies in the inertial subrange, or  $\frac{\lambda}{2} < r < \frac{\mathcal{L}}{2}$  where  $\lambda$  describes the Taylor microscale (details presented in Section 4.2). This restricts the data to use approximately 10 points, depending on the experiment, in the autocorrelation function for the Bessel function fit. As a result, this method is more susceptible to noise than the exponential curve fit. A sample Bessel function fit is shown in figure 3.9 in comparison with the exponential curve fit, limited to  $r < \frac{\mathcal{L}}{2}$ . Resulting profiles of the integral length scale computed by these two methods are shown in figure 3.10. The increased noise in using the Bessel function, due to having fewer points for the curve fit, is apparent in these profiles. There are also notable qualitative differences in the profile shapes near the boundary. For this reason, we use the exponential fit as our preferred method for computing integral length scale in this facility.

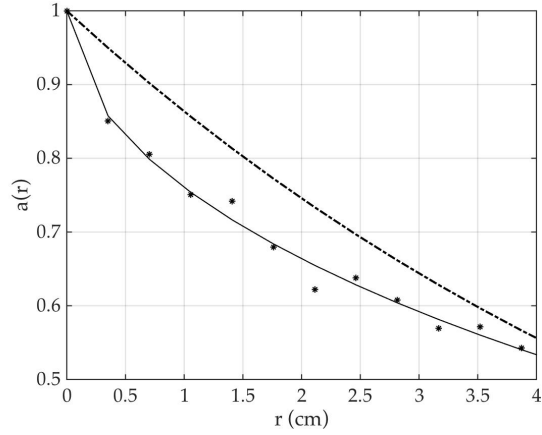


Figure 3.9: Bessel function (solid line) and exponential curve fit (dash-dotted line) to autocorrelation function  $a_{11,1}$  (\*).  $T_{on} = 4s$ ,  $\Phi_{on} = 6.25\%$ ,  $z = 13.02$  cm,  $8 \times 8$  RASJA.

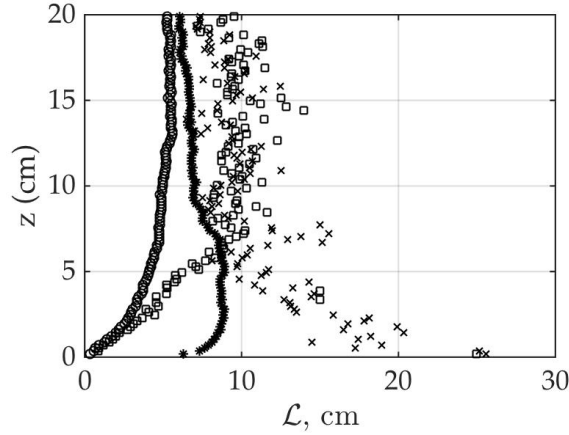


Figure 3.10: Integral length scale profile comparison between Bessel function and exponential curve fit.

### 3.3.3 Integral Length Scale - Scaling Law

For reference to other experimental and theoretical data, we also compute the integral length scale via the scaling determined relationship  $\mathcal{L}^* = \frac{k^{\frac{3}{2}}}{\varepsilon}$ , where  $\varepsilon$  is the dissipation rate of turbulent kinetic energy, to be discussed in depth in Chapter 4. As this is not a direct measurement of the integral length scale, it

results in values that are within the right order of magnitude of the exponential fit method. Results are included in table 3.7 and table 3.8.

### 3.3.4 Integral Length Scale Results

Although the integral length scale in experimental turbulence facilities is often thought to scale strictly with the grid spacing or other geometric constraints, as discussed in Hopfinger & Toly (1976), it has been shown that the integral length scale can be controlled by varying the parameters of an active grid in wind tunnel experiments (Makita 1991, Mydlarski & Warhaft 1996). Additionally, the integral length scale is strongly dependent upon distance from the grid in both GST (Thompson & Turner 1975) and moving-bed experiments (Thomas & Hancock 1977).

Indeed, we find that we are able to control  $\mathcal{L}$  by varying  $T_{on}$ , similar to the variation observed in RMS velocity and  $k$  computations. Longer  $T_{on}$  means the jets penetrate deeper into the flow, injecting more energy and controlling the degree of turbulent stirring. Therefore changing  $T_{on}$  is equivalent to changing the geometry within a facility, and is a suitable manner in which to vary  $\mathcal{L}$  using a single RASJA. Results from the 8 x 8 RASJA are summarized in table 3.7. From the 15 data points considered with the 8 x 8 RASJA, we find that  $\mathcal{L}^*$  is greater than  $\mathcal{L}_L$  by a factor of 3.32, on average.

Because the variations in  $T_{on}$  in the 16 x 16 RASJA are very small compared to those in the 8 x 8 RASJA, incremented by 0.2 s rather than 2 s, we do not observe discernible differences in the resulting integral length scale measured by the exponential fit to the autocorrelation function. Although  $\mathcal{L}_L$  does not

$\Phi_{on}$ (%)	$T_{on}$ (s)	$\mathcal{L}_L$ (cm)	95% CI	$\mathcal{L}_T$ (cm)	95% CI	$\mathcal{L}^* = \frac{k^{\frac{3}{2}}}{\epsilon}$ (cm)
6.25	4	6.80	[6.17, 7.50]	5.32	[4.86, 5.86]	21.66
6.25	6	7.44	[6.75, 8.22]	6.48	[5.96, 7.07]	26.10
6.25	8	9.71	[8.85, 10.64]	6.10	[5.60, 6.69]	30.30
7.7	4	7.01	[6.35, 7.70]	5.61	[5.10, 6.16]	27.51
7.7	6	7.22	[6.47, 7.92]	6.25	[5.68, 6.86]	25.50
7.7	8	7.83	[7.00, 8.52]	6.04	[5.52, 6.60]	27.29
9.1	4	6.56	[5.92, 7.21]	5.05	[4.57, 5.60]	20.34
9.1	6	7.79	[7.07, 8.60]	6.85	[6.29, 7.49]	24.71
9.1	8	7.37	[6.58, 8.08]	6.08	[5.58, 6.72]	25.87
10.5	4	6.43	[5.76, 7.02]	4.94	[4.54, 5.40]	20.66
10.5	6	7.64	[6.92, 8.35]	6.33	[5.81, 6.94]	23.03
10.5	8	9.00	[8.11, 9.88]	7.43	[6.83, 8.13]	36.66
12.5	4	6.81	[6.10, 7.45]	5.29	[4.78, 5.85]	21.02
12.5	6	7.71	[6.92, 8.46]	5.64	[5.16, 6.17]	23.44
12.5	8	8.74	[7.90, 9.56]	6.00	[5.51, 6.54]	25.32

Table 3.7: Integral length scale results, 8 x 8 RASJA.

$\Phi_{on}$ (%)	$T_{on}$ (s)	$\mathcal{L}_L$ (cm)	95% CI	$\mathcal{L}_T$ (cm)	95% CI	$\mathcal{L}^* = \frac{k^{\frac{3}{2}}}{\epsilon}$ (cm)
3.1	0.8	4.63	[4.29, 5.27]	3.59	[3.44, 4.16]	10.45
3.1	1.0	5.19	[4.71, 5.84]	3.83	[3.69, 4.49]	11.64
3.1	1.2	4.65	[4.29, 5.26]	3.57	[3.37, 4.20]	11.61
3.1	1.4	4.52	[4.21, 5.22]	4.41	[4.39, 5.37]	12.83
3.1	1.6	4.75	[4.37, 5.42]	4.53	[4.41, 5.38]	13.35

Table 3.8: Integral length scale results, 16 x 16 RASJA.

strictly increase with  $T_{on}$ , a trend of increasing  $\mathcal{L}^*$  is observed with  $T_{on}$ , and the incremental changes suggest that changing  $T_{on}$  should still result in changing integral length scale as long as the interval in  $T_{on}$  is sufficiently large. Due to the different general geometry and energetics of the flow between the two facilities, however, we do observe noticeably smaller  $\mathcal{L}$  in the 16 x 16 RASJA as compared to the 8 x 8 RASJA. Results with the 16 x 16 RASJA are summarized in table 3.8. The ratio of  $\mathcal{L}^*$  to  $\mathcal{L}_L$  measured in the 5 tests with the 16 x 16 RASJA is 2.53.

### 3.3.5 Integral Time Scale - Autocorrelation

Using ADV data, we can compute integral time scales in a similar manner to the integral length scale, such that  $T_{int} = \int \rho(\tau) d\tau$  where  $\rho(\tau) = \frac{\overline{u(t)u(t+\tau)}}{u'^2}$ . With resulting values of the integral time scale on the order of 1 s, we can smooth the temporal autocorrelation by generating ensemble averages based on shorter samples of the 30 minute temporal record. A sample temporal autocorrelation that has been ensemble averaged 9 times is shown in figure 3.11. It is symmetric, so half of the curve is pictured. Because the autocorrelation curve does not simply asymptote to zero, we include two metrics of the integral time scale. The first,  $T_{int,c}$ , is the integral under the entire one-sided curve. The second,  $T_{int,0}$ , is the integral under the entire one-sided curve until the first zero-crossing.

Using ensemble averaging highlights the inconsistencies with this method, as changing the number of ensemble averages dramatically alters the shape of the curve and location of zero crossings. Additionally, zero-crossings may not occur, as we see in one sample autocorrelation in figure 3.12. As a result,  $T_{int}$  varies greatly, depending on how many averages are used. Table 3.9 compares the number of ensemble averages with the resulting values of  $T_{int}$ . Because of the inconsistencies in this method, we do not use the temporal autocorrelation as a reliable means to computing the integral time scale.

### 3.3.6 Integral Time Scale - Scaling

Alternately, as in Peters (1999), we can estimate the integral time scale as

$$\tau_{int} = \frac{\mathcal{L}}{\sqrt{k}}$$

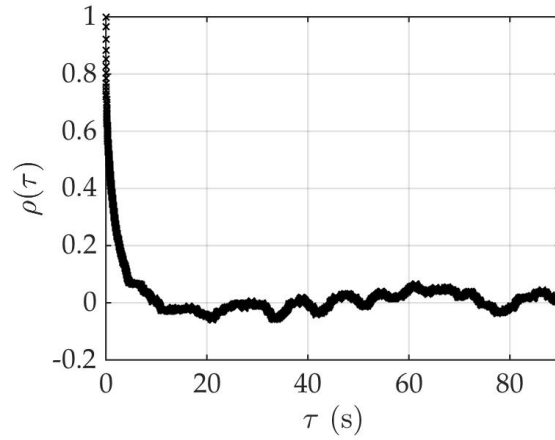


Figure 3.11: Sample temporal autocorrelation function from ADV data; 9 ensemble averages.

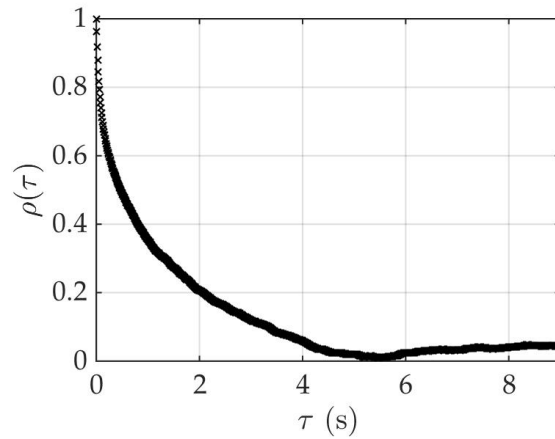


Figure 3.12: Sample temporal autocorrelation function from ADV data; 99 ensemble averages.

Number of ensemble averages	$T_{int,c}$ (s)	$T_{int,0}$ (s)
1	1.05	0.81
9	1.73	0.78
49	1.16	0.70
99	1.21	0.67

Table 3.9: Resulting  $T_{int}$  based on varying ensemble averaging intervals. Note: \* denotes that  $\rho(\tau)$  did not cross zero, so the integral was taken to the minimum of  $\rho(\tau)$ .

$\Phi_{on}$ (%)	$T_{on}$ (s)	$\tau_{int}$ (s)
6.25	4	1.20
6.25	6	1.17
6.25	8	1.35
7.7	4	1.18
7.7	6	1.13
7.7	8	1.11
9.1	4	1.14
9.1	6	1.18
9.1	8	1.06
10.5	4	1.07
10.5	6	1.17
10.5	8	1.27
12.5	4	1.11
12.5	6	1.15
12.5	8	1.24

Table 3.10: Integral time scale results, 8 x 8 RASJA.

$\Phi_{on}$ (%)	$T_{on}$ (s)	$\tau_{int}$ (s)
3.1	0.8	0.76
3.1	1.0	0.77
3.1	1.2	0.63
3.1	1.4	0.59
3.1	1.6	0.58

Table 3.11: Integral time scale result, 16 x 16 RASJA.

or the ratio of the integral length scale to the RMS turbulent velocity scale. Though not a direct method, it appears to be more consistent as it is based upon robust flow statistics. For the 15 cases considered with the 8 x 8 RASJA, we find an average  $\tau_{int}$  of 1.17 s, which is close to our PIV sampling frequency,  $F_s$  of 1 Hz that was selected to achieve independent samples. With the 16 x 16 RASJA,  $\tau_{int}$  lowers to 0.67 s. Interestingly, as shown in tables 3.10 and 3.11, there is no clear dependence of  $\tau_{int}$  on  $T_{on}$  as is observed in many of the other turbulence statistics.

## 3.4 Structure of Turbulence Facility

### 3.4.1 Boundary Layer and Tank Structure

Given the resulting profiles of RMS velocities, turbulent kinetic energy, and integral length scale, we can better understand the structure of the turbulence in the tank as it develops with distance from the jets and height above the bed. As shown in the caricature of the tank presented in figure 2.1, the tank is overall structured with a jet merging region, where the motion is dominated by the downward and upward momentum from individual jet activity, a mixed region, where the jet wakes are stirred into horizontally homogeneous nearly isotropic turbulence, and below, a bed-influenced region, where the flow is strongly altered due to its interaction with the bed. We find that when using the two different RASJAs, we observe all three of these regions, although there are additional details within and between these regions that we will present, based on each RASJA.

#### 8 x 8 RASJA

Profiles of  $u'$ ,  $w'$ , and  $k$  show a fairly straightforward structure of the turbulence facility with the 8 x 8 RASJA. We observe  $u'$  and  $k$  constant with  $z$  for much of the upper one-half to two-thirds of the FOV. If we also consider profiles of integral length scale, we observe  $\mathcal{L}_L$  nearly vertical for  $z > 1.5\mathcal{L}_L$ . This is the lower bound of our mixed region. As  $z$  increases above this height,  $u'$  continues to be relatively independent of  $z$ , and so it appears that in experiments with the 8 x 8 RASJA, the mixed region extends to the top of the FOV. We define metrics

with subscript  $m$  as the mean of those values in the mixed region; for example,  $u'_m$  is the mean of the horizontal RMS velocity in the mixed region.

In this region, we are interested in the isotropy of the turbulence. The ratio  $\frac{w'}{u'}$  provides a measure of isotropy, with a value of  $\frac{w'}{u'} = 1$  denoting isotropic turbulence. Though we do not achieve unity, we find a ratio  $\frac{w'}{u'} = 1.29$ , which is consistent with isotropy ratios observed in other facilities with forcing from only one side of the tank. Variano & Cowen (2008) found an isotropy ratio of 1.27, and several GST experiments found ratios of 1.1-1.3 (Hopfinger & Toly 1976) and 1.4 (McDougall 1979). Due to the forcing along the vertical axis in particular, one would expect to observe  $\frac{w'}{u'} > 1$  away from boundaries.

Moving lower in the FOV, the intercomponent energy transfer becomes stronger, as  $w'$  decays and  $u'$  increases due to the kinematic boundary condition and the inability of bed-normal motions to penetrate the boundary. Below a height of approximately  $z = 4$  cm,  $u'$  exceeds  $w'$ , where the flow becomes very anisotropic. The upper limit of the source region, where the flow becomes increasingly altered by the presence of the boundary with strong bed-parallel velocity fluctuations, is at the crossing point where  $u' = w'$ . Turbulent kinetic energy also increases towards the bed in this region. Between the source region and mixed region is a transition region, where  $u'$  weakly increases towards the bed. The lower limit of the source region is found where  $k$  and  $u'$  peak, roughly 1 cm above the bed, depending on the experiment.

Below the source region, velocity fluctuations decrease rapidly towards the bed. Certainly the no-slip viscous boundary condition causes velocity to approach zero at the bed, though the viscous sublayer does not extend all the way to the location of the peak of  $k$  and  $u'$ . This is our kinematic region, which is

comparable to the viscous region in Hunt & Graham (1978), though in our experiments it reaches beyond a true viscous region and to the height of active intercomponent energy transfer into turbulent splats (Perot & Moin, 1995a) due to the fluid interaction with the boundary.

### 16 x 16 RASJA

When using the 16 x 16 RASJA, the regions of flow are organized slightly differently. Recall that the 16 x 16 RASJA is non-dimensionally “deeper,” with  $\frac{H}{\delta} = 13$ , compared to  $\frac{H}{\delta} = 7.1$  with the 8 x 8 RASJA. The bed-influenced regions behave similarly to those described for the 8 x 8 RASJA, with strong anisotropy and bed-parallel RMS velocities due to turbulent splats. The kinematic region is again found between the bed and the location of the peak in  $u'$  and  $k$ . The source region exists between the crossing point where  $u' = w'$  and the peak in  $u'$ .

Above the source region, the flow transitions to the mixed region, which is again found to have a lower bound at  $z = 1.5\mathcal{L}_L$ . Interestingly, although  $u'$  is constant in this range,  $k$  decreases with distance from the jets. We will explore this further in the coming subsection. Above the mixed region, there is a decay in  $u'$ ,  $w'$ , and  $k$  with  $z$ . This is noticeably different between the two RASJAs, as shown in figures 3.4 and 3.5. As we do not make measurements more than 20 cm above the bed, it is unclear whether there would be an additional mixed region above the decay, or whether the jet merging region transitions directly to the decay region. Regardless, we are interested in exploring the rate of decay observed with the 16 x 16 RASJA and in characterizing the turbulence in the mixed region directly above the boundary layer.

### 3.4.2 Decay of Turbulence away from the Source

Recalling the decay relationship proposed by Hopfinger & Toly (1976) that suggests that turbulence facilities with turbulence generated by oscillating grids or random jet arrays should show decay of  $u'$  and  $w'$  away from the source, we draw comparisons between the results obtained in our two facilities to determine the relevance of the concept of decay away from the RASJAs.

As shown in figures 3.13 and 3.14, turbulent decay is not always an accurate representation of the observations in a facility with an oscillating grid or random jet array. For experiments with the 8 x 8 RASJA, with  $\frac{H}{J} = 7$ , both  $u'$  and  $w'$  are nearly independent of  $z$  as discussed previously. However, with the 16 x 16 RASJA, with  $\frac{H}{J} = 13$ , there is a much clearer region of decay for both  $u'$  and  $w'$  that closely aligns with the Hopfinger & Toly (1976) relationship for  $\frac{z}{H} > 0.15$ . Although figures 3.13 and 3.14 only show one profile from each RASJA, all curves collapse well within their facility. Because the two RASJA experiments shown have similar values of  $k$ ,  $u'$ , and  $w'$  near the bed, the flow structure of the facility appears more closely linked to the proximity of the turbulence source to the bed, or rather, the ratio  $\frac{H}{J}$ .

The expected decay in GST theory also neglects the enhancement of  $u'$  at the no-slip boundary that we observe in figure 3.13, or the viscous decay of either  $u'$  or  $w'$  at the bed, as observed in figure 3.14. Instead, our data from both experiments are better aligned with the experimental GST results of Brumley & Jirka (1987) and theory of Hunt & Graham (1978) in the measurement region considered, even though the Brumley & Jirka (1987) experiments consider the mean shear free turbulent boundary layer at a free surface rather than a flat plate. A free surface differs from a flat plate boundary in that there is free slip

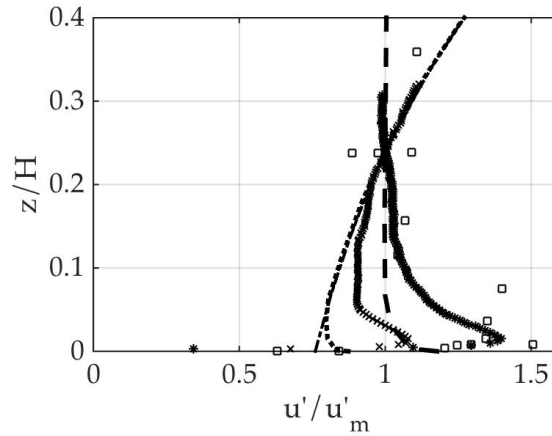


Figure 3.13: Comparison of experimental  $u'$  data.  $T_{on} = 4$  s,  $\Phi_{on} = 6.25\%$ ,  $8 \times 8$  RASJA (\*),  $T_{on} = 0.8$  s,  $\Phi_{on} = 3.1\%$ ,  $16 \times 16$  RASJA (x) with Brumley & Jirka (1987) GST data ( $\square$ ), Hopfinger & Toly (1976, dash-dot), and Hunt & Graham (dashed line). Vertical axis normalized by jet height  $H = 71$  cm and  $H = 65$  cm for  $8 \times 8$  and  $16 \times 16$  RASJAs, respectively; horizontal axis normalized to average 1 at  $\frac{z}{H} = 24\%$ , as in Brumley & Jirka (1987).

and a deformable free surface, leading to potentially weaker intercomponent energy transfer near the surface and weaker viscous decay to zero at the surface itself. Even with these differences, the Brumley & Jirka (1987) experiments show a significant transfer of energy from surface-normal to surface-parallel, with  $\frac{u'}{u'_m}$  values around 1.4, compared to 0.8 predicted by the combined Hopfinger & Toly (1976) and Hunt & Graham (1978) theories.

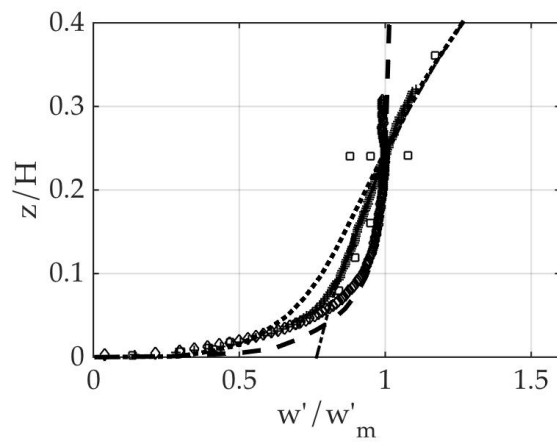


Figure 3.14: Profiles of experimental  $w'$  data.  $T_{on} = 4$  s,  $\Phi_{on} = 6.25\%$ ,  $8 \times 8$  RASJA ( $\diamond$ ),  $T_{on} = 0.8$  s,  $\Phi_{on} = 3.1\%$ ,  $16 \times 16$  RASJA (+). See previous figure for legend of remaining data.

## CHAPTER 4

### TURBULENT KINETIC ENERGY BALANCE

In order to understand the dynamics and energy balance of the unique boundary layer that forms without a mean flow or mean bed shear, we look to the turbulent kinetic energy budget. In channel flow, one would expect to see a balance between the dissipation rate and production of  $k$  in the boundary layer, as shown in figure 4.1. Turbulent transport and viscous diffusion are also important, with the latter of particular significance at the wall, where it balances dissipation. Pressure diffusion is an order of magnitude smaller than dissipation and production, and we observe pressure, production, and turbulent transport equal to zero at the wall.

However, in absence of a mean flow, we will observe much different effects. Starting from the full turbulent kinetic energy equation,

$$\frac{\partial k}{\partial t} + \langle U_j \rangle \frac{\partial k}{\partial x_j} = -\frac{1}{\rho_0} \frac{\partial \langle u_i p \rangle}{\partial x_i} - \frac{1}{2} \frac{\partial \langle u_j u_j u_i \rangle}{\partial x_i} + \nu \frac{\partial^2 k}{\partial x_j^2} - \langle u_i u_j \rangle \frac{\partial \langle U_i \rangle}{\partial x_j} - \nu \left\langle \frac{\partial u_i \partial u_i}{\partial x_j \partial x_j} \right\rangle$$

we aim to understand the balance of unsteady turbulent kinetic energy, advection, pressure diffusion, turbulent transport, molecular viscous transport, production, and dissipation in a mean shear free boundary layer above a solid boundary. With continuous turbulent forcing,  $k$  is stationary in time. We first explore several methods of measuring the dissipation rate  $\varepsilon$  of turbulent kinetic energy, several of which depend strictly on isotropy. Perfect isotropy does not exist in our flow, nor in many other flows where it is assumed to exist, so we are able to compare these computation methods and to evaluate the remaining terms in the energy balance. In this chapter, all results are presented for the 8 x 8 RASJA above a solid boundary.

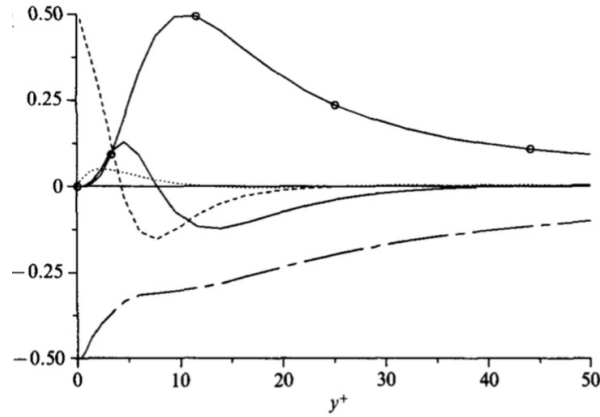


Figure 4.1: Turbulent kinetic energy balance in a turbulent boundary layer driven by a mean flow on a flat plate, normalized by  $2k$ , reproduced from Spalart (1988). Dissipation (dash-dotted line), production (o-), turbulent diffusion (solid line), viscous diffusion (dashed line), pressure (dotted line).

## 4.1 Dissipation

### 4.1.1 Scaling Law

The order of magnitude of  $\varepsilon$  can be estimated based on scaling arguments by  $\varepsilon_{sc} = C_\varepsilon \frac{(\frac{2}{3}k)^{\frac{3}{2}}}{\mathcal{L}}$ , using  $k = k_m$  and  $\mathcal{L} = \mathcal{L}_m$ . The empirical constant  $C_\varepsilon$  is of order 1, though a value of 0.5, as found in Pearson et al. (2002), Burattini et al. (2005), and Variano & Cowen (2008), shows closer agreement in magnitude with the dissipation measurements below, as shown in table 4.1.

### 4.1.2 Second-Order Structure Function

We can also determine the dissipation rate with the longitudinal second-order structure function  $D_{LL}(x, r) = \langle [U(x_c - \frac{r}{2}) - U(x_c + \frac{r}{2})]^2 \rangle$  at every height in the

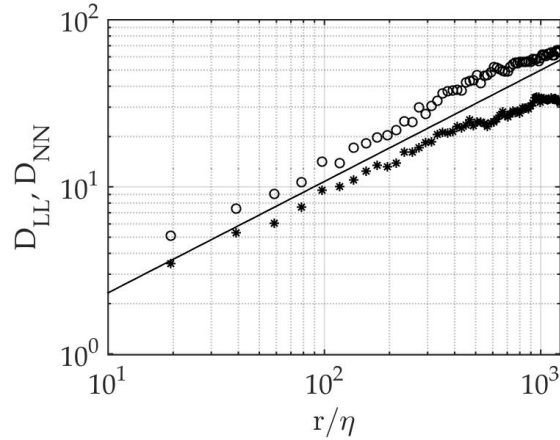


Figure 4.2: Second-order structure functions  $D_{LL}$  (\*) and  $D_{NN}$  (o) plotted against  $2/3$  slope.  $T_{on} = 4s$ ,  $\Phi_{on} = 6.25\%$ ,  $z=10.45cm$ ,  $8 \times 8$  RASJA.

FOV in which  $r$  denotes the horizontal separation distance between the two points in each computation and  $x_c$  describes the centerline  $x = 0$ . Dissipation is then found via  $\varepsilon(r) = \frac{1}{r}(\frac{D_{LL}}{C_2})^{\frac{3}{2}}$  with constant  $C_2 = 2.0$  (Pope 2000). We can directly compute  $D_{NN}$  as the second-order transverse structure function from  $W$ , using a lateral separation  $r$ , adjusting the relationship to  $\varepsilon(r) = \frac{1}{r}(\frac{3}{4}\frac{D_{NN}}{C_2})^{\frac{3}{2}}$  by assuming local isotropy and invoking the relationship between the transverse and longitudinal structure functions  $D_{NN} = \frac{4}{3}D_{LL}$  (Pope 2000). These relationships apply in the inertial subrange such that  $\mathcal{L} \gg r \gg \eta$  where  $\eta$  represents the Kolmogorov lengthscale  $\eta \equiv (\frac{\nu^3}{\varepsilon})^{\frac{1}{4}}$ . For our data, we are interested in the approximate range  $500 \gg \frac{r}{\eta} \gg 1$  where the compensated structure functions are suitable for estimating dissipation. Sample second-order structure functions are shown in figure 4.2.

### 4.1.3 Direct Method

The direct formulation is an alternate method for computing dissipation via  $\varepsilon \equiv 2\nu \langle S_{ij} S_{ij} \rangle$ , with  $S_{ij} \equiv \frac{1}{2} \left( \frac{\partial u_i}{\partial x_j} + \frac{\partial u_j}{\partial x_i} \right)$ . This method is advantageous in that there are no empirical constants or isotropy requirements. We know that the flow is very anisotropic near the bed, as is evident when considering the intercomponent transfer from  $w'$  to  $u'$  presented in figure 3.2. Although the flow is more isotropic in the mixed region, we still observe weak anisotropy even in the mixed region, due to the vertical forcing of the facility. Thus, we cannot precisely assume that horizontal and vertical statistics are equivalent, which is a key requirement in the previous methods.

Because we can only directly measure  $\frac{\partial u}{\partial x}$ ,  $\frac{\partial u}{\partial z}$ ,  $\frac{\partial w}{\partial x}$ , and  $\frac{\partial w}{\partial z}$  from PIV data, we invoke continuity, as in Cowen & Monismith (1997) and Doron et al. (2001), such that

$$\begin{aligned} \overline{\left(\frac{\partial v}{\partial y}\right)^2} &= \overline{\left(-\frac{\partial u}{\partial x} - \frac{\partial w}{\partial z}\right)^2} = \overline{\left(\frac{\partial u}{\partial x}\right)^2} + \overline{\left(\frac{\partial w}{\partial z}\right)^2} + 2\overline{\left(\frac{\partial u}{\partial x} \frac{\partial w}{\partial z}\right)} \\ \overline{\left(\frac{\partial v}{\partial y}\right)^2} &= \overline{\left(-\frac{\partial u}{\partial x} - \frac{\partial w}{\partial z}\right)^2} = \overline{\left(\frac{\partial u}{\partial x}\right)^2} + \overline{\left(\frac{\partial w}{\partial z}\right)^2} + 2\overline{\left(\frac{\partial u}{\partial x} \frac{\partial w}{\partial z}\right)} \end{aligned}$$

Radial symmetry allows for substitutions  $\frac{\partial v}{\partial x} = \frac{\partial u}{\partial x}$ ,  $\frac{\partial u}{\partial y} = \frac{\partial u}{\partial x}$ ,  $\frac{\partial v}{\partial z} = \frac{\partial u}{\partial z}$ , and  $\frac{\partial w}{\partial y} = \frac{\partial w}{\partial x}$ , which simplifies the dissipation formula to

$$\varepsilon = 2\nu \left[ 4\overline{\left(\frac{\partial u}{\partial x}\right)^2} + \overline{\left(\frac{\partial u}{\partial z}\right)^2} + \overline{\left(\frac{\partial w}{\partial x}\right)^2} + 2\overline{\left(\frac{\partial w}{\partial z}\right)^2} + 2\overline{\left(\frac{\partial u}{\partial x} \frac{\partial w}{\partial z}\right)} + 2\overline{\left(\frac{\partial u}{\partial z} \frac{\partial w}{\partial x}\right)} \right]$$

to fully capture dissipation from 2D PIV measurements. The cross terms,  $\overline{\left(\frac{\partial u}{\partial x} \frac{\partial w}{\partial z}\right)}$  and  $\overline{\left(\frac{\partial u}{\partial z} \frac{\partial w}{\partial x}\right)}$ , only account for approximately 3% of the total dissipation in the direct method, which is reasonable given that the flow is nearly isotropic in the mixed region and diagonal elements of  $S_{ij}$  dominate.

Spatial resolution is of critical importance in using the direct method, as noise is amplified if the resolution is refined beyond the particle motions, and large PIV analysis grids average the turbulent motions causing an underestimation of the dissipation rate. Given a spatial resolution of  $9\eta$ , an integration of the universal spectrum in Pao (1965) suggests that computing the spatial derivatives directly from our PIV data is sufficient for capturing 92% of the total dissipation with the direct method (Cowen & Monismith 1997). Thus, resulting values are scaled up by a factor of 1.09, bringing our estimate to 100%, as shown in table 4.1.

We find that the direct method with a correction factor provides the best estimate for dissipation in these experiments, as it requires the fewest assumptions about the flow. The anisotropy near the bed is apparent in figure 4.5 when comparing longitudinal and transverse structure functions. Whereas the longitudinal method effectively captures the increase in dissipation near the bed shown in the direct method, the transverse measurements approach zero. For the duration of this paper, we will use  $\varepsilon_m$  as the mean of the dissipation rate in the mixed region as computed from the corrected direct method.

#### 4.1.4 Spatial Spectra

We also explore the use of spatial spectra from PIV to compute dissipation. Since spatial spectra require a complete spatial record, Delaunay triangulation is used to linearly interpolate filtered data. We use the relation

$$\varepsilon = \left( \frac{G_{uu}(\chi) \chi^{\frac{5}{3}}}{C_1} \right)^{\frac{3}{2}}$$

$\Phi_{on}$ (%)	$T_{on}$ (s)	Scaling ( $\frac{cm^2}{s^3}$ )	$D_{LL}$ ( $\frac{cm^2}{s^3}$ )	$D_{NN}$ ( $\frac{cm^2}{s^3}$ )	Direct ( $\frac{cm^2}{s^3}$ )	$G_{uu}$ ( $\frac{cm^2}{s^3}$ )	$G_{ww}$ ( $\frac{cm^2}{s^3}$ )
6.25	4	7.32	5.23	6.39	8.34	12.88	15.66
6.25	6	9.47	6.80	7.86	9.90	18.28	21.73
6.25	8	10.21	9.32	12.07	12.19	28.18	32.22
7.7	4	8.09	5.67	7.17	7.55	9.40	12.64
7.7	6	10.11	7.73	8.88	10.29	20.37	23.54
7.7	8	11.98	9.46	11.06	12.97	28.84	34.54
9.1	4	7.86	6.19	7.60	9.48	15.91	18.36
9.1	6	10.08	7.99	9.36	11.66	26.00	28.93
9.1	8	12.10	9.20	11.20	12.88	32.25	35.31
10.5	4	8.82	6.50	7.72	10.58	17.24	20.64
10.5	6	9.82	7.63	9.41	11.98	24.42	27.73
10.5	8	10.52	8.18	9.59	9.77	13.99	17.36
12.5	4	8.71	7.41	8.02	11.09	20.47	22.14
12.5	6	10.38	9.16	9.63	12.88	30.55	31.78
12.5	8	10.63	9.78	11.21	13.72	33.62	35.94

Table 4.1: Resulting dissipation values computed from various methods, averaged in the mixed region,  $8 \times 8$  RASJA.

with one-sided longitudinal spatial spectrum  $G_{uu}(\chi)$  and wavenumber  $\chi$  (Pope 2000). Coefficient  $C_1 = \frac{1}{2} \frac{18}{55} \alpha$  for longitudinal measurements, with  $\alpha = 1.5$ . Assuming isotropy, a similar relation exists for transverse spatial spectrum  $G_{ww}(\chi)$  with coefficient  $C'_1 = \frac{4}{3} C_1$ . The plateau of the function gives a measurement of  $\varepsilon$  at every height  $z$  from both longitudinal and transverse spatial spectra, an example of which is shown in figure 4.3.

Dissipation estimates from compensated spatial spectra consistently overestimate dissipation rates computed by more robust methods such as second-order structure function fits and direct measurements (Doron et al. 2001, de Jong et al. 2009). Because this method of computing dissipation is the only one of the methods explored in this dissertation that requires interpolation, we explore the effects of interpolation on the other methods to better understand the effects of interpolation. When using interpolated data to compute dissipation from the

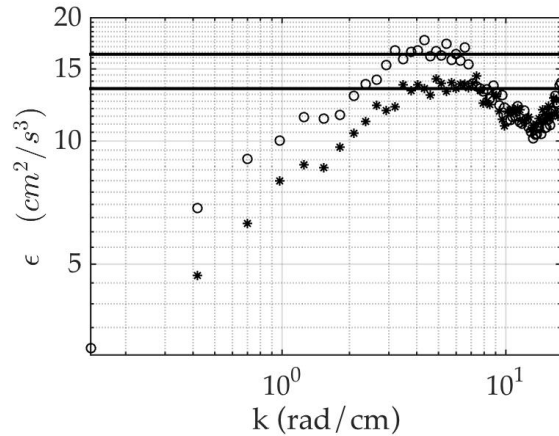


Figure 4.3: Compensated one-side spatial spectra.  $G_{uu}$  (\*),  $G_{ww}$  ( $\circ$ ). Example for  $T_{on} = 4s$ ,  $\Phi_{on} = 6.25\%$ ,  $8 \times 8$  RASJA.

direct method, we see a 30-40% increase in the mixed region, as shown in the example in figure 4.4. Similarly, the second-order structure function estimates increase by 20-40% in the mixed region. Therefore, it seems likely that a portion of the overestimation in the dissipation rate computed by compensating spatial spectra is due to interpolation.

#### 4.1.5 Eulerian Frequency Spectra

Whereas several methods are available from which to compute dissipation rates from spatial PIV data, it would be valuable to further develop methods of determining dissipation from point measurements such as ADV. Such instruments are typically more readily deployable in field experiments or in laboratory setups with limited visual access. Without a mean flow, we are unable to convert temporal records to spatial records via Taylor's frozen turbulence hypothesis, and so we instead turn to Eulerian frequency spectra (Tennekes 1975).

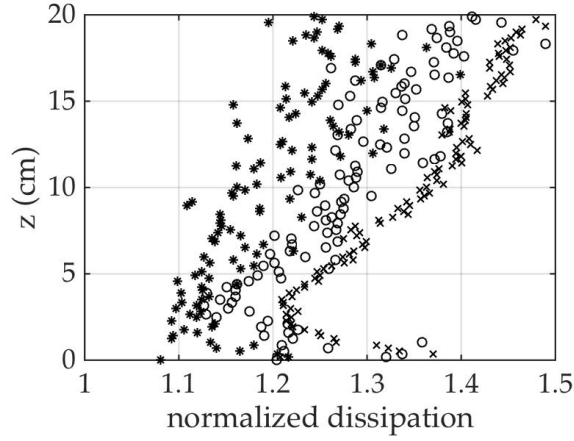


Figure 4.4: Increase in dissipation estimate resulting from interpolating in data via Delaunay triangulation. Profiles are normalized by un-interpolated data via the same method (i.e.  $D_{LL}$  ratio is  $D_{LL}$  (interpolated) to  $D_{LL}$  (un-interpolated)).  $D_{LL}$  (\*),  $D_{NN}$  (o), direct method (x). Sample profiles shown for  $T_{on} = 4s$ ,  $\Phi_{on} = 6.25\%$ , 8 x 8 RASJA.

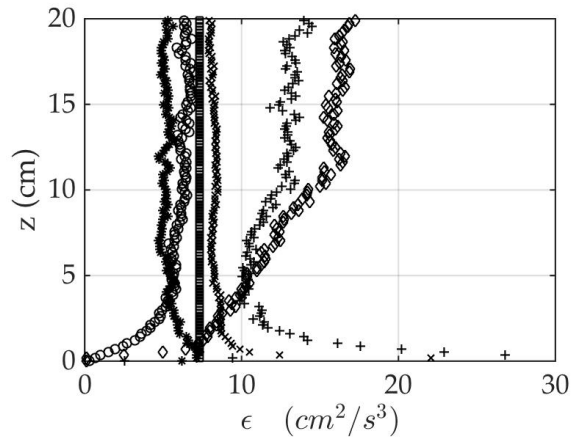


Figure 4.5: Method comparison of dissipation profiles. Scaling law (square),  $D_{LL}$  (\*),  $D_{NN}$  (o), direct method (x),  $S_{uu}$  (+),  $S_{ww}$  ( $\diamond$ ). Sample profiles shown for  $T_{on} = 4s$ ,  $\Phi_{on} = 6.25\%$ , 8 x 8 RASJA.

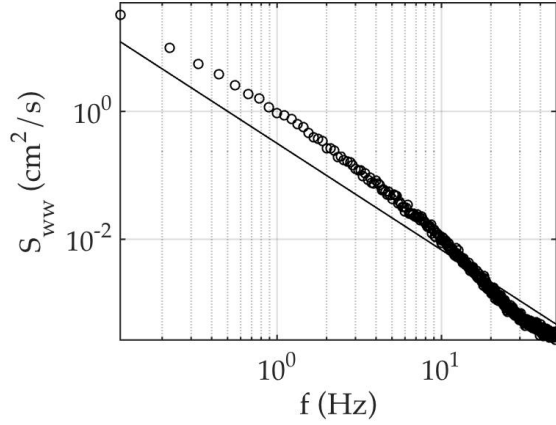


Figure 4.6: Frequency spectra from 100 Hz ADV measurement at  $z = 12$  cm, 200 ensemble averages.  $T_{on} = 4s$ ,  $\Phi_{on} = 6.25\%$ ,  $8 \times 8$  RASJA.

Temporal frequency spectra, shown in figure 4.6, are computed from 100 Hz ADV records taken in the mixed region at a point  $z = 12$  cm above the bed. Although the spectra are only plotted up to the Nyquist frequency, all frequency spectra shown are normalized such that the integral of the spectra over  $\omega \in (-\infty, \infty)$  are equal to the variance of the velocity signal. The  $S_{ww}$  spectra are least affected by noise in the configuration used, due to the geometric considerations of the ADV, as is evident by the elevated noise tails of  $S_{uu}$  and  $S_{vv}$  in figure 2.9, so we are only considering the bed-normal velocity spectra in the coming analysis.

Through a simple scaling of  $2\pi$ , temporal frequency spectra are transformed into Eulerian frequency spectra; a sample compensated Eulerian frequency spectrum is shown in figure 4.7. By identifying the plateau of the compensated spectrum, we utilize the relationships introduced by Tennekes (1975)

$$E(\omega) = B_0 \varepsilon^{\frac{2}{3}} \left( \sqrt{2k} \right)^{\frac{2}{3}} \omega^{-\frac{5}{3}}$$

and further developed by Kit et al. (1995) as

$$E(\omega) = B_1 \varepsilon^{\frac{2}{3}} w'^{\frac{2}{3}} \omega^{-\frac{5}{3}}$$

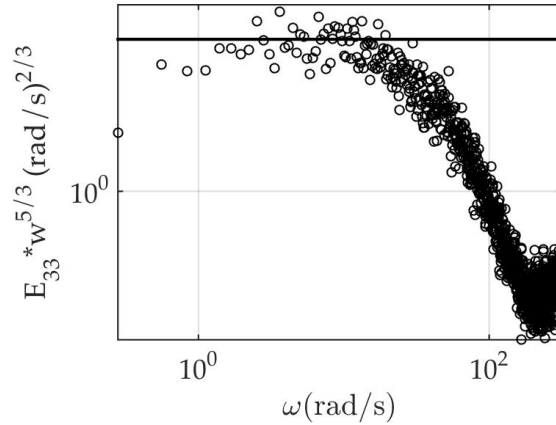


Figure 4.7: Eulerian frequency spectrum of vertical velocity from 100 Hz ADV measurement at  $z = 12$  cm, 80 ensemble averages.  $T_{on} = 4$ s,  $\Phi_{on} = 6.25\%$ ,  $8 \times 8$  RASJA.

to deduce the empirical constants  $B_0$  and  $B_1$  that relate dissipation to the Eulerian frequency spectra.

Few experimental studies have been conducted to determine the empirical fit coefficients. In GST studies, DeSilva & Fernando (1994) found a value of  $B_1 = 8$ . In these experiments RMS velocities were estimated by the Hopfinger-Toly (1976) equations and scaling arguments rather than measured directly in the facility. Later GST experiments by Kit et al. (1995) used a two-component fiber optic laser Doppler velocimeter and reported a value of coefficient  $B_1 = 0.7$  for vertical velocity records after using isotropic strain rate relationships to determine the dissipation rate from the vertical velocity records. Variano & Cowen (2008) reported  $B_0 = 0.23$  and  $B_1 = 0.35$  for a vertical velocity time series, with dissipation rates computed from the second-order longitudinal structure function and RMS velocities computed from PIV measurements and turbulent spectra computed from ADV data.

To compute current estimates of  $B_0$  and  $B_1$ , our dissipation estimate comes

from the corrected direct method using PIV data, whereas  $E(\omega)$ ,  $w'$ , and  $k$  come directly from ADV measurements. Resulting values of  $B_0 = 0.14$  and  $B_1 = 0.19$  satisfy the Tennekes (1975) and Kit et al. (1995) models, respectively, for vertical velocity measurements.

## 4.2 Production

Because the spatial resolution of the analyzed PIV data is sufficient to directly compute spatial derivatives for higher-order statistical analysis such as dissipation, we can also directly compute production,  $P$ , and the remaining terms in the turbulent kinetic energy balance.  $P = -\langle u_i u_j \rangle \frac{\partial \langle U_i \rangle}{\partial x_j}$ , expands to

$$P = - \left[ 4 \langle uu \rangle \frac{\partial \langle U \rangle}{\partial x} + 2 \langle uw \rangle \frac{\partial \langle U \rangle}{\partial z} + 2 \langle uw \rangle \frac{\partial \langle W \rangle}{\partial x} + \langle ww \rangle \frac{\partial \langle W \rangle}{\partial z} \right]$$

by invoking radial symmetry. In figure 4.8, we consider each of the  $\langle u_i u_j \rangle$  terms. Whereas  $\langle uu \rangle$  and  $\langle ww \rangle$  have significant magnitudes, as expected,  $\langle uw \rangle$  is nearly zero. Figure 4.9 shows the mean velocity gradients. Due to horizontal homogeneity, we observe negligible contributions from  $\frac{\partial \langle U \rangle}{\partial x}$  and  $\frac{\partial \langle W \rangle}{\partial x}$ . There are, however, weak contributions from the vertical gradients of both horizontal and vertical mean velocities.

When combining the products of the mean velocity gradients and  $\langle u_i u_j \rangle$  terms, the summation ultimately results in low levels of production. For all 30 original trials with the  $8 \times 8$  RASJA,  $P$  is approximately zero at the bed. For the trials explored with  $M^* < 1\%$ , production remains negligible near the bed and in the mixed region, though not all 15 trials show such small values of  $P$  throughout the boundary layer. While more than half of these trials show near-zero magnitudes of production, an example of which is shown in figure 4.10,

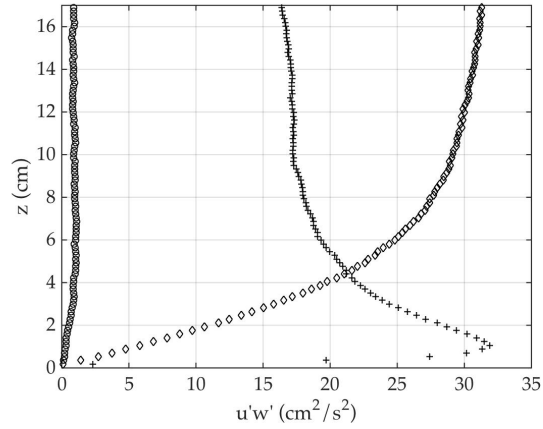


Figure 4.8: Profiles of  $\overline{u_i u_j}$  terms in the production equation.  $\overline{u'u'}$  (+),  $\overline{u'w'}$  (o),  $\overline{w'w'}$  (◇)  $T_{on} = 4s$ ,  $\Phi_{on} = 6.25\%$ ,  $8 \times 8$  RASJA.

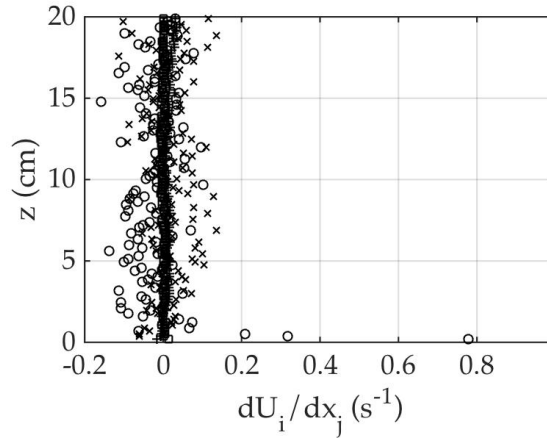


Figure 4.9: Contributions from mean velocity gradients in the production equation.  $\frac{\partial \langle U \rangle}{\partial x}$  (□),  $\frac{\partial \langle U \rangle}{\partial z}$  (o),  $\frac{\partial \langle W \rangle}{\partial x}$  (+),  $\frac{\partial \langle W \rangle}{\partial z}$  (x).  $T_{on} = 4s$ ,  $\Phi_{on} = 6.25\%$ ,  $8 \times 8$  RASJA.

other trials exhibit weak production in the source layer ranging from 2 to  $6 \frac{cm^2}{s^3}$ , as shown in figure 4.11. Looking at the individual components, it appears that non-zero production results from non-zero  $\frac{\partial \langle U \rangle}{\partial x}$  in particular.

Despite non-negligible values of  $P$  shown in the latter profile, the values of production obtained remain small in comparison to dissipation. Whereas

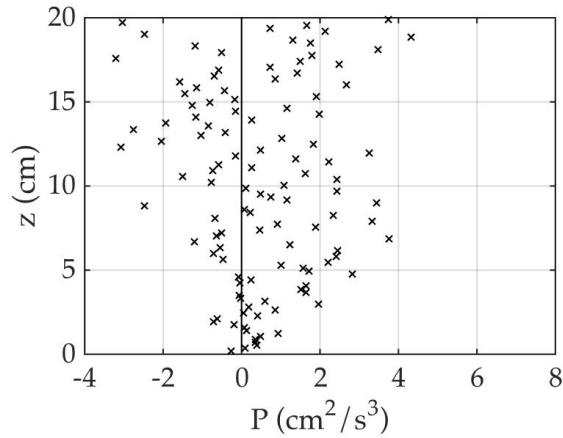


Figure 4.10: Sample profile for which production contributes minimally to turbulent kinetic energy balance.  $T_{on} = 4\text{s}$ ,  $\Phi_{on} = 6.25\%$ ,  $8 \times 8$  RASJA.

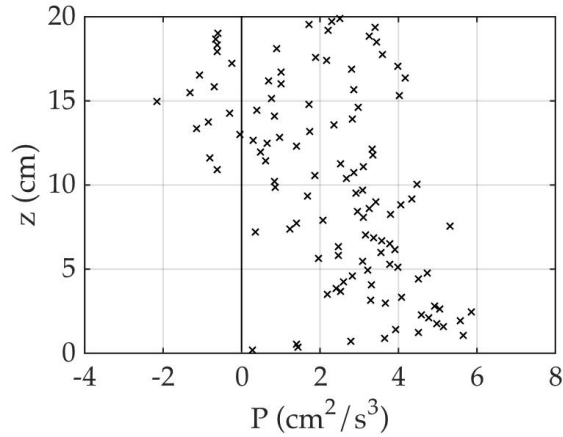


Figure 4.11: Sample profile for which production is not negligible.  $T_{on} = 4\text{s}$ ,  $\Phi_{on} = 7.7\%$ ,  $8 \times 8$  RASJA.

production and dissipation are typically in balance in the near-wall region in boundary layers resulting from mean flows, the magnitude of production is at most half as great as the magnitude of dissipation and is typically negligible. Figure 4.14 shows the sample relative contributions of production and dissipation (and the remaining terms in the energy balance) for the case of near-zero production.

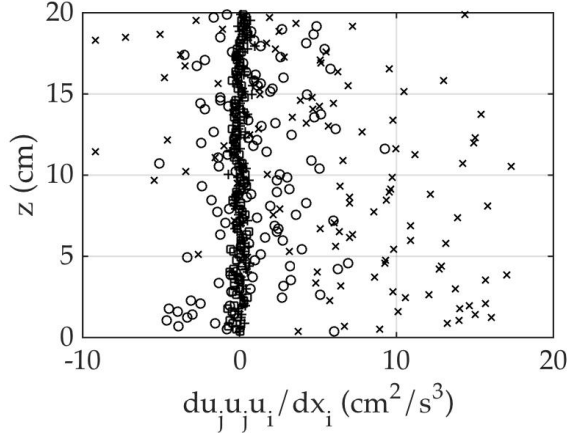


Figure 4.12: Contributions of triple correlation terms,  $\frac{\partial \overline{u_j u_j u_i}}{\partial x_i}$ , to turbulent transport.  $T_{on} = 4s$ ,  $\Phi_{on} = 6.25\%$ ,  $8 \times 8$  RASJA.

### 4.3 Turbulent Transport

Considering the triple correlation,  $T = -\frac{1}{2} \frac{\partial \langle u_j u_j u_i \rangle}{\partial x_i}$ , we invoke radial symmetry to simplify our equation to

$$T = -\frac{1}{2} \left[ 4 \frac{\partial \langle uuu \rangle}{\partial x} + 2 \frac{\partial \langle wwu \rangle}{\partial x} + 2 \frac{\partial \langle uuw \rangle}{\partial z} + \frac{\partial \langle www \rangle}{\partial z} \right]$$

which we calculate directly from PIV data. In doing so, we find negligible contributions from the  $\frac{\partial}{\partial x}$  terms, as is expected from horizontal homogeneity, as shown in figure 4.12. The triple correlation is an inherently noisy calculation, with relatively wide fluctuations throughout the FOV, so a local median smoothing filter is later applied to the final profile of  $T$  shown in figure 4.14. This is done via MATLAB's `medfilt1` function, a one-dimensional median filter, along 6 point-long segments.

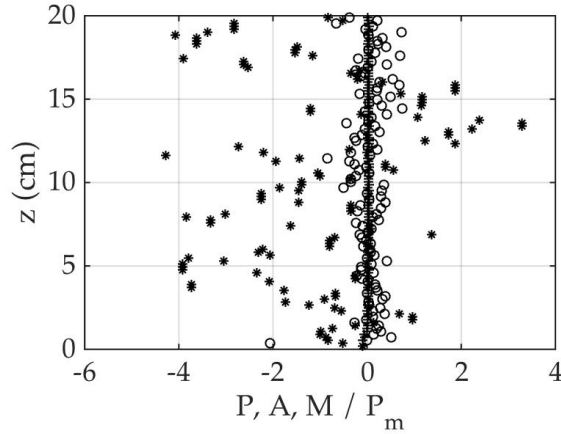


Figure 4.13: Production, advection, and viscous transport, normalized by median production, for  $T_{on} = 4s$ ,  $\Phi_{on} = 6.25\%$ .

#### 4.4 Advection

Due to low mean flow relative to the turbulence, advection of turbulent kinetic energy  $A = \langle U_j \rangle \frac{\partial k}{\partial x_j}$  is very weak relative to the other terms in the turbulent kinetic energy balance.  $A$  is weakly non-zero immediately above the bed, due to the bed-normal gradient in  $k$  at the no-slip boundary, and the downward flow, both of which contribute via the  $\langle W \rangle \frac{\partial k}{\partial z}$  component of the advection term. Even so, the ratio between mean advection and dissipation is 0.24% in the trial case for  $T_{on} = 4s$ ,  $\Phi_{on} = 6.25\%$ , for example, as shown in figure 4.13. Advection is an order-of-magnitude smaller than production as well, so we neglect its contribution to the turbulent kinetic energy balance.

#### 4.5 Viscous Transport

Due to the homogeneity of the flow,  $M = \nu \frac{\partial^2 k}{\partial x_j^2}$ , or viscous transport, is also negligibly small, despite noticeable gradients of turbulent kinetic energy,  $\frac{\partial k}{\partial z}$ . Viscous

transport is only approximately half as strong as advection, as shown in figure 4.13, and it is similarly neglected.

## 4.6 Pressure Diffusion

At present, we do not make *in situ* pressure measurements in the facility, nor do we have measurements with sufficient temporal resolution to allow for the direct computation of pressure gradients from PIV data using methods such as those shown by Dabiri et al. (2014). However, by considering the turbulent kinetic energy balance shown in figure 4.14 and computing pressure diffusion,  $Pr = \frac{1}{\rho_0} \frac{\partial \langle u_i p \rangle}{\partial x_i}$  as the residual, it is apparent that pressure potentially plays a significant role at the bed to balance non-zero dissipation, since all other terms approach zero at the bed. In particular, the bed-normal component  $p_z = -\frac{1}{\rho_0} \frac{\partial \overline{w' p'}}{\partial z}$  would likely be of greatest significance, and it is something that we will revisit in future experiments to evaluate its role in the energy balance.

## 4.7 Turbulence Statistics

Having completed analysis of many higher-order turbulence statistics, we can compute additional metrics of the flow such as Kolmogorov scales, Taylor scales, Reynolds numbers, and others. We compute the Kolmogorov time and length scales as  $\tau = (\frac{\nu}{\epsilon})^{\frac{1}{2}}$  and  $\eta \equiv (\frac{\nu^3}{\epsilon})^{\frac{1}{4}}$ , respectively, to represent the smallest scales of the turbulence. An intermediate length scale, the Taylor microscale, is then computed as  $\lambda = \sqrt{10} \eta^{\frac{2}{3}} \mathcal{L}^{\frac{1}{3}}$ . Resulting values are summarized in table 4.2 and table 4.3.

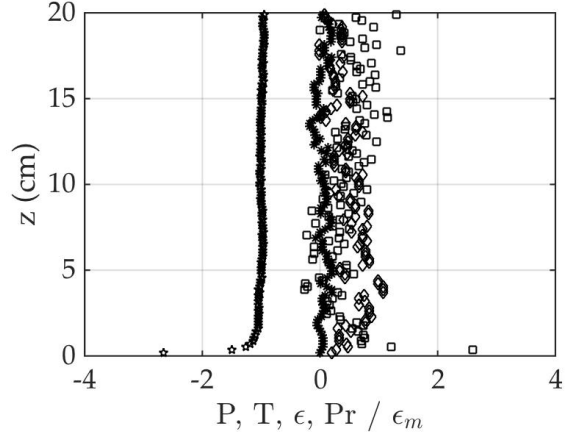


Figure 4.14: Dissipation (☆), Triple correlations (median-filtered for smoothing, ◇), Production (median-filtered for smoothing, \*), and estimated Pressure (□). Non-dimensionalized by  $\epsilon_m$  from direct method.  $T_{on} = 4s$ ,  $\Phi_{on} = 6.25\%$ ,  $8 \times 8$  RASJA.

$\Phi_{on} (\%)$	$T_{on} (s)$	$\tau (s)$	$\eta (cm)$	$\lambda (cm)$
6.25	4	0.035	0.019	0.42
6.25	6	0.032	0.018	0.42
6.25	8	0.029	0.017	0.45
7.7	4	0.036	0.019	0.43
7.7	6	0.031	0.018	0.41
7.7	8	0.028	0.017	0.41
9.1	4	0.032	0.018	0.41
9.1	6	0.029	0.017	0.42
9.1	8	0.028	0.017	0.40
10.5	4	0.031	0.018	0.40
10.5	6	0.029	0.017	0.41
10.5	8	0.032	0.018	0.45
12.5	4	0.030	0.017	0.40
12.5	6	0.028	0.017	0.41
12.5	8	0.027	0.016	0.42

Table 4.2: Kolmogorov and Taylor scales,  $8 \times 8$  RASJA.

$\Phi_{on}$ (%)	$T_{on}$ (s)	$\tau$ (s)	$\eta$ (cm)	$\lambda$ (cm)
3.1	0.8	0.025	0.016	0.33
3.1	1.0	0.022	0.015	0.33
3.1	1.2	0.019	0.014	0.30
3.1	1.4	0.018	0.014	0.30
3.1	1.6	0.017	0.013	0.29

Table 4.3: Kolmogorov and Taylor scales, 16 x 16 RASJA.

The Reynolds number based on the Taylor microscale,  $Re_\lambda = \left(\frac{2}{3}k\right) \sqrt{\frac{15}{\epsilon}}$ , provides a traditional metric of grid turbulence. Our values range from 244 to 378, consistent with results in Variano & Cowen (2008). We can also compute a grid Reynolds number,  $Re_G = 2\frac{\sqrt{\frac{2}{3}k}\mathcal{L}}{\nu}$ , for comparison to prior experiments in GST literature, and  $Re_L = Re^* = \frac{k^2}{\epsilon\nu}$  for comparison with moving bed experiments. The Peclet number, the ratio of advective transport to diffusive transport, is computed as  $Pe = \frac{\bar{U}\mathcal{L}}{\chi_t}$  where turbulent diffusivity  $\chi_t = \sqrt{k}\mathcal{L}$  and  $\bar{U}$  is the magnitude of mean longitudinal velocity. Values of  $Pe$  less than 0.1 confirm the highly diffusive-dominant nature of the facility in which the turbulence outweighs advective transport. Results of the aforementioned statistics are summarized in table 4.4 and table 4.5.

$\Phi_{on}$ (%)	$T_{on}$ (s)	$Re_\lambda$	$Re_G$	$Re_L = Re^*$	$\chi_t \left( \frac{cm^2}{s} \right)$	$Pe$
6.25	4	288	6308	12455	38.63	0.021
6.25	6	334	7799	16783	47.76	0.010
6.25	8	378	11385	21461	69.72	0.046
7.7	4	331	6793	16385	41.60	0.019
7.7	6	335	7608	16818	46.59	0.031
7.7	8	352	8962	18626	54.88	0.091
9.1	4	277	6150	11475	37.66	0.013
9.1	6	330	8398	16335	51.43	0.007
9.1	8	342	8290	17524	50.77	0.020
10.5	4	279	6224	11681	38.11	0.016
10.5	6	316	8119	14974	49.72	0.024
10.5	8	409	10336	25041	63.30	0.034
12.5	4	281	6690	11818	40.97	0.025
12.5	6	318	8369	15177	51.25	0.001
12.5	8	341	9976	17395	61.09	0.036

Table 4.4: Reynolds numbers and Peclet number, 8 x 8 RASJA.

$\Phi_{on}$ (%)	$T_{on}$ (s)	$Re_\lambda$	$Re_G$	$Re_L = Re^*$	$\chi_t \left( \frac{cm^2}{s} \right)$	$Pe$
3.1	0.8	197	4200	5807	25.72	0.055
3.1	1.0	218	5212	7155	31.92	0.035
3.1	1.2	230	5172	7907	31.67	0.018
3.1	1.4	249	5370	9335	32.89	0.002
3.1	1.6	262	6000	10329	36.74	0.025

Table 4.5: Reynolds numbers and Peclet number, 16 x 16 RASJA.

## CHAPTER 5

### BOUNDARY LAYER RESULTS - SOLID BOUNDARY

Given the analysis of our mean shear free boundary layer and exploration of methods of analysis presented in the preceding chapters, we now aim to compare the resulting profiles to existing literature on experimental and theoretical flows without mean bed shear. We first consider results over a solid flat plate, for which there is significant prior research. As the conceptual development of rapid distortion theory and prior experiments differs significantly from our experimental setup (*e.g.* we study a physically stationary boundary, whereas prior research considers temporally and spatially developing boundary layers over, at times, moving boundaries), we explore the similarities and differences observed, many of which are expected given the varied configurations.

#### 5.1 Fluctuating Velocities and Turbulent Kinetic Energy

The following are comparisons between our experimental results with the moving bed experiment of Thomas & Hancock (1977) and RDT of Hunt & Graham (1978) for both inviscid and viscous cases, which apply in different regions of the boundary layer. Viscosity dominates the flow within approximately  $\frac{\mathcal{L}}{10}$  of the boundary, causing velocity to approach zero due to the no-slip boundary, though a true viscous sublayer is difficult to identify within this region. Outside of this region and within approximately one integral length scale of the wall, where intercomponent energy transfer is strong due to the presence of the boundary, inviscid theory can be applied as the kinematic, rather than no-slip, boundary condition, dominates.

The turbulence generating mechanisms and imposed boundary conditions are very different between our experiments and the moving bed studies, so we do not expect identical results. In our experimental facility, the RASJA continuously injects momentum into the flow and acts as a constant source of stationary turbulence. At present, we do not consider the development of turbulence from the inception of jet activity, but instead begin measurements once the turbulence is statistically stationary. The solid glass boundary does not move and acts as a sink of energy due to the no-slip boundary. By contrast, the moving bed experiments and theory have a source of energy above the flow, as the grid-generated turbulence advects over the boundary, and at the moving bed itself, which can dampen or increase the velocity of nearby fluid that is moving faster or slower, respectively, than the mean flow velocity.

Furthermore, the results presented in Thomas & Hancock (1977) and Hunt & Graham (1978) are time and space dependent, providing an additional layer of complexity. As shown in figure 1.1, the boundary layer grows with distance along the bed as the flow develops downstream of the turbulence-generating grid. The boundary layer does not evolve in a self-similar manner, with the source region and viscous regions of Hunt & Graham (1978) growing at different rates, and so it becomes critical, yet arbitrary, to select the location downstream in the moving-bed experiments to provide adequate comparison to the stationary boundary layer generated by the RASJA.

We show two sets of results in the moving bed experiments:  $x/M = 13$  and  $x/M = 25$ , where the ratio of downstream distance  $x$  to grid-spacing  $M$  gives a measure of the relative development of the turbulent boundary layer as it decays along the moving bed. We do not include the moving bed data of Uzkan &

Reynolds (1967) due to the low magnitude of the integral length scale reported that consequently alters the scaling significantly so as not to produce comparable results, as is argued in Thomas & Hancock (1977).

### 5.1.1 8 x 8 RASJA

Figure 5.1 shows the inviscid RDT profiles for turbulent velocities. We include three experimental trials, varying  $T_{on}$  from 4 s to 8 s. Our three bed-normal RMS velocity trials collapse and scale well with the moving bed experiments and theory. However, the tangential RMS velocity proves more complicated. Away from the wall ( $z/L_m > 0.1$ ), the inviscid theory qualitatively serves well. The moving bed experiments are limited by their ability to properly scale with downstream turbulence development, as is evident by the agreement observed between the  $x/M = 13$  moving bed data, whereas at  $x/M = 25$ ,  $u'/u'_m$  shows a greater departure from unity away from the wall. Our experimental data better agree with the more developed boundary layer in the  $x/M = 25$  case, which asymptotes to unity nearly 1.5 integral length scales above the wall.

Close to the wall ( $z/L_m < 0.1$ ), the viscous model shown in figure 5.2 better captures the tangential velocity fluctuations that decay to zero at the bed, as is expected as viscous processes are dominant at the wall. The moving bed experimental data do not follow this trend, likely due to our inability to measure velocities within the viscous boundary layer (Thomas & Hancock 1977).

The inviscid theory does not fully capture the measured flow dynamics when considering  $k$  near the wall, as shown in figure 5.3. Due to the no-slip boundary,  $k$  approaches zero at  $z = 0$  whereas inviscid RDT suggests  $\frac{k}{k_m} = 1$  at

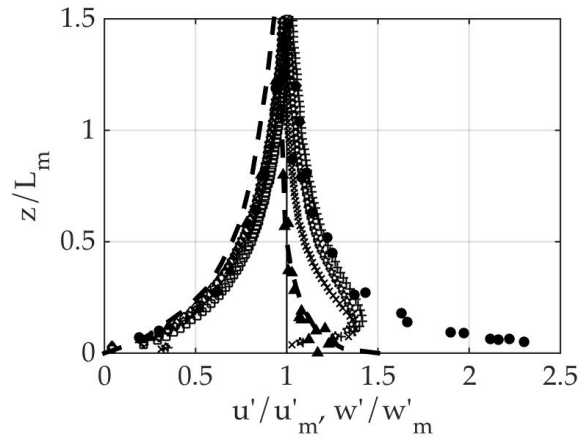


Figure 5.1: Comparison of  $u'/u'_m, w'/w'_m$  with Hunt & Graham (1978) inviscid theory and Thomas & Hancock (1977) experimental moving bed data at  $x/M = 25$  ( $\bullet$ ),  $x/M = 13$  ( $\blacktriangle$ ). Present cases are for  $\Phi_{on} = 6.25\%$  and  $T_{on} = 4$  s ( $\star, \diamond$ ), 6 s ( $+, \ast$ ), 8 s ( $\times, \square$ )

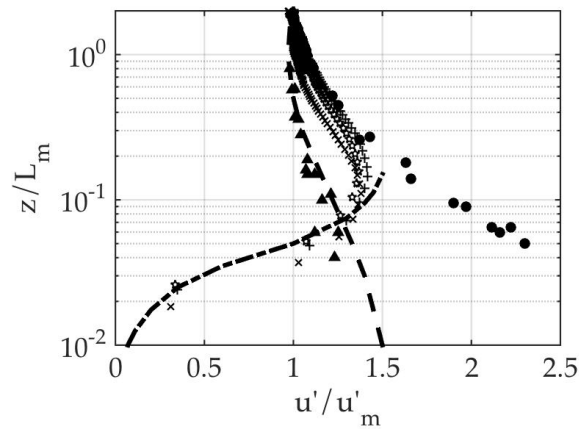


Figure 5.2: Viscous (—) and source (---) regions of  $u'/u'_m$ . See previous figure for legend.

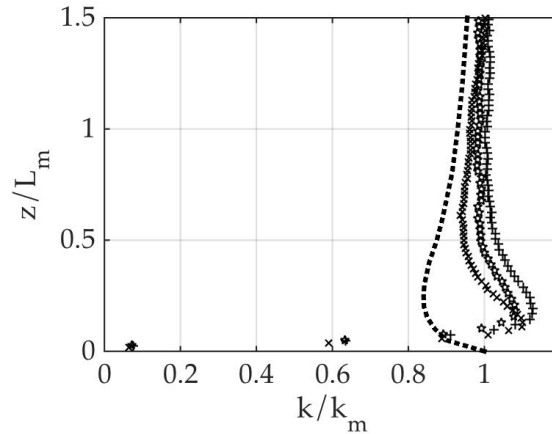


Figure 5.3: Comparison of  $k/k_m$  with Hunt & Graham (1978) inviscid theory. See figure 5.1 for legend.

the moving bed, though this is not a realistic expectation of our flow. Furthermore, rather than  $k$  decaying gradually with increasing depth, we experimentally observe  $\frac{k}{k_m} > 1$  near the bed with a peak near  $z/\mathcal{L}_m = 0.1$ . This increase in  $k$  can be attributed to the bed-parallel turbulent motions that arise from the significant intercomponent energy transfers generated via turbulent splats (Perot & Moin 1995a) and likely pressure gradient contributions due to the rigid wall.

### 5.1.2 16 x 16 RASJA

We observe similar collapse of the five curves with varying  $T_{on}$  from the 16 x 16 RASJA trials. Though the magnitude of the normalized  $u'$  curves shown in figure 5.4 is slightly lower in the experiments with the 16 x 16 RASJA than with the 8 x 8 RASJA, as shown in figure 5.1, the profiles show good qualitative agreement. The shape of the viscous decay toward the bed shown in figure 5.5 varies slightly, though it is still consistent with RDT and the less-developed  $x/M = 13$  trials of Thomas & Hancock (1977).

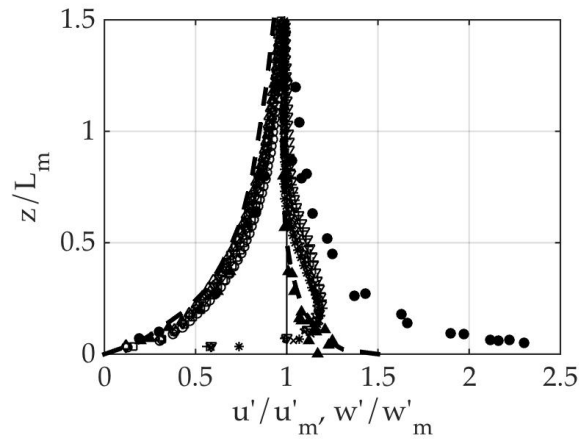


Figure 5.4: Comparison of  $u'/u'_m$ ,  $w'/w'_m$  with Hunt & Graham (1978) inviscid theory and Thomas & Hancock (1977) experimental moving bed data at  $x/M = 25$  ( $\bullet$ ),  $x/M = 13$  ( $\blacktriangle$ ). Present cases are for  $\Phi_{on} = 3.1\%$  and  $T_{on} = 0.8$  s ( $*$ ,  $\square$ ),  $1.0$  s ( $\times$ ,  $\circ$ ),  $1.2$  s ( $\star$ ,  $\diamond$ ),  $1.4$  s ( $\nabla$ ,  $\triangle$ ),  $1.6$  s ( $+$ ,  $\star$ ).  $16 \times 16$  RASJA.

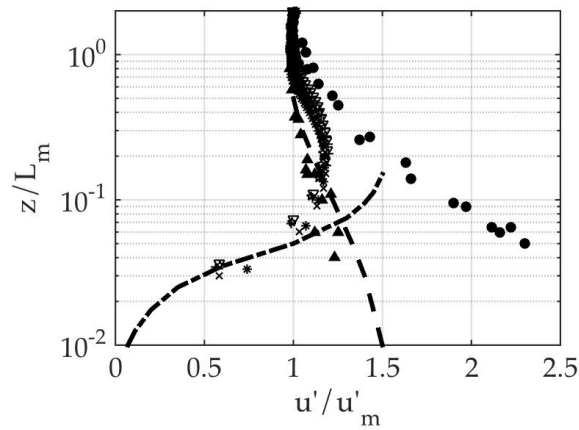


Figure 5.5: Viscous (–) and source (–·) regions of  $u'/u'_m$ . See previous figure for legend.

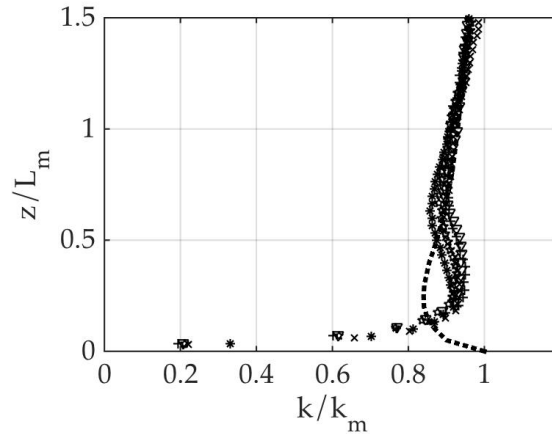


Figure 5.6: Comparison of  $k/k_m$  with Hunt & Graham (1978) inviscid theory. See figure 5.4 for legend.

The resulting turbulent kinetic energy profiles from the  $16 \times 16$  RASJA show further disagreement with the inviscid RDT profiles shown in figure 5.6, as expected. Due to the decay in  $k$  with  $z$  referenced previously in figure 3.5, the selection of  $k_m$  in the mixed region is less straightforward and the resulting collapse of the curves does not reach unity within  $1.5\mathcal{L}$  of the bed.

## 5.2 Integral Length Scale

Further evidence of the physical nature of turbulent splats is shown when we reconsider the integral length scale. A scaling of figure 3.8 better highlights the stretching of horizontal motions observed within one integral length scale of the bed. Figure 5.7 shows that whereas Hunt & Graham (1978) find a 5% increase in  $\mathcal{L}_{11}$  near  $\frac{z}{\mathcal{L}_{11}} = 1$ , and Thomas & Hancock (1977) find nearly a 10% increase near  $\frac{z}{\mathcal{L}_{11}} = 0.5$ , our data show 25-40% increases in the length scale of motions parallel to the bed in the  $8 \times 8$  RASJA. In the  $16 \times 16$  RASJA, shown in figure 5.8, there is a 40-60% increase in  $\frac{\mathcal{L}_{11}}{\mathcal{L}_{11,m}}$ . At  $z = 0$ , RDT suggests  $\frac{\mathcal{L}_{11}}{\mathcal{L}_{11,m}} = 2/3$ , which is a

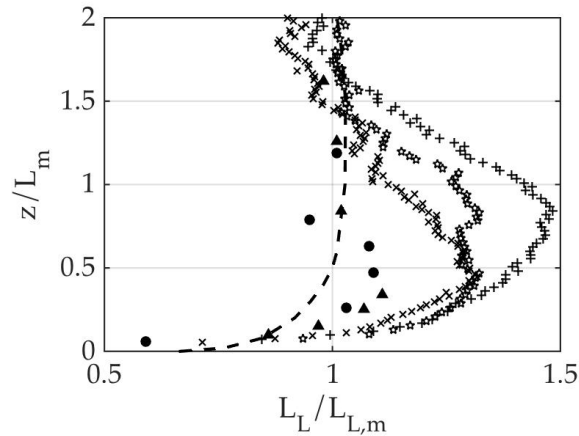


Figure 5.7: Longitudinal integral length scale comparison with Hunt & Graham (1978) and Thomas & Hancock (1977) Present cases are for  $\Phi_{on} = 6.25\%$  and  $T_{on} = 4$  s ( $\star$ ), 6 s (+), 8 s (x). 8 x 8 RASJA.

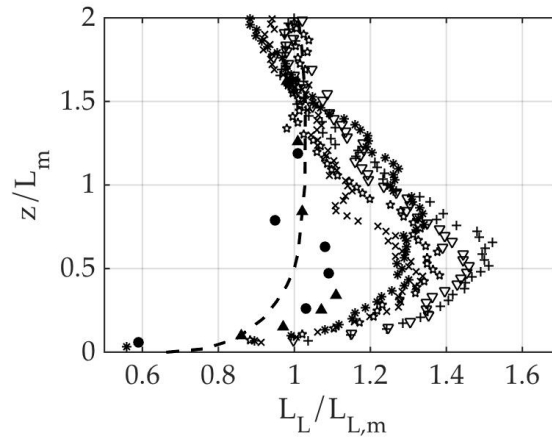


Figure 5.8: Longitudinal integral length scale comparison with Hunt & Graham (1978) and Thomas & Hancock (1977) Present cases are for  $\Phi_{on} = 3.1\%$  and  $T_{on} = 0.8$  s (\*), 1.0 s (x), 1.2 s ( $\star$ ), 1.4 s ( $\nabla$ ), 1.6 s (+). 16 x 16 RASJA.

reasonable estimate if our data were extrapolated further towards the bed. The transverse integral length scale profiles in figure 5.9 and figure 5.10 align well and approach zero at the bed, as is consistent with theory. Again, better collapse is observed in the 8 x 8 RASJA trials as compared to the 16 x 16 RASJA trials.

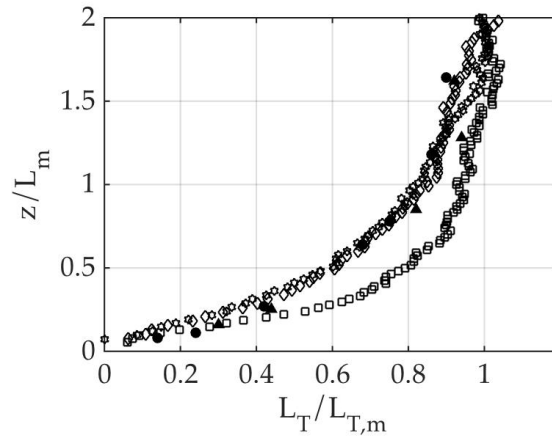


Figure 5.9: Transverse integral length scale comparison with Thomas & Hancock (1977). 8 x 8 RASJA. See figure 5.7 for legend.

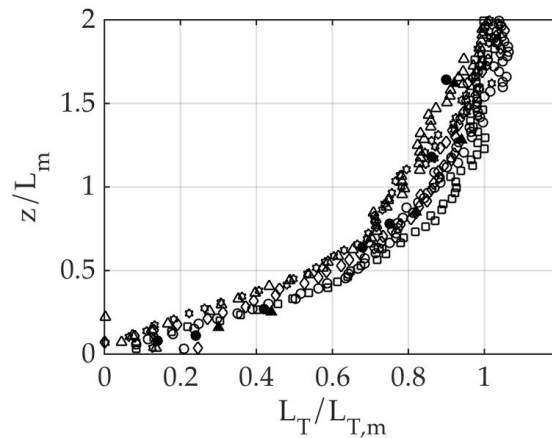


Figure 5.10: Transverse integral length scale comparison with Thomas & Hancock (1977). 16 x 16 RASJA. See figure 5.8 for legend.

### 5.3 Dissipation Comparisons with RDT

Teixeira & Belcher (2000) extended the RDT work of Hunt & Graham (1978) to account for dissipation. With strict assumptions of isotropy, they only consider diagonal components of Reynolds stress and dissipation terms. Thus, component-based dissipation simplifies to  $\varepsilon_{11} = 2\nu \left[ 2 \left( \frac{\partial u}{\partial x} \right)^2 + \left( \frac{\partial u}{\partial z} \right)^2 \right]$  and  $\varepsilon_{33} =$

$2\nu \left[ 2 \overline{\left( \frac{\partial w}{\partial x} \right)^2} + \overline{\left( \frac{\partial w}{\partial z} \right)^2} \right]$ . We assume radial symmetry so that  $\varepsilon_{22} = \varepsilon_{11}$ . We draw comparisons between these contributions in figures 5.11 and 5.12. It is important to note that our experiments are performed at much greater Reynolds numbers than these simulations. Using  $Re^* = \frac{k^2}{\nu \varepsilon}$ , we find experimental values ranging from 5,800 to 25,000, whereas Teixeira & Belcher (2000) and Perot & Moin (1995b) have values of  $Re^*$  of 134 in the cases considered.

As both the theoretical work of Teixeira & Belcher (2000) and DNS studies of Perot & Moin (1995b) address temporally developing turbulent boundary layers, we explore how our stationary data compares with their evolving profiles. At the initial insertion of the wall in RDT, our data and the DNS data show distinct disagreements at the bed for both the  $\frac{\varepsilon_{11}}{\varepsilon_{11,m}}$  and  $\frac{\varepsilon_{33}}{\varepsilon_{33,m}}$  cases.

At later times, the no-slip boundary develops and  $\frac{\varepsilon_{33}}{\varepsilon_{33,m}}$  approaches zero; the intercomponent energy transfer becomes more evident as  $\frac{\varepsilon_{11}}{\varepsilon_{11,m}}$  increases at the bed. The tangential dissipation component shows excellent agreement between our experimental data and the DNS data at  $\frac{\sqrt{kt}}{\mathcal{L}^*} = 2.0$ , where the integral length scale  $\mathcal{L}^* = \frac{k^{1.5}}{\varepsilon}$ , and with RDT at  $\frac{\sqrt{kt}}{\mathcal{L}^*} = 0.10$ . In the bed-normal component, our experimental  $\varepsilon_{33}$  approaches the mixed value more rapidly in the  $8 \times 8$  RASJA trial than the DNS or RDT at  $\frac{\sqrt{kt}}{\mathcal{L}^*} = 0.10$ ; however,  $\frac{\varepsilon_{33}}{\varepsilon_{33,m}}$  does not reach unity until  $\frac{z}{\mathcal{L}^*} > 1.5$ .

Whereas the total dissipation profiles in the trials conducted with the  $8 \times 8$  RASJA show values relatively independent of  $z$ , as shown previously in figure 4.5, the experiments in the  $16 \times 16$  RASJA facility show decaying dissipation away from the source, as we see in figure 5.13. Thus, the normalization presented in figures 5.11 and 5.12 does not converge to unity at  $\frac{z}{\mathcal{L}^*} = 0.5$  as suggested by Perot & Moin (1995b).

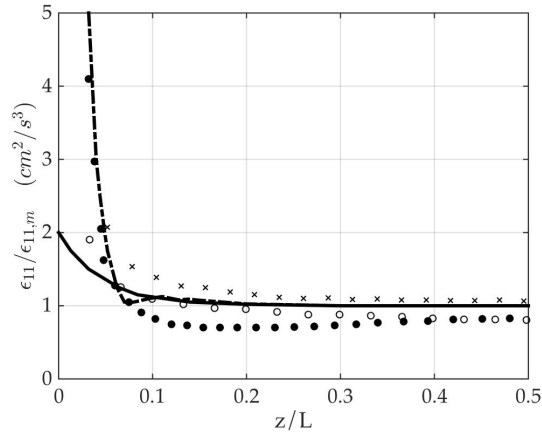


Figure 5.11:  $\varepsilon_{11}$  comparison to Teixeira & Belcher (2000) (solid line -  $\frac{\sqrt{kt}}{\mathcal{L}^*} = 0$ , viscous; dash-dot -  $\frac{\sqrt{kt}}{\mathcal{L}^*} = 0.10$ ), Perot & Moin (1995b) (dots -  $\frac{\sqrt{kt}}{\mathcal{L}^*} = 2.0$ ,  $Re^*=134$ ) (x -  $8 \times 8$ ,  $\circ$  -  $16 \times 16$ ).

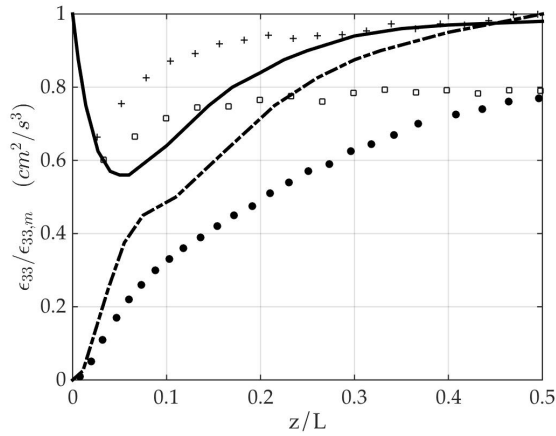


Figure 5.12:  $\varepsilon_{33}$  comparison to Teixeira & Belcher (2000) (solid line -  $\frac{\sqrt{kt}}{\mathcal{L}^*} = 0$ ; dash-dot -  $\frac{\sqrt{kt}}{\mathcal{L}^*} = 0.10$ ), Perot & Moin (1995b) (dots -  $\frac{\sqrt{kt}}{\mathcal{L}^*} = 2.0$ ,  $Re^*=134$ ) (+ -  $8 \times 8$ ,  $\square$  -  $16 \times 16$ ).

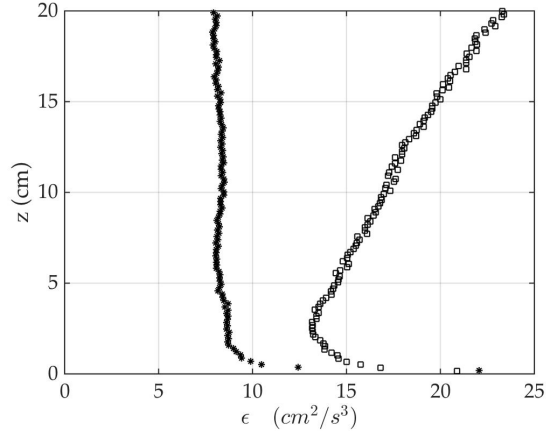


Figure 5.13: Comparison of total dissipation profiles between 8 x 8 RASJA (\*) and 16 x 16 RASJA (□).

Total dissipation,  $\varepsilon_{TB} = \frac{1}{2} (\varepsilon_{11} + \varepsilon_{22} + \varepsilon_{33})$ , expands to

$$\varepsilon_{TB} = \nu \left[ 4 \overline{\left( \frac{\partial \mathbf{u}}{\partial x} \right)^2} + 2 \overline{\left( \frac{\partial \mathbf{u}}{\partial z} \right)^2} + 2 \overline{\left( \frac{\partial \mathbf{w}}{\partial x} \right)^2} + \overline{\left( \frac{\partial \mathbf{w}}{\partial z} \right)^2} \right]$$

by applying radial symmetry to the Teixeira & Belcher (2000) formulation. This equation describes pseudo-dissipation, and it shows several obvious differences between our direct method of computing actual dissipation, which do not assume strict isotropy, but only radial symmetry. This theoretical method underestimates our results by approximately 44%, due primarily to the altered coefficients of the diagonal terms of the stress tensor.

By contrast, Teixeira & Da Silva (2012) compute the full dissipation rate as

$$\varepsilon_{TDS} = 2\nu \left[ 4 \overline{\left( \frac{\partial \mathbf{u}}{\partial x} \right)^2} + \overline{\left( \frac{\partial \mathbf{u}}{\partial z} \right)^2} + \overline{\left( \frac{\partial \mathbf{w}}{\partial x} \right)^2} + \overline{\left( \frac{\partial \mathbf{w}}{\partial z} \right)^2} + 2 \overline{\left( \frac{\partial \mathbf{u}}{\partial z} \frac{\partial \mathbf{w}}{\partial x} \right)} \right]$$

which improves agreement with our direct dissipation calculations to account for 87% of the total dissipation. Furthermore, Teixeira & Da Silva (2012) consider the increase in dissipation at the bed, finding a peak at  $\varepsilon(z=0) = \frac{17}{15} \varepsilon_m$ . By applying our direct method formulation and the Teixeira & Da Silva (2012)

formulation, we find significantly larger ratios of  $\varepsilon_{z=0}/\varepsilon_m$  ranging from 1.5 to 3.6 across the experimental cases considered.

## CHAPTER 6

### SEDIMENT DYNAMICS

One of the main objectives of this research is to understand the role of bed stress and the ability to transport sediment in turbulent flows where there is negligible mean shear. In the previous chapters, we saw strong intercomponent energy transfer in the boundary layer profiles, with strong bed-parallel motions that could contribute to instantaneous viscous shear events. Additionally, we found that pressure gradients may be of particular importance in turbulent flows with negligible mean shear, and those gradients could play a role in bed mobility.

In this chapter, we explore a new method for characterizing shear stress in a mean shear free turbulent flow. We also describe our experimental observations of sediment transport, whether via small-scale events such as rolling or creeping along the fluid-sediment interface, or larger-scale suspension events that can lead to periods of entrainment. An unexpected outcome from the experiments with turbulence above a sand bed was the formation of ripples. This was a surprising observation, as ripples have not previously been linked to turbulence absent mean or oscillatory flows, and in this chapter we present our findings on the relationship between the integral length scale of the turbulence and ripple development.

## 6.1 Bed Stress Analysis

### 6.1.1 Viscous vs. Reynolds Stresses

Characterizing the bed stress is non-trivial in a flow with negligible mean shear.

Classic viscous shear stress

$$\tau_v = \mu \frac{d\bar{U}}{dz}$$

does not accurately represent the bed shear in our fundamental study, as  $\langle U \rangle$  and any spatial gradient thereof is nearly zero when averaged over time in this stationary flow. Although there are strong instantaneous local shear events acting upon the boundary, we are unable to capture their magnitude immediately at the boundary through our PIV measurements. We look to using Reynolds stress

$$\tau_{Re} = \rho \langle u_i u_j \rangle$$

as a surrogate for viscous shear, as the magnitude of  $\tau_{Re}$  at the edge of a shear-driven boundary layer is equivalent to  $\tau_v$  at  $z = 0$  (Pope 2000). We again find that this results in a negligible contribution to stress due to homogeneity and radial symmetry when averaged over time.

### 6.1.2 Short Time Scale Analysis

As we know that both viscous and Reynolds stresses must be significant over short time scales, due to the sediment transport observed, we instead look for a way to characterize events over short time periods. We consider production,  $P = -\langle u_i u_j \rangle \frac{\partial \langle U_i \rangle}{\partial x_j}$ , which has contributions from both Reynolds stress compo-

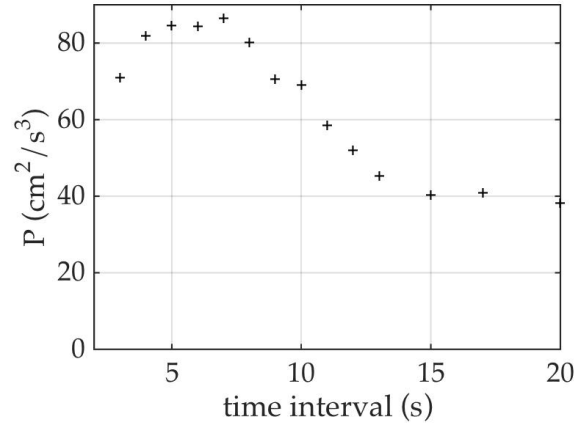


Figure 6.1: Maximum magnitude of production obtained with varying time intervals.

nents  $\langle u_i u_j \rangle$  and mean velocity gradients  $\frac{\partial \langle U_i \rangle}{\partial x_j}$ . When averaged over 30 minutes,  $P$  is nearly zero, as discussed previously. Over short time scales, however, on the order of seconds or tens of seconds, we observe considerably higher magnitudes of  $P$ .

To achieve this, we break the temporal record of PIV data into increments ranging from 3 seconds to 20 seconds.  $P$  is computed based on the mean flow and velocity fluctuations within that period only. Thus, too small of a record results in negligible fluctuations, and too long of a record results in negligible mean velocities. We find that maximum values of  $P$  are attainable for a period of 7 s for the trial in which  $\Phi_{on} = 3.125\%$  and  $T_{on} = 0.8$  s with the 16 x 16 RASJA, for example, as shown in figure 6.1.

We again compute  $\tau_v$  and  $\tau_{Re}$  instead using 7 s time periods. We first compute  $\frac{d\langle U \rangle}{dz}$  by using first-order finite differences; a histogram of all of the 7 s averages is shown in figure 6.2. Using finite differences, we are unable to see true viscous shear as the nearest that we can measure is 2.7 mm above the bed, with resulting values of  $\tau_v < 0.1$  mPa.

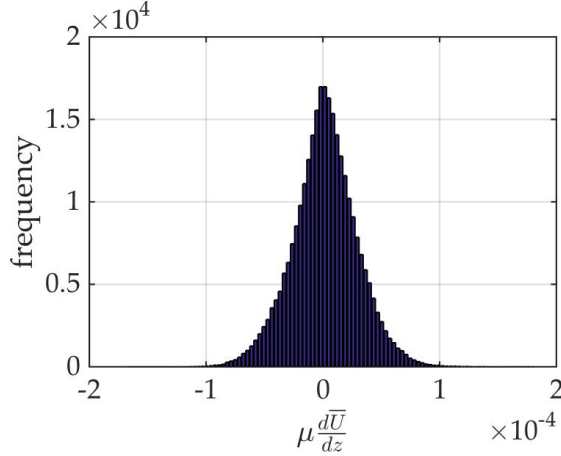


Figure 6.2: Histogram of  $\tau_v$  (at 7 s intervals) measured at  $z = 3$  mm.  $\Phi_{on} = 6.25\%$ ,  $T_{on} = 4$  s,  $8 \times 8$  RASJA.

Instead, we calculate  $\rho \langle u_i u_j \rangle$  in 7 s increments at the edge of the boundary layer. In a shear-driven flow, there is a peak in  $\rho \overline{uw}$  at the end of the viscous boundary layer from which we can approximate the magnitude of  $\tau_v$ , then  $\rho \langle u_i u_j \rangle$  decreases with increasing height above the bed. In our experiments, the magnitude of  $\rho \langle uw \rangle$  does not peak, but instead continually increases with height, as shown in figure 6.3. We instead choose the edge of the boundary layer as the height at which  $k$  peaks at the transition from the kinematic region to the source region, approximately 1 cm above the bed as shown in figure 3.4, for example.

By constructing a histogram of the Reynolds stresses computed from 7 s increments, as shown in figure 6.4, we can better understand the magnitude of instantaneous stress events and their associated friction velocities,

$$u_* = \sqrt{\frac{|\tau_{Re}|}{\rho}}$$

which we calculate from the magnitude of Reynolds stresses presented in the histogram. As expected, the histogram of Reynolds stresses is centered about

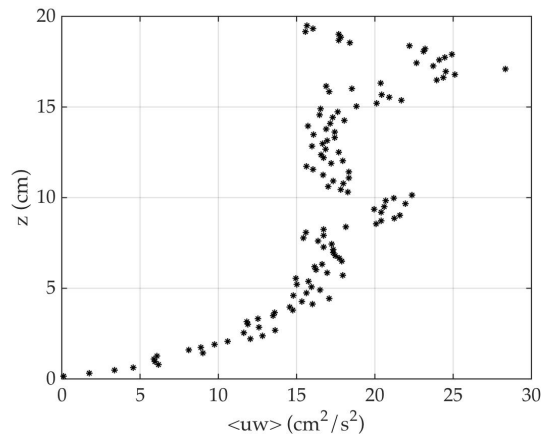


Figure 6.3: Magnitude of maximum  $\overline{uw}$  computed over 7 second increments.  $\Phi_{on} = 6.25\%$ ,  $T_{on} = 4$  s,  $8 \times 8$  RASJA.

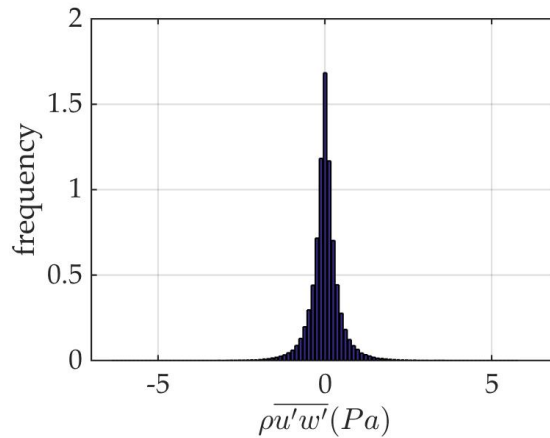


Figure 6.4: Histogram of  $\tau_{Re}$  (at 7 s intervals) measured at  $z = 1$  cm.  $\Phi_{on} = 6.25\%$ ,  $T_{on} = 4$  s,  $8 \times 8$  RASJA.

zero, which tells us little about the high magnitude stress events that result in intermittent sediment motion and pick-up. Similarly, carrying out the computation using the median Reynolds stress would produce a negligible friction velocity. Instead, we look at the tails of the histogram to gain an understanding of the likelihood of an extreme instantaneous local event to mobilize sediment at the bed.

Percentiles	$\tau_{Re}$ (Pa)	$u_*$ (cm/s)
0.5	-1.62	4.02
2.5	-0.96	3.09
5	-0.70	2.64
10	-0.46	2.15
25	-0.18	1.35
50	0.00	0.22
75	0.19	1.39
90	0.47	2.17
95	0.72	2.69
97.5	1.00	3.16
99.5	1.74	4.17

Table 6.1: Percentiles of Reynolds stress distribution and corresponding friction velocities.  $\Phi_{on} = 6.25\%$ ,  $T_{on} = 4$  s,  $8 \times 8$  RASJA.

Specifically, it is useful to consider what occurs at various percentiles of the Reynolds stress distribution. We compute the percentiles of the Reynolds stress distribution and convert them into friction velocities, as shown in table 6.1. While this distribution is approximately symmetric, it is not precisely centered upon zero with symmetric tails. In order to assign specific values that roughly correspond to the value in a perfectly symmetric distribution in table 6.2, we compute the average of the matching percentiles on either side of the median. For example, to identify the values of friction velocity exceeded by the outermost 1% of the data, we average the friction velocities found for the 0.5 and 99.5 percentiles.

Clearly, the friction velocities found in the tails of the Reynolds stress histogram over short time periods are significant in comparison to those centered about the median. From the Shields curve, shown previously in figure 1.2, it is expected that a critical  $u_*$  of 1.3 cm/s corresponds to incipient sediment motion for the sand used in our experiments. Indeed, our data shows that this critical stress is exceeded in the outermost ranges of the histograms at the 25th and 75th

% of data in tails	$\Phi_{on} = 6.25\%$ $T_{on} = 4$ s 8 x 8 RASJA	$\Phi_{on} = 3.125\%$ $T_{on} = 0.8$ s 16 x 16 RASJA	$\Phi_{on} = 3.125\%$ $T_{on} = 1.6$ s 16 x 16 RASJA
1	4.10	4.40	6.15
5	3.13	3.36	4.68
10	2.66	2.87	4.01
20	2.16	2.31	3.25
50	1.37	1.44	2.06

Table 6.2: Lower bounds of tails of friction velocity  $u_*$  (cm/s) distribution for three RASJA settings.

percentiles in the case for which  $\Phi_{on} = 6.25\%$  and  $T_{on} = 4$  s with the 8 x 8 RASJA, for example. The likelihood to exceed this stress in tests shown with the 16 x 16 RASJA is even higher, consistent with the increased observations of sediment transport to be discussed in the upcoming sections.

## 6.2 Mechanisms of Sediment Suspension

Two distinct phenomena are observed that result in sediment suspension from the bed in which sand grains are picked up and briefly entrained in the fluid flow above the bed. The first is vortical in nature, much like a dust devil (Sinclair 1968) or whirlwind that spins about a vertical axis and travels laterally across the bed. These structures are typically attached to the bed and are able to entrain additional sediment as they travel, due to the low pressure in the core of the vortex that encourages sediment pick-up. In experiments with the 8 x 8 RASJA, bed-attached vortices reached approximately 1 cm to 5 cm above the bed and were less than 2 cm in diameter according to visual estimates. In experiments with the 16 x 16 RASJA, these structures could grow significantly larger and entrain sand grains up to approximately 10 cm above the bed with diameters

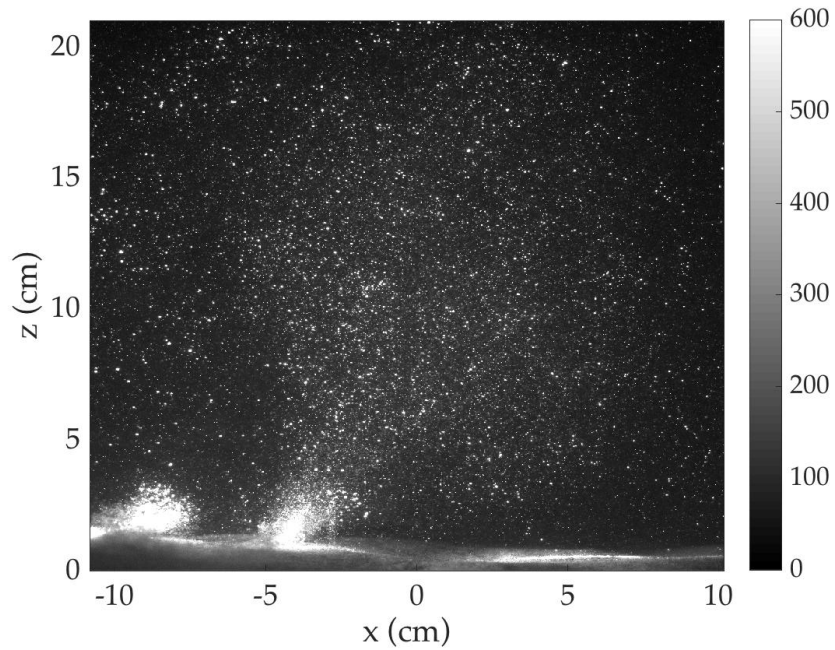


Figure 6.5: Image of sediment suspension generated by bed-attached sand vortices.  $\Phi_{on} = 3.1\%$ ,  $T_{on} = 1.6$  s,  $16 \times 16$  RASJA.

up to approximately 5 cm. These large vortices appeared to be more short-lived than their smaller counterparts.

From visual observations, vortices appear more frequently over flat terrain rather than a rippled bed, though they can form anywhere. There appear to be no lasting effect on large scale bed morphology as a result of vortices; small trails that form as sediment is entrained into the vortex or is deposited after falling out of suspension are quickly erased by other turbulent flow structures near the bed. Figure 6.5 shows a sample image in which two bed-attached vortices were present in the FOV. The high concentration of sand near the bed shows the cores of the vortices. The vortex on the left is contained within the bottom 1.5 cm above the bed, whereas the vortex on the right appears connected to a larger cloud of suspended sediment entrained above.

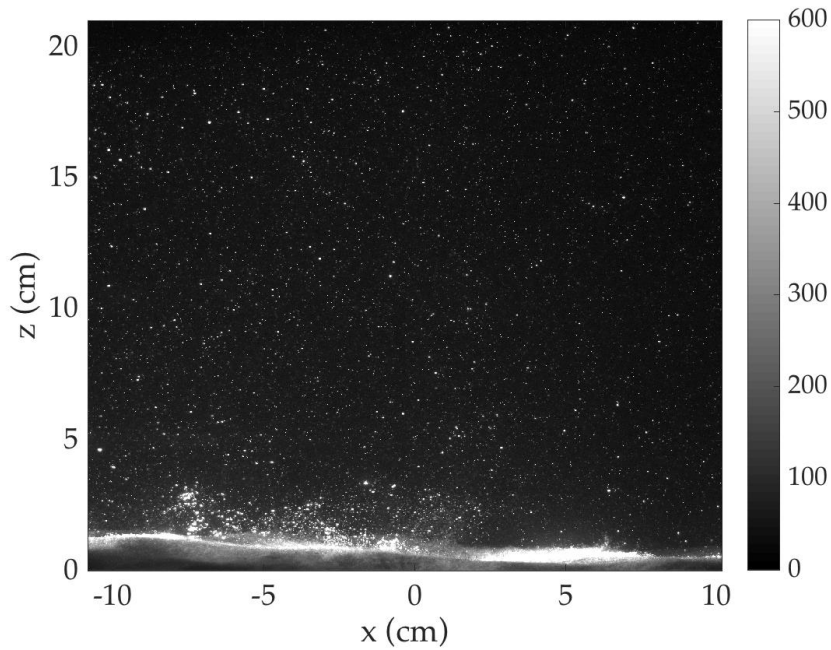


Figure 6.6: Image of sediment transport in a turbulent splat.  $\Phi_{on} = 3.1\%$ ,  $T_{on} = 1.6$  s, 16 x 16 RASJA.

The second suspension phenomena is generated via turbulent splats, or the interaction of multiple adjacent splats into antisplats (Perot & Moin, 1995a). Re-suspension events from splats occurred when flows approaching the bed suddenly feel the bed and are turned and travel along the bed from the central location of the splat. These were observed as clusters of sediment grains being entrained in the flow only a few millimeters above the bed and radiating outwards, an example of which is shown in figure 6.6.

When multiple splats interacted, in that various strong instantaneous bed-parallel flows approached one another, sediment was ejected vertically upward from the bed. Vortices occasionally emerged as a result of anti-splats, though from the observations made, it is not clear that anti-splats are essential to the formation of vortical structures of sediment suspension. Resuspension from

splats and anti-splats occurred on both flat and rippled sediment boundaries. When sand ripples were present, the occurrence of splats appeared to cause the deepening and migration of ripple troughs; likewise, anti-splats were often found to contribute to the formation and migration of ripple crests.

Sediment suspension was much more prevalent in tests with the 16 x 16 RASJA than with the 8 x 8 RASJA. Suspension events were larger in size, entrained relatively greater quantities of sediment, and kept sediment in suspension for longer durations of time. Figure 6.7 shows a series of images collected for the same suspension event. The dispersion of the suspended cloud is apparent as time progresses. Additionally, there is stretching and reforming of the cloud that is evident as the structure grows and divides into multiple patches of suspended sediment.

### **6.3 Ripple Dynamics**

In addition to sediment motion generated via vortices and splats, we observe ripples that develop across the bed. This was an unexpected result in our experiments, as structures such as ripples and dunes are typically generated along mean currents or oscillatory flows. We seek a relationship between the ripples and turbulence, and we describe the resulting sediment transport associated with the bed morphology in this unique flow.

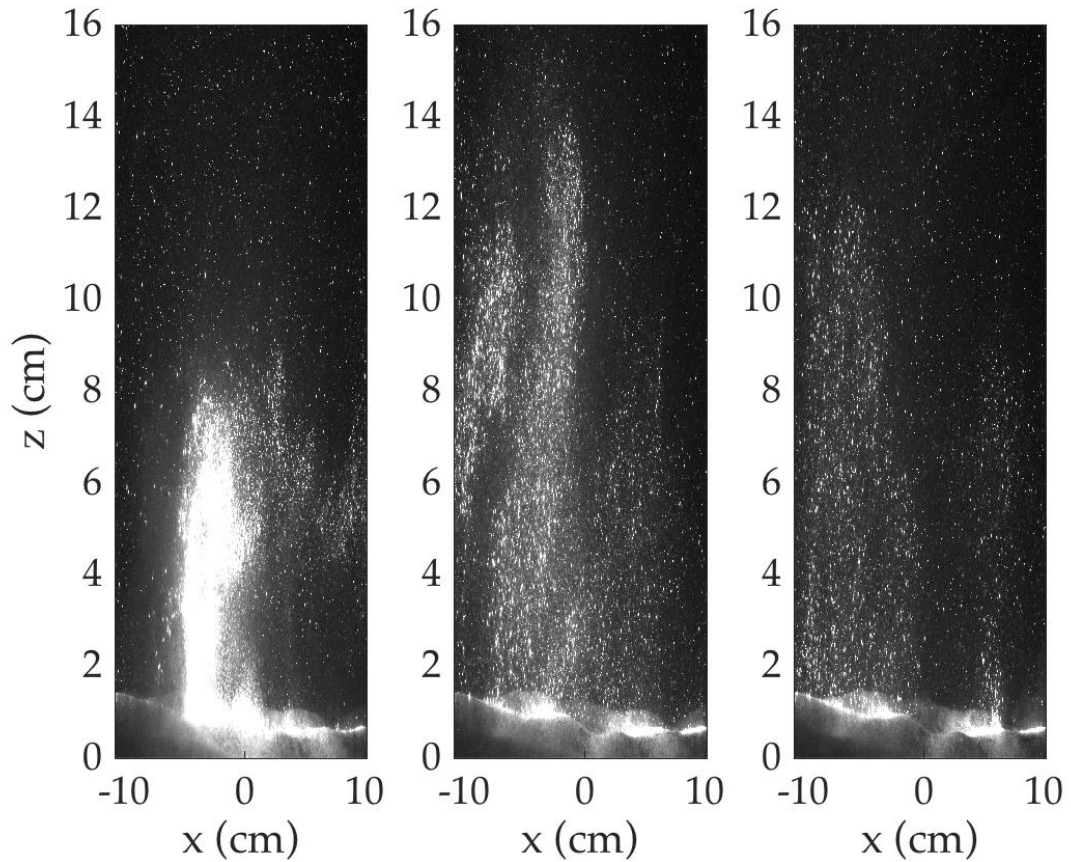


Figure 6.7: Evolution of a cloud of suspended sediment. Each panel, from left to right, shows the progression of the sediment cloud at 1 s intervals.  $\Phi_{on} = 3.1\%$ ,  $T_{on} = 1.6$  s, 16 x 16 RASJA.

### 6.3.1 Development of Ripples

Starting from an initially flat bed, small dimples quickly began to emerge in the bed, even in the absence of visible sediment suspension events. Instead, transport on the order of millimeters via rolling or creeping contributed to much of the bed morphology. In time, depending on the strength of the turbulence, it was apparent that the ripples were organized in patterns orthogonal to the tank walls. Eventually, the entire bed developed into a grid of orthogonal ripples, which continued to migrate throughout the tests, though they appeared to reach

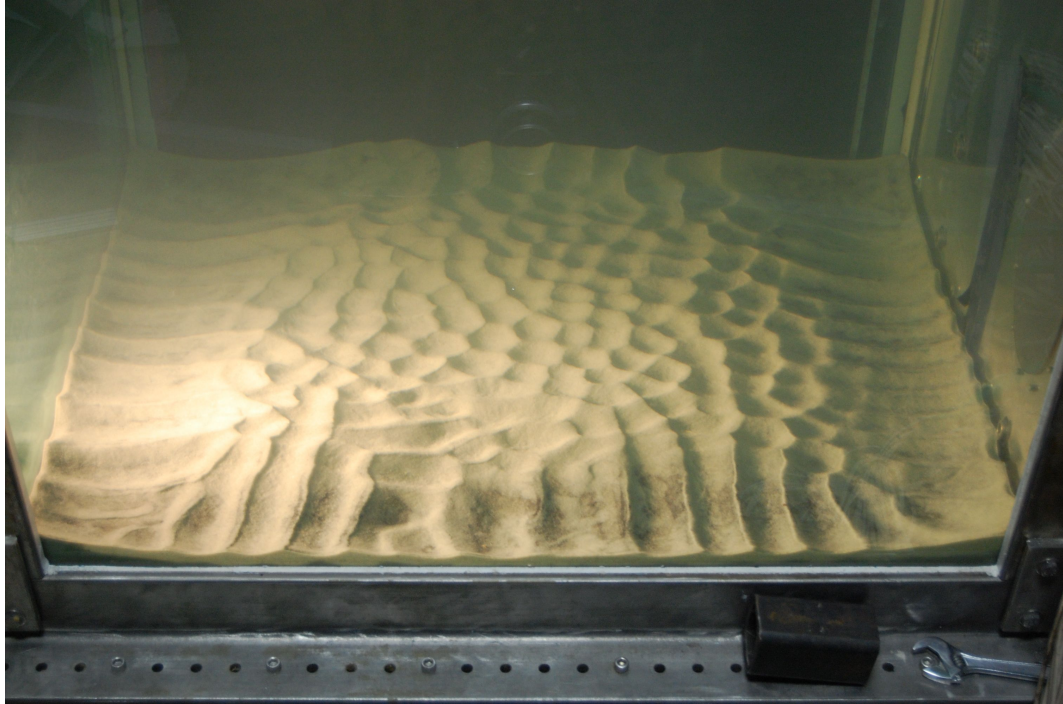


Figure 6.8: Resulting sand ripples after 12 hours.  $\Phi_{on} = 6.25\%$ ,  $T_{on} = 4$  s,  $8 \times 8$  RASJA.

near-equilibrium patterns that migrated but did not change shape or size.

In tests in which turbulence was generated by the  $8 \times 8$  RASJA, the bed was fully covered by ripples approximately 4-6 hours after the jets were turned on, and the equilibrium state was achieved after 12-18 hours, depending on the strength of the turbulence. Tests with higher  $T_{on}$  saw faster ripple development than tests with lower  $T_{on}$ . In the  $16 \times 16$  RASJA, this process occurred much more rapidly, with intersecting ripples forming within minutes of turning on the jets and the entire bed covered with ripples in 4-6 hours.

Despite the clear pattern of the ripples observed in the tests with the  $8 \times 8$  RASJA, the organization of which seems to be a result of the square facility, it does not appear that the ripples originate at the walls or exist because of the physical enclosure of the tank. Along the walls, there are distinct wall-normal

ripples that extend into the tank before the orthogonal pattern forms, though observations show that incipient ripple growth does not begin at the walls. The turbulence within two integral length scales of the walls is not homogeneous as there is a boundary layer and weak upward return flow along the walls. Thus, it is not expected that the ripples along the walls follow the same pattern as the ripples in the interior of the tank. Indeed, the wall-attached ripples extend approximately two integral length scales before merging into orthogonal ripples. This is due to the transition to homogeneity and the no flux boundary condition at the wall that requires orthogonality.

In tests with the 16 x 16 RASJA, ripples evolved much more rapidly. Interestingly, wall-normal ripples were not consistently observed along all 4 walls of the tank, as shown in figure 6.9, for comparable levels of  $k$  as shown in figure 6.8. This emphasizes that the walls are not an essential starting point for ripple growth. A similar interior pattern was observed with intersecting ripples of relatively uniform spacing.

Tests were performed with the 8 x 8 RASJA in which the outermost and two outermost rings of jets in the 8 x 8 RASJA were not activated, thus eliminating the roles of the side walls in the experiment. In these cases, organized rippled patterns still emerged in the center of the facility, even in absence of the orthogonal ripples that were connected to the walls. More details are presented in Johnson (2012). The experiments with the 16 x 16 RASJA support the notion that walls are not required for ripples to emerge, as wall-normal ripples are not always present even when interior ripples were fully developed.

These tests also show that the vibrations generated by turning the jets on and off do not play a role in the ripple formation. Because the jet arrays are

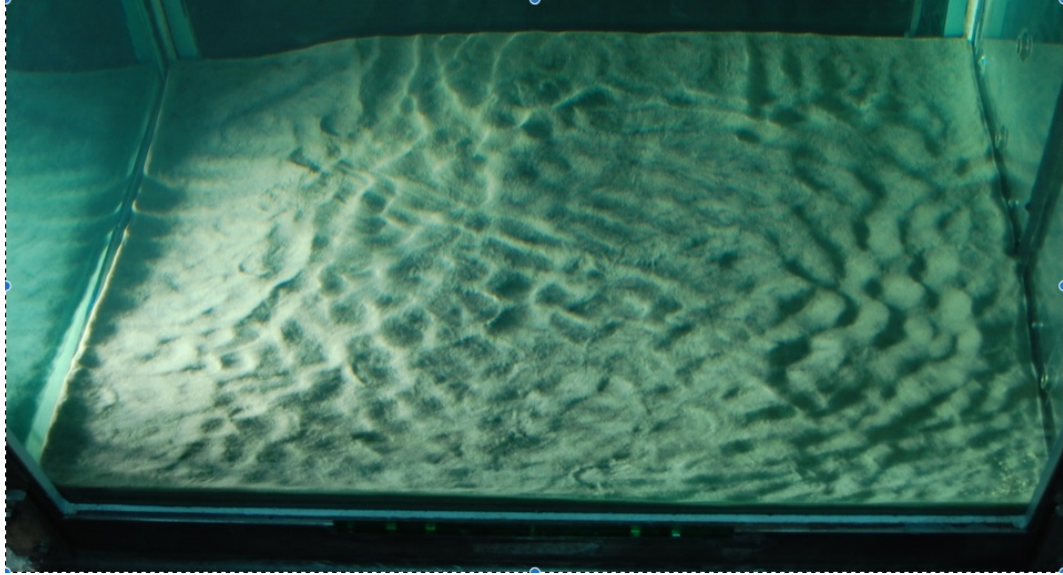


Figure 6.9: Resulting sand ripples after 6 hours.  $\Phi_{on} = 3.15\%$ ,  $T_{on} = 0.8$  s,  $16 \times 16$  RASJA.

mounted directly onto the frame of the tank, vibrations are relatively uniform across the entire facility and would therefore create similar patterns regardless of which jets were or were not active. In other words, running only the central  $4 \times 4$  core of jets should result in a fully-rippled bed if vibrations are the ripple generating mechanism. However, since ripples only evolve in the center of the tank during these experiments, vibrations seem an unlikely cause.

Additionally, we have considered the possible contributions of a tank seiche along the free surface and of vibrations resulting from the jets turning on and off. Wave gauge tests showed no noticeable peaks suggesting a seiche, as discussed in Johnson (2012). Thus we infer that the ripples are a result of the turbulence.

### 6.3.2 Ripple Spacing

To measure the ripple spacing,  $R$ , we use photographs taken once the equilibrium state was stable, approximately 12-18 hours after the inception of turbulence, such as that shown in figure 6.8. Working laterally, we measure the pixel to pixel location of each ripple crest in the homogeneous region. The pixel spacings are converted to distances knowing that the bed is 80 cm wide. We find that with increasing  $T_{on}$ , there is an increase in  $R$ .

Indeed, when comparing  $R$  to the metrics of the turbulence, we find a relationship between the integral length scale of the turbulence and the spacing of the ripple crests.  $R$  increases linearly with  $\mathcal{L}_m$ , as shown in figure 6.10. Although we performed experiments with only one type of sediment, we expect that additional parameters such as size and specific weight of the sediment would also come into play in this relationship. With the sediment used in these experiments, we obtain the relationship  $R = 2.92 + 0.17\mathcal{L}$  from the best fit line, which has an  $R^2$  value of 0.95.

### 6.3.3 Additional Comments on Bedforms

Although we observe a relationship between the turbulence and the lengthscale of the ripples, we are unable to fully explain the generation mechanisms for ripple formation. We know that suspension structures such as splats and vortices can affect transport of the ripples, as well as deepening or steepening ripple troughs or crests, respectively; however, it appears that such suspension is not required for transport. In lieu of measurements within the bed, visual observations of the bed do not show particle movement that would suggest fluidization

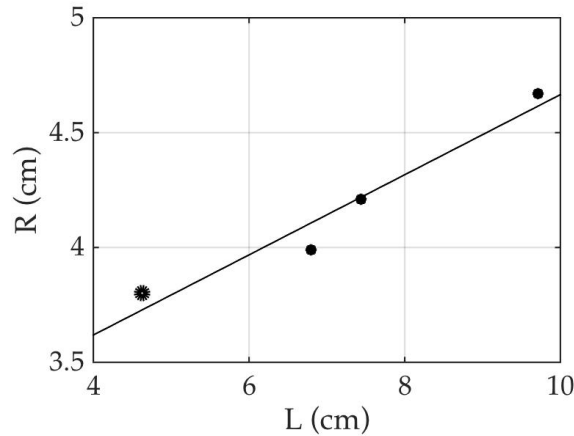


Figure 6.10: Relationship between sand ripple spacing and integral length scale. (\*) denotes tests with  $8 \times 8$  RASJA; (o) denotes tests with  $16 \times 16$  RASJA.

or dilation of the bed. Ripples seem to form via localized rolling of sand grains over small regions on the order of millimeters to centimeters, but these transport events are much weaker than splats.

It remains a possibility that pressure fluctuations above or within the bed could contribute to these sediment transport events, although we currently do not have measurements to support or negate this hypothesis. A dynamic pressure field above the bed would likely show similar correlation length scales as the integral length scale of the turbulence, due to the inextricably linked velocity fluctuations and dynamic pressure gradients. Spatial pressure gradients within the bed, as described in Musa et al. (2014), can reinforce ripple evolution, as the internal pressure field within a ripple induces upward seepage at the crest and a downward flux at the trough. Indeed, when examining the ripple fields produced with the  $8 \times 8$  RASJA at low levels of sediment suspension, implications of this type of phenomenon are apparent as coarse grained material ejected from the ripple is often found at the crests whereas dark, finer sediments

that may be pulled into the bed from the flow are found in the troughs. Despite this evidence, it is difficult to observe or record these phenomena occurring in real time.

In the experiments performed with the 16 x 16 RASJA, sediment suspension is much more frequent than with the 8 x 8 RASJA. There is competition between suspension-induced bed deformation and ripple formation, as energetic splats can extend several ripple lengths, alternately reinforcing or erasing the underlying ripple structure. Furthermore, ripples may be covered with mixtures of sand deposited from suspension events, resulting in less predictable distributions of coarse and fine sediments aligned on crests or troughs, respectively.

## CHAPTER 7

### BOUNDARY LAYER RESULTS - SEDIMENT BOUNDARY

Given the analysis methods and techniques used to explore the mean shear free turbulent boundary layer above a solid bed, we now report similar analyses of the mean shear free turbulent boundary above sediment boundaries for comparison. The sediment boundary introduces several levels of complexity. The boundary is porous, allowing for vertical flow to penetrate the bed. Local shear stresses and pressure fluctuations can induce sediment suspension, in which sand particles roll or creep along the bed, or are picked up from the bed and briefly entrained into the flow until they are brought to rest by gravity and friction. Sediment transport along the bed via creep or rolling resulting in bedforms is possible, even in absence of significant suspension. We explore each of these mechanisms through boundary layer comparisons and analysis of suspension and bed morphology. While other related phenomena, such as bed fluidization, drag on the fluid by suspended sediment, or organized pressure fields may also occur, we do not directly explore them in the context of the boundary layer, but instead mention outcomes related to their potential existence.

Because turbulence levels were found to be relatively independent of  $\Phi_{on}$  in the range selected, experiments above a sediment bed with the 8 x 8 RASJA were only performed for  $\Phi_{on} = 6.25\%$  with varying  $T_{on}$ . These experiments were performed above both flat and rippled sediment beds. With the 16 x 16 RASJA, we perform tests for  $\Phi_{on} = 3.1\%$  with varying  $T_{on}$ . In this chapter,  $T_{on}$  is restricted to range 0.8 s to 1.6 s, as has been presented previously. Due to the inconsistencies in results obtained above a rippled bed beneath the 16 x 16 RASJA, PIV data was only collected above nearly-flat sediment beds.

The turbulence is forced such that the bed is just beyond incipient motion, with low frequency suspension events and transport dominated by creep and some saltation in experiments with the 8 x 8 RASJA. Experiments with the 16 x 16 RASJA showed much higher levels of sediment suspension, by considering the frequency of events, quantity of suspended sediment, and strength of each event to transport sediment over significant distances. The increase in suspension with the 16 x 16 RASJA leads to considerable differences in the boundary layer profiles as compared to those with the 8 x 8 RASJA. Analysis is presently performed such that suspended sediment grains are treated the same as tracer particles.

## **7.1 Fluctuating Velocities and Turbulent Kinetic Energy**

### **7.1.1 Flat Sediment Boundary - 8 x 8 RASJA**

Here we consider the boundary layer formed when turbulence interacts with a flat boundary, comparing the impermeable glass plate bed to a permeable, weakly-mobile sediment bed. Looking at figure 7.1, there is no noticeable change in  $u'$  between a flat solid and flat sediment boundary. However, lower values of  $w'$  are obtained above a sediment bed, due to the permeability that allows penetration from bed-normal flows. Similarly, we observe a slight decrease in  $k$  considering the flat sediment bed compared to the flat solid bed, as shown in figure 7.2. Though the differences in  $k$  near the boundary are imperceptible, there is approximately a 5% reduction throughout the mixed region of the flow in the example case shown. In the comparable case with  $T_{on} = 8$  s, this decay is slightly more pronounced at 7%.

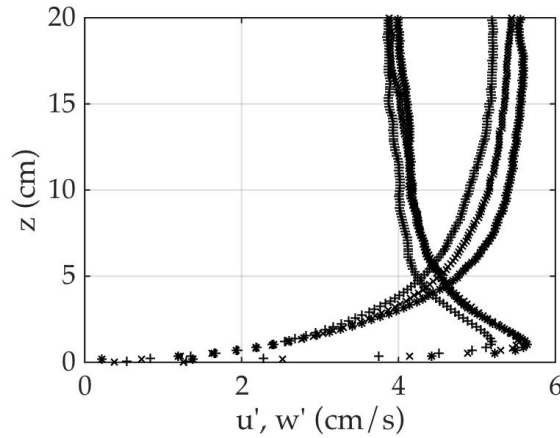


Figure 7.1: Profiles of  $u'$  and  $w'$  above solid (\*,  $\circ$ ), flat sediment ( $\times$ ,  $\diamond$ ), and rippled sediment (+,  $\square$ ) boundaries.  $\Phi_{on} = 6.25\%$ ,  $T_{on} = 4$  s, 8 x 8 RASJA.

### 7.1.2 Rippled Sediment Boundary - 8 x 8 RASJA

Both  $u'$  and  $w'$  are affected by the presence of bed ripples, compared to the flat solid or flat sediment bed. As shown in figure 7.1, there is a decrease in the strength of the horizontal turbulent velocity fluctuations throughout the entire water column in the FOV, due to the increased drag that results from the bed forms. Similarly,  $k$  is decreased throughout the entire water column by approximately 8% compared to the flat sediment bed in the case shown. A similar trend occurs in the  $T_{on} = 8$  s trial, with a reduction of 15 % between the sediment and flat boundaries.

### 7.1.3 Smooth Sediment Boundary - 16 x 16 RASJA

Experiments with sediment boundaries with turbulence generated by the 16 x 16 RASJA, even at small  $T_{on}$ , result in ripple development within minutes of

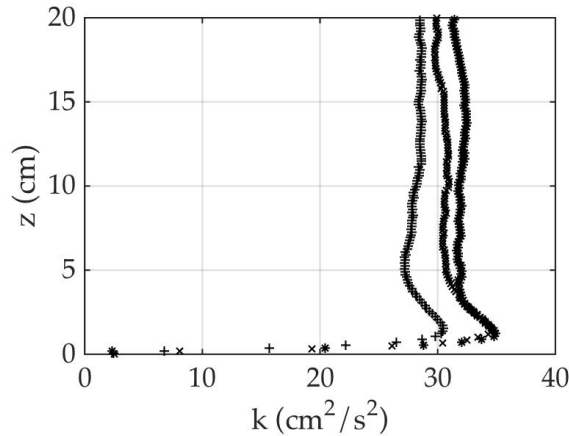


Figure 7.2: Profiles of  $k$  above solid (\*), flat sediment (x), and rippled sediment (+) boundaries.  $\Phi_{on} = 6.25\%$ ,  $T_{on} = 4$  s, 8 x 8 RASJA.

turning on the jets even at relatively low levels of jet activity. Thus, instead of a truly flat sediment bed, all of the trials were performed over shallow ripples. Interestingly, the opposite trend is observed in comparing solid and sediment boundaries. Significantly higher values of  $u'$ ,  $w'$ , and  $k$  are obtained above a sediment bed than a solid bed. Sample profiles are shown in figures 7.3 and 7.4, and this is consistent across all 5 cases of varying  $T_{on}$ . The shape between the profiles computed over solid and sediment beds is noticeably different, with less pronounced splats occurring over the sediment bed, as is evident in particular in the profiles of  $u'$  and  $k$ . The increase in  $u'$  and  $k$  from the top of the source layer to the top of the kinematic region is more gradual and lower in relative magnitude over sediment than over the solid glass boundary.

It appears that the increase in the turbulent kinetic energy is likely caused by the increased mobility and inertia of suspended sediment. By comparing one-sided spatial spectra  $G_{uu}$  and  $G_{ww}$  above both a solid glass and mobile sediment boundary, we see distinct differences in the energy levels at different wavenumbers. In figure 7.5, which shows a comparison of spectra at  $z = 11.9$  cm, where  $u'$

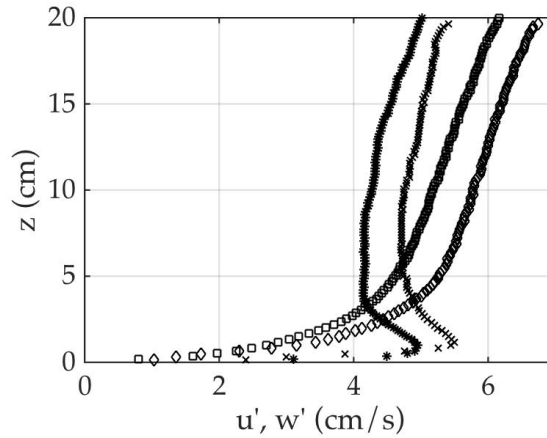


Figure 7.3: Profiles of  $u'$  and  $w'$  above solid ( $*$ ,  $\circ$ ) and sediment ( $\times$ ,  $\diamond$ ) boundaries.  $\Phi_{on} = 3.1\%$ ,  $T_{on} = 0.8$  s,  $16 \times 16$  RASJA.

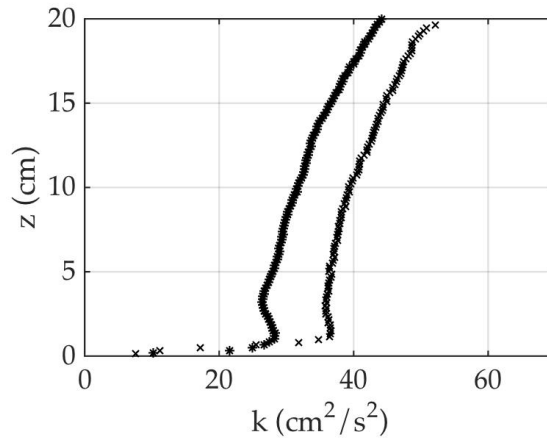


Figure 7.4: Profiles of  $k$  above solid ( $*$ ) and sediment ( $\times$ ) boundaries.  $\Phi_{on} = 3.1\%$ ,  $T_{on} = 0.8$  s,  $16 \times 16$  RASJA.

is relatively constant with  $z$ , we see that for low wavenumbers ( $\kappa < 1.5$  rad/cm),  $G_{uu, glass} > G_{uu, sand}$ . However, for  $\kappa > 3$  rad/cm, this trend is reversed and  $G_{uu, sand} > G_{uu, glass}$ . An approximate transition wavenumber of  $\kappa = 2$  rad/cm corresponds to coherent structures in the flow of approximately 3 cm in diameter, suggesting that clouds of suspended sediment may be causing an increase in the turbulence levels. As we saw in the previous chapter, this is consistent with observations of suspended clouds of sediment.

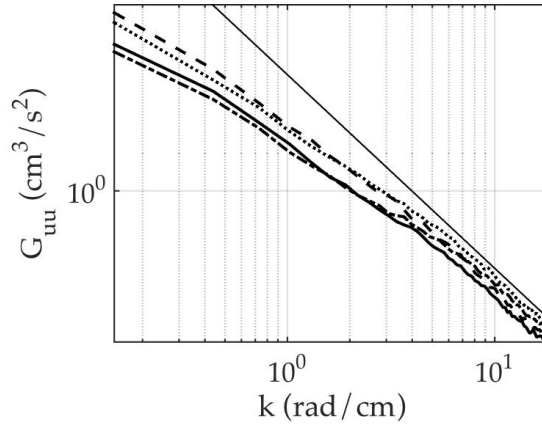


Figure 7.5: Spatial spectra comparison above solid and sediment boundaries. glass,  $G_{uu}$  - solid line; glass,  $G_{wv}$  - dashed line; sand,  $G_{uu}$  - dash-dotted line; sand,  $G_{wv}$  - dotted line.  $z = 11.9$  cm.  $\Phi_{on} = 3.1\%$ ,  $T_{on} = 0.8$  s,  $16 \times 16$  RASJA.

We observe this effect more clearly towards the bed, as shown in figure 7.6. Here, the crossing point at which  $G_{uu,sand}$  exceeds  $G_{uu,glass}$  occurs at a slightly smaller wavenumber of  $\kappa = 2$  rad/cm. The transition observed for  $G_{uu}$  happens at a smaller wavenumber than for  $G_{wv}$ , suggesting structures near the bed that are more stretched in the horizontal and restricted in the vertical, as is also consistent with observations of sediment suspension.

## 7.2 Dissipation

### 7.2.1 Sediment Boundary - $8 \times 8$ RASJA

We compute dissipation profiles via the direct method and we find that the presence of the sediment boundary, rather than a solid boundary, results in lower values of dissipation throughout the flow. The impact of the shape of the bound-

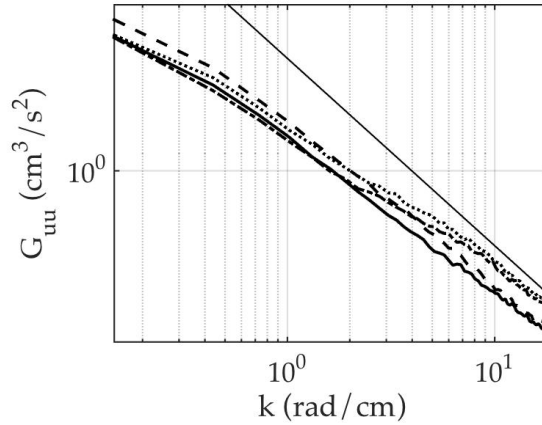


Figure 7.6: Spatial spectra comparison above solid and sediment boundaries. glass,  $G_{uu}$  - solid line; glass,  $G_{wv}$  - dashed line; sand,  $G_{uu}$  - dash-dotted line; sand,  $G_{wv}$  - dotted line.  $z = 4.0$  cm.  $\Phi_{on} = 3.1\%$ ,  $T_{on} = 0.8$  s,  $16 \times 16$  RASJA.

ary, rippled or flat, is again inconclusive, as different trials show different results whether the rippled boundary has higher or lower dissipation values than a flat boundary, as shown in figure 7.7. Given the results of reduced  $k$  in flows above a sediment bed, the reduction in  $\epsilon$  is not surprising. Sediment transport is infrequent in these experiments, and the sand acts as a penetrable porous, nearly stationary boundary, dampening turbulent velocity fluctuations relative to the solid impermeable boundary.

## 7.2.2 Sediment Boundary - $16 \times 16$ RASJA

We observe an increase in the dissipation rate when computed above a sediment boundary instead of a glass boundary in tests with the  $16 \times 16$  RASJA. An example of these results is shown in figure 7.8, in which it is clear that the dissipation rate is nearly doubled by changing from a solid to a sediment boundary. The slopes of the profiles are also noticeably different, with the dissipation above a

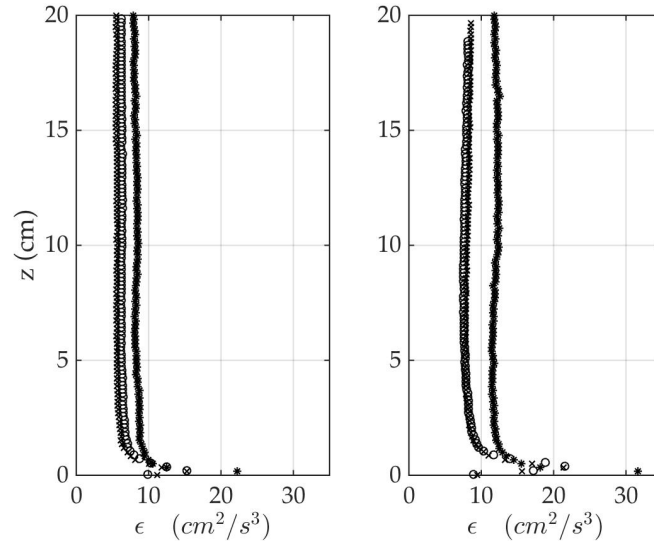


Figure 7.7: Profiles of dissipation above solid (\*), flat sediment (x), and rippled sediment (o) boundaries. Figure on left shows results for  $\Phi_{on} = 6.25\%$ ,  $T_{on} = 4$  s,  $8 \times 8$  RASJA. Figure on right shows results for  $\Phi_{on} = 6.25\%$ ,  $T_{on} = 8$  s,  $8 \times 8$  RASJA.

sediment bed more uniform with  $z$ .

Figures 7.5 and 7.6 show an increase in the spatial spectra for higher wavenumbers in the dissipation range. This is consistent with the increase in dissipation caused by suspended sediment structures generating fluid turbulence and hence dissipation at scales of the sediment clouds and smaller. Instead of a strict decay of  $\epsilon$  away from the RASJA, there is an additional source of turbulence that stirs the flow.

### 7.3 Integral Length Scale

As we explored in the previous chapter, the integral length scale is an important parameter in relating the turbulence to the spacing of the ripples. Because the

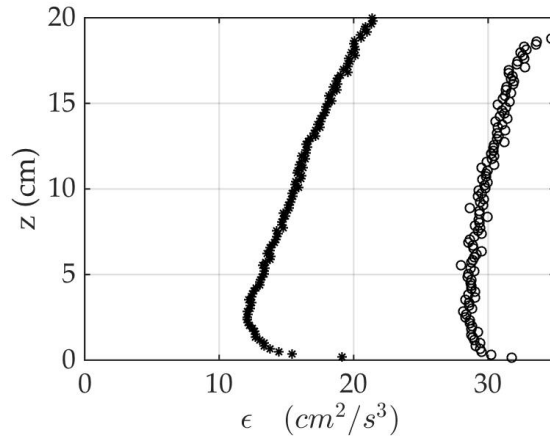


Figure 7.8: Dissipation profiles above solid (\*) and sediment (o) boundaries.  $\Phi_{on} = 3.1\%$ ,  $T_{on} = 0.8$  s,  $16 \times 16$  RASJA.

ripples induce drag and affect the strength of turbulent velocity fluctuations, we might expect to see similar changes in  $\mathcal{L}$  before and after the formation of ripples, if the ripples force coherent flow structures on the same spacing as the ripple crests. However, we find inconclusive results in the  $8 \times 8$  RASJA experiments, examples of which are shown in figure 7.9. It appears that  $\mathcal{L}$  is possibly sensitive to bed conditions, as there is variation in the integral length scale depending on the boundary condition. However, due to the inherent noise in this measurement, at present we cannot confidently identify a trend that relates  $\mathcal{L}$  to the three different boundary conditions considered.

Similarly, in experiments with the  $16 \times 16$  RASJA, we obtain results that suggest that the composition of the boundary does not significantly affect the integral length scale. Resulting values of the longitudinal and transverse integral length scales are shown in table 7.1.

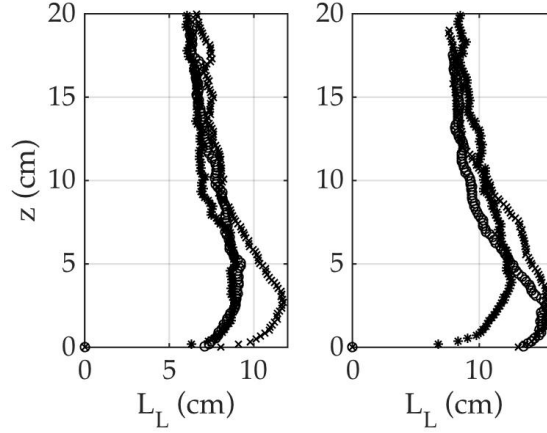


Figure 7.9: Profiles of longitudinal integral length scale above solid (\*), flat sediment (x), and rippled sediment (o) boundaries. Figure on left shows results for  $\Phi_{on} = 6.25\%$ ,  $T_{on} = 4$  s, 8 x 8 RASJA. Figure on right shows results for  $\Phi_{on} = 6.25\%$ ,  $T_{on} = 8$  s, 8 x 8 RASJA.

$\Phi_{on}$ (%)	$T_{on}$ (s)	glass - $\mathcal{L}_L$ (cm)	sand - $\mathcal{L}_L$ (cm)	glass - $\mathcal{L}_T$ (cm)	sand - $\mathcal{L}_T$ (cm)
3.1	0.8	4.63	4.43	3.59	3.44
3.1	1.0	5.19	4.73	3.83	3.46
3.1	1.2	4.65	4.45	3.57	3.87
3.1	1.4	4.52	5.22	4.41	4.49
3.1	1.6	4.75	6.01	4.53	4.13

Table 7.1: Comparison of integral length scale measurements above solid and sediment boundaries. 16 x 16 RASJA.

## CHAPTER 8

### CONCLUSIONS

#### 8.1 Summary

The facility we developed generates high Reynolds number turbulence via randomly actuated synthetic jet arrays that is horizontally homogeneous and nearly isotropic in the mixed region. We see strong intercomponent energy transfer and evidence of turbulent splats near the bed, characterized by the transition from  $w'$  to  $u'$ , with strong local shear and an increase in turbulent kinetic energy near the bed due to local pressure gradients above both solid and sediment boundaries. We are able to control the relative magnitudes of turbulence statistics such as  $u'$ ,  $w'$ ,  $k$ ,  $\varepsilon$ , and, importantly,  $\mathcal{L}$ , by altering the mean on-time in the jet-firing algorithm, and we are the first to show the ability to vary  $\mathcal{L}$  in this type of facility by changing the mean on-time in the jet-firing algorithm.

The results we observe have several distinct differences from prior facilities and theories that have been designed to study turbulence in a mean shear free environment. Whereas our results agree with the data in the moving bed studies of Thomas & Hancock (1977) and Hunt & Graham (1978) in the inviscid models when the flow measurement is farther than one integral length scale above the bed, these models and experiments do not show as energetic a boundary as we find in our experiments. It appears that the moving bed and source of energy by its motion may dampen potential splats, apparent in the discrepancies observed in turbulent kinetic energy and integral length scale profiles. This could also be a result of the significantly lower Reynolds numbers in the moving bed simulations than in our experimental facility.

Furthermore, because the aforementioned studies, in addition to RDT and DNS studies of Teixeira & Belcher (2000) and Perot & Moin (1995b), respectively, are time-dependent, it appears that our data more closely aligns with these studies at later time scales, when the forced turbulent flow has had time to respond to the presence of the solid boundary. This is indeed a quick transition, as is observed in figures 5.11 and 5.12, though the lack of collapse in figure 5.2 suggests that these models are limited in capturing fully developed turbulent boundaries.

In our analysis, we consider several methods for computing dissipation. Because several methods require isotropy, we evaluate the implications of these assumptions, which clearly break down at the bed. We are instead able to compute dissipation directly, and thus find that the longitudinal second-order structure function, though a commonly used robust method, underestimates the dissipation rate found in the direct method. With our estimate of dissipation, we provide additional estimates of the coefficients needed to compute dissipation via Eulerian frequency spectra, when low mean flows prevent the use of Taylor's frozen turbulence hypothesis for temporal measurements of turbulent flows.

Considering the remaining terms found in the turbulent kinetic energy balance, we see that dissipation, turbulent transport, and pressure likely play the greatest roles in the mean shear free turbulent boundary layer generated from homogeneous isotropic turbulence. Production is nearly zero in this flow, even at the boundary, due to the negligible mean flows in the facility. Despite such weak mean shear, we know that there are highly energetic local shear events at the bed, due to turbulent splats and intercomponent energy transfer, that make this type of facility and boundary layer of unique importance.

The turbulent splats, in particular, contribute to much of the sediment transport that is observed, both in sediment suspension and in ripple development. We also observe vortical sediment transport. While splats affect ripple migration, it appears that ripples are able to develop even in absence of sediment pick-up. We find a linear relationship between ripple spacing and the integral length scale of the turbulence, suggesting the ripples are indeed connected to the turbulence, a novel finding in the area of sediment transport.

We find that traditional methods of determining bed stress from mean viscous bed shear or Reynolds stress struggle to capture the energetics of this unique flow. Instead, intermittent and local stresses not represented by averages are what contributes to sediment pick-up. Instead, our characterization of Reynolds stresses in the boundary layer over short time scales better highlights the likelihood of local transient stresses to suspend sediment. By considering the strength of friction velocity in the tails of histograms of Reynolds stresses, we find that we exceed the critical friction velocity suggested by Shields to mobilize sand used in our experiments. Thus, this appears to be a promising method for understanding transport and suspension in a flow where the turbulence levels significantly outweigh the ability of the mean flows to generate bed stresses.

In comparing the turbulent boundary layer generated over a solid boundary to that above a sediment boundary, we observe difference results based on the energetics of the sediment. In experiments with the 8 x 8 RASJA, in which sediment suspension was infrequent and relatively small scale, the transition from a solid to sediment bed generally dampened the strength of turbulent velocity fluctuations. Specifically,  $w'$  decreased above a flat sediment bed compared

to a flat solid bed, due to the porosity of the bed. When the bed was rippled, both  $u'$  and  $w'$  decreased, due to increase drag on fluid motions. In experiments with the 16 x 16 RASJA, where sediment suspension was frequent and, at times, filled the entire FOV, the observed behavior was an increase in  $u'$ ,  $w'$ , and  $\varepsilon$ . We are able to attribute this increase in turbulence to the significant levels of sediment suspension, as increases in spatial spectra were observed on similar spatial scales as the suspension structures, suggesting that these structures serve as an additional source of turbulence from the bed, rather than a sink of turbulence observed above a solid or immobile sediment bed.

## 8.2 Future Directions

Beyond developing these two unique RASJAs to study boundary layers and compare solid and sediment boundaries in a mean shear free turbulent environment, there are several future directions this research can follow. As direct continuations of the present work, there is a need to better understand the pressure fields resulting from the generation of turbulence. Performing PIV at higher sampling rates would allow for the direct computation of spatial pressure gradients in the flow, if there is sufficient resolution in both space and time, even in absence of *in situ* pressure measurements. Furthermore, understanding pressure fluctuations within the bed would shed light on the role fluidization may play in sediment suspension or in ripple development. To support this work, repeating experiments with relatively low density particles such as ground walnut shells would likely result in a more fluidized bed with more chance for sediment pick-up, which may ultimately clarify the relative importance of the simultaneous physical processes that occur in sediment transport

and ripple development, as well as to elucidate the effect of specific weight on the processes of incipient motion and sediment pick-up. Alternately, studying sand with difference grain sizes would further develop the scaling relationship that determines ripple spacing.

In continuing to understand the feedback mechanisms that a mobile or rippled sediment bed may have on the flow, using particle tracking velocimetry (PTV) would be a valuable tool in distinguishing tracer particle motions from suspended grains of sand. Because suspended sediment is not truly passive, as it is inertial and is notably heavier than water, it is possible that entrained sediment imposes drag on the surrounding fluid. PTV can be used to independently identify sand grains so that the flow surrounding suspended sediment may be treated differently from turbulent flow in absence of suspension. Moreover, if sediment grains can be tracked via PTV at high temporal sampling frequencies, it may be possible to study the flow preceding suspension events to identify if critical stress events or coherent flow structures exist as a precursor to pick-up.

It is important to continue to understand the development of flows in random jet arrays, as this method of turbulence generation has recently grown in popularity to study mean shear free turbulence. Because much of the work in this field, present research included, considers constant turbulent forcing and a statistically stationary bed, it would be valuable to study the initial development of this boundary layer. Surely there is a very rapid transition to turbulence (*i.e.* within several seconds of turning the jets on). However, exploring the evolution to homogeneity and statistical equilibrium would be of value both in better understanding the facility and in applications to environmental flows in which a transient source of turbulence, such as a collapsing wave, may impinge

upon a boundary before the flow is well-mixed.

As one of the environmental applications of this work is to understand swash-generated turbulence, it would be fascinating to increase the turbulence levels in the facility so that they are on par with those observed in nearshore flows, in particular, with significant sediment transport. Comparisons between this experimental work and field work, which can be complicated by the interaction between turbulence and both oscillatory and mean flows, are critical to parameterizing models for sediment transport in energetic coastal zones. On a laboratory level, this could possibly be achieved by mounting a RASJA above a wave or current flume in order to control the level of turbulence relative to benthic turbulence in an oscillatory or shear flow, and to study the resulting changes in sediment pick-up observed from the distinctly different turbulence generating mechanisms.

## APPENDIX A - RASJA OPERATING CODES

### 8 x 8 RASJA m-files

The following scripts are used to run the two RASJAs. The first two scripts, `runjets.m`, and `pump_update_independent.m`, are slight adaptations of the codes developed by Evan Variano (Variano & Cowen 2008) to operate the 8 x 8 RASJA. Because the 8 x 8 RASJA is controlled in real time via a 96 channel digital output card, the function `pump_update_independent` is called every tenth of a second and a complete matrix of on-off states is not stored.

#### **runjets.m**

```
% This code will randomly fire 64 pumps using digital outputs
    through a
% board connected using a 96 channel digital output card (PCI-
    DIO96H) .
% This code was originally developed by Evan Variano with
% Professor Edwin Cowen.

% running parameters
N = 80; % the card thinks we are running 80 jets , because 17-32
    is empty
mean_on_time=30*ones(1,N); % Mean time jets on is 3 seconds
mean_off_time=210*ones(1,N); % Mean time jets off is 21 seconds
sigma_on_time=10*ones(1,N); % STD of jets being on is 1 seconds
```

```

sigma_off_time=70*ones(1,N); % STD of jets being off is 7
seconds

% set up the matrix of pump states' initial conditions
A=9+zeros(600,N); % 80 columns (for the 64 pumps) and 600 rows
for 60 seconds of buffer size.
% a value of 9 means pump hasn't chosen its on or off time yet
% initial state of each pump is off

A(1,:)=zeros(1,N);

for i=1:30000 %let randomization sort it all out
    A=pump_update_independent(A,mean_on_time,mean_off_time,
        sigma_on_time,sigma_off_time);
end

save ic A
load ic

% this matrix holds the values for right now and the near
future

% initialize Digital Output
dio=digitalio('mcc',0)
hwlines=addline(dio,0:(N-1),'out') % Add all 80 (64) output
channels

% run the time series. This will run a function "
pump_update_independent"

```

```

% in order to randomly generate different matrices to dictate
    which pumps
% are on and which are off. The timerfcn will mandate that this
    part of
% the code will run every .1 seconds. The matrix is converted
    into
% logicals in order to make it clear that the pump is either on
    or off.

set(dio, 'TimerFcn', 'A=pump_update_independent(A, mean_on_time,
    mean_off_time, sigma_on_time, sigma_off_time); a=logical(A
    (1,:)); putvalue(dio,a);')
set(dio, 'TimerPeriod', .1)
start(dio)
% stop(dio)

```

### **pump\_update\_independent.m**

```

% Original code developed by Evan Variano with Professor Edwin
    Cowen
% This function will be used as a part of the RunJets program.
    This code
% will generate random matrices that control the state of each
    pump. Each
% row in the matrix represents a tenth of a second so the on
    time for each
% pump will be represented by the number of rows that contain a
    '1' in each
% column.

```

```

function out = pump_update_independent(A,mean_on_time ,
    mean_off_time ,sigma_on_time , sigma_off_time)
if sigma_on_time>mean_on_time;
    beep;
    'error - sigma_on_time should be less than 3 x mean_on_time
    ';
    return;
end

```

```

% update procedure: for each pump, if the next step is going to
    be a 9, then
% choose an on or off time and fill in the corresponding number
    of next
% steps with zero or 1

```

```

% update the matrix
for i=1:256 %64 % go through each pump
    if(A(2,i)==9) % if next step is undefined
        if(A(1,i)==1) %if this pump is on right now
            offlength=round(normrnd(mean_off_time(i) ,
                sigma_off_time(i))); %choose an off time
            if offlength <1;
                offlength=1;
            end
            A(2:offlength+1,i)=0;
            % fill in this off time as the number of rows. the
                +1 will be
            % eliminated later and is only there for

```

```

        convenience
elseif(A(1,i)==0) %if pump is off right now;
    onlength=round(normrnd(mean_on_time(i),
        sigma_on_time(i))); %choose an on time
    if onlength < 1;
        onlength=1;
    end
    A(2:onlength+1,i)=1;
    % fill in this on time as the number of rows. the
    +1 will be
    % eliminated later and is only there for
    convenience
    end
end
end
end
% correct for the +1 in order to normalize the run times

B=A;
A(1:599,:) = B(2:600,:);
A(600,:) = 9;
out=A; % send this new matrix

```

## **16 x 16 RASJA - m-files to generate on-off states**

The function, `pump_update_independent`, is also used in the 16 x 16 RASJA system by simply editing the number of jets to 256. Because of the increase to 256 jets, we use an Arduino microcontroller to signal the on-off states. To do this, we build a complete matrix that stores the on-off states of all 256 jets for a

given period of time. This occurs in the third script, `Create_A_master.m`, which utilizes `pump_update_independent` at each time step to build a matrix for, in this case, a 40 minute trial.

Once the complete matrix is constructed, `Limit_jets_replacements.m` is used to verify that no more than 4 (or some limit set by the user) on a single board are on at a given time. If too many jets are on, the extra jets are turned off, and another board with fewer than 4 jets gains an extra active jet to compensate. Several functions were written to simplify this procedure. The coding of `Limit_jets_replacements.m` and the functions was primarily completed by Bonnie Powell.

In `Limit_jets_replacements.m`, the individual on-off states are converted to bytes in groups of 8 jets. Because each board utilizes two shift registers to transfer the bytes to the individual jets, the first 8 and last 8 jets on each board are treated separately.

## **Create\_A\_master.m**

```
% This script saves a matrix of "random" 1's and 0's based on
  inputs. The matrix
% saved should then be input into Limit_jets_replacements.m

N = 256; %number of jets; edit pump_update_independent to
  reflect correct N inputs
mean_on_time=30*ones(1,N);
mean_off_time=210*ones(1,N);
sigma_on_time=10*ones(1,N);
```

```

sigma_off_time=70*ones(1,N);

% set up the matrix of pump states ' initial conditions
% this matrix holds the values for right now and the near
    future
% a value of 9 means pump hasnt chosen its on or off time yet

A12=9+zeros(600,N); % 256 columns (for the pumps) and 600 rows
    for 60 seconds of buffer size.
%initial state of each pump is off
A12(1,:)=zeros(1,N);
for i=1:30000 %let randomization sort it all out
    A12=pump_update_independent(A12,mean_on_time,mean_off_time,
        sigma_on_time,sigma_off_time);
end

save ic12 A12
load ic12

%store actual matrix of on/off states for all time
for kk=1:24,000 % 40 minutes at 0.1s update
    A12=pump_update_independent(A12,mean_on_time,mean_off_time,
        sigma_on_time,sigma_off_time);
    a=logical(A12(1,:));
    A_master(kk,:) = a;
end

save ic12_master A_master kk

```

## Limit\_jets\_replacements.m

```
load ic12_master;
N=256; %number of jets
[nr nc]=size(A_master);
num_regs=(N/8)/2;

%powers of 2 used to calculate binary to decimal are stored in
    vector2
vector2 = [1, 2, 4, 8, 16, 32, 64, 128];
Asum = zeros(nr,num_regs*2);
threshold=4;%the maximum number of jets that can be on out of
    every set of 16
steps=nr;

% calculate the percentage of jets that are on at a time BEFORE
    changes and
% put in the matrix A_master_percentages column 1
A_master_percentages=zeros(steps,2);%initialize matrix
A_master_sums1=squeeze(sum(A_master,2)); %sum of A_master
    across each row
A_master_percentages(:,1)=A_master_sums1/nc; %divide by the
    number of rows to get percentage

% works for row 1
placement= 1:2:num_regs*2;

for row=1:1 %for the first row only
```

```

for shiftreg=1:num_regs %increment over every set of 16
jets

Atemp = A_master(row,( shiftreg -1)*16+1 : shiftreg*16);
%create a length 16 vector
count = NumOn(Atemp); %use NumOn function to find out
the number of jets on
p=find(Atemp==1)+((shiftreg*16)-16); %make a vector
with indices of jets that are on
% add something to it to make p
% increment from 1:nr, instead of 1:16
% y=randsample(p,length(p)); %create a vector of
randomly chosen, non-repeating, values from p

for k=1:(count-threshold)
if count>threshold
%use RowOff function to turn a jet off for
however long it
%was going to be on for, returns updated
%A_master and the last row needed to be turned
off
[r_off, col_off, A_master]=RowOff(row,p(k),
A_master);
len=r_off-row + 1;
[A_master, col_out]=Search(row, col_off, len,
A_master);
count=count-1; %make the count one less because
a jet was turned off
end

```

```

end

count=0; %reset the count for the next Atemp vector
Atemp_half1=Atemp(1:8);
Atemp_half2=Atemp(9:16);
Atemp_powers1 = Atemp_half1.*vector2; %multiply by the
    correct power of 2 for the individual 16
Atemp_powers2 = Atemp_half2.*vector2;
summm1=sum(Atemp_powers1); %add up all those numbers to
    get the decimal equivalent
summm2=sum(Atemp_powers2);
Asum(row, shiftreg*2-1) = summm1; %put in a matrix Asum
    the decimal number
Asum(row, shiftreg*2) = summm2;
end
end

% works for middle rows

for row=2:nr-1 %for the middle row only (excludes the first and
    last rows)

    for shiftreg=1:num_regs %increment over every set of 16
        jets

            Atemp = A_master(row, (shiftreg-1)*16+1 : shiftreg*16);
                %create a length 16 vector
            count = NumOn(Atemp); %use NumOn function to find out
                the number of jets on

```

```

p=find(Atemp==1)+((shiftreg*16)-16); %make a vector
    with indices of jets that are on

for k=1:length(p)
    %use Jet_preference function to see if the jet was
        previously turned off

    if count>threshold && Jet_preference(row,p(k),
        A_master)==1

        % use RowOff function to turn the preferenced
            jet off for
        % however long it was going to be on for ,
            returns updated
        % A_master and the last row needed to be turned
            off
        [r_off , col_off , A_master]= RowOff(row,p(k) ,
            A_master);
        len=r_off-row + 1;
        [A_master , col_out]=Search2(row, col_off , len ,
            A_master);
        count=count-1;
    end
end

% check to see you need to force more jet(s) off (in
    order)
% because no more preferenced ones exist and the count
    is

```

```

% still greater than the threshold

if count>5
    p_new=find(Atemp==1)+((shiftreg*16)-16); %make a
        new vector with indices of jets that are on

    for c=1:length(p_new)
        if count>threshold
            % use RowOff function to turn a jet off for
                however long it
            % was going to be on for , returns updated
                A_master
            % and the last row needed to be turned off
            [r_off,col_off,A_master]= RowOff(row,p_new(
                c),A_master);
            len=r_off-row + 1;
            [A_master,col_out]=Search2(row,col_off,len,
                A_master);
            count=count-1;
        end
    end
end

count=0; %reset the count for the next Atemp vector
Atemp_half1=Atemp(1:8);
Atemp_half2=Atemp(9:16);
Atemp_powers1 = Atemp_half1.*vector2; %multiply by the
    correct power of 2 for the individual 16
Atemp_powers2 = Atemp_half2.*vector2;

```

```

summm1=sum(Atemp_powers1); %add up all those numbers to
    get the decimal equivalent
summm2=sum(Atemp_powers2);
Asum(row, shiftreg*2-1) = summm1; %put in a matrix Asum
    the decimal number
Asum(row, shiftreg*2) = summm2;
end
end

% works for last row

for row=nr:nr %for the last row only
    for shiftreg=1:num_regs %increment over every set of jets
        Atemp = A_master(row, (shiftreg-1)*16+1 : shiftreg*16);
        %create a length 16 vector
        count = NumOn(Atemp); %use NumOn function to find out
            the number of jets on
        p=find(Atemp==1)+((shiftreg*16)-16); %make a vector
            with indices of jets that are on

        for k=1:length(p)
            if count>threshold && Jet_preference(row,p(k),
                A_master)==1
                % use LastRowOff function to turn off a jet ,
                    returns updated A_master
                [A_master]=LastRowOff(row,p(k),A_master);
                count=count-1;
            end
        end
    end
end

```

```

% check to see if you need to force more jet(s) off (in
    order)
% because no more preferenced ones exist and the count
    is
% still greater than the threshold

if count>threshold
    p_new=find(Atemp==1)+((shiftreg*16)-16);%make a new
        vector with indices of jets that are on

    for c=1:length(p_new)
        if count>threshold %use LastRowOff function to
            turn off a jet , returns updated A_master
            [A_master]=LastRowOff(row,p(k),A_master);
            count=count-1;
        end
    end
end

count=0; %reset the count for the next Atemp vector
Atemp_half1=Atemp(1:8);
Atemp_half2=Atemp(9:16);
Atemp_powers1 = Atemp_half1.*vector2; %multiply by the
    correct power of 2 for the individual 16
Atemp_powers2 = Atemp_half2.*vector2;
summm1=sum(Atemp_powers1); %add up all those numbers to
    get the decimal equivalent
summm2=sum(Atemp_powers2);

```

```

        Asum(row, shiftreg*2-1) = summm1; %put in a matrix Asum
            the decimal number
        Asum(row, shiftreg*2) = summm2;
    end
end

% calculate the percentage of jets that are on at a time AFTER
    changes and
% put in the matrix A_master_percentages column 2
A_master_sums2=sum(A_master,2); %sum of A_master across each
    row
% A_master_percentages(:,2)=A_master_sums2./nr; %divide by the
    number of rows to get percentage

save tester_03212016_40min_30s_3p_limit4

```

## **Jet\_preference.m**

```

% this function checks to see if the jet with a value of 1
    should be
% preferred to be turned off – in other words, the value in
    the same
% column but row directly above it must be a 0
% inputs– ind, row, A_master
% outputs– pref = 1 if it should be preferred, 0 if it should
    not be

function [pref] = Jet_preference(row,ind,A_master)

```

```

if A_master(row-1,ind)==0
    pref = 1;
else
    pref = 0;
end

```

### **LastRowOff.m**

```

%inputs the row and indice and big matrix and outputs an
    updated matrix
%this function turns off the jet at the specified row and
    indice , designed
%for use in the last row where the jet can not be on any longer

```

```

function [A_master] = LastRowOff(row,ind ,A_master)

```

```

A_master(row,ind)=0;

```

### **NumOn.m**

```

%inputs Atemp and outputs the number of jets that are on in
    that set of 8

```

```

function [count] = NumOn(Atemp)

```

```

count=0;

```

```

for l=1:length(Atemp)

```

```

    if Atemp(l)==1

```

```

        count = count + 1;
    end
end

```

## Replace.m

%this function replaces the specified vertical vector with 1's

```
function [A_master]=Replace(row,ind,length,A_master)
```

```
A_master(row:(row+length-1),ind)=1;
```

## RowOff.m

%turns off a vertical section of jets

%inputs the indice (column) of the jet to be turned off, the  
row it is

%in, and the large matrix, and outputs the row number where the  
jet is on

%until, the column the jets are being turned off in, and the  
updated matrix

```
function [r_off,col_off,A_master] = RowOff(row,ind,A_master)
```

```
rw=row;
```

```
[nr nc]=size(A_master);
```

```
for r=row:nr-1
```

```

A_master(r,ind) = 0;

if A_master(r+1,ind)==1
    A_master(r+1,ind) = 0;
    rw=rw+1;
    col_off=ind;
else
    col_off=ind;
    break;
end
end

r_off=rw;

```

## Search.m

```

%this function looks through each column (except for the set of
    16 the jet
%is currently in) in the the first row and finds a vertical
    vector of 0's
%of the specified length
%inputs -row, col, length, A_master
%outputs - a_vect_out (the vector of 0's) and col_out (the
    column
%in which the vertical vector is
%note: only use for first row, where Jet_preference is not
    needed

function [A_master, col_out]=Search(row, col, length, A_master)

```

```

[nr,nc]=size(A_master);%find the size of the regular A_master
A_master=[A_master,A_master];%make the A_master matrix twice as
    long by doubling it
[nr2,nc2]=size(A_master);%find the size of the larger A_master

if (row+length)<=nr

    %search all of the columns except the block of 16 the jet
    is currently in

    for c=ceil(col/16)*16+1:(ceil(col/16)*16+1)+nc

        if A_master(row,c)==0 %when a zero is found

            n=find(A_master(row:(row+length),c)==1); %create a
                vertical vector

            if sum(n) ==0 %if the vector is only zeros

                if c<=nc %if the column is within the
                    boundraries of the original matrix
                    col_out=c; %assign col_out
                else %if the column is larger than the original
                    matrix, subtract to account for that
                    col_out=c-nc;
                end

            %use the Replace function to replace the 0's

```

```

        with 1's
        [A_master]=Replace(row,col_out,length,A_master)
        ;
        disp('replaced')
        break; %once these are found, break out of the
            loop
    end
end
end

else %if you are near the end, don't do any replacements

    col_out=col; %just assign a value to col_out to make the
        function work
    disp('did not replace')

end

A_master=A_master(:,1:nc); %restrict A_master back to the
    original size

```

## Search2.m

```

%this function looks through each column (except for the set of
    8 the jet
%is currently in) in the the specified row (not the first row)
    and finds a vertical vector of 0's
%of the specified length and replaces them with 1's

```

```

%inputs–row, col (column), length (of the vector), A_master
%outputs– col_out (the column in which the vertical vector is)
    and A_master (updated)

function [A_master, col_out]=Search2(row, col, length, A_master)

[nr,nc]=size(A_master);%find the size of the regular A_master
A_master=[A_master,A_master];%make the A_master matrix twice as
    long by doubling it
[nr2,nc2]=size(A_master);%find the size of the larger A_master

if (row+length)<=nr

    %search all of the columns except the block of 16 the jet
    is currently in

    for c=ceil(col/16)*16+1:(ceil(col/16)*16+1)+nc

        if A_master(row,c)==0 %when a zero is found

            n=find(A_master(row:(row+length),c)==1); %create a
                vertical vector
            %use the Jet_preference function to determine if
                the vector has a 1 above or below it
            [pref] = Jet_preference(row,c,A_master);

            if sum(n) ==0 && pref==1 %if the vector is only
                zeros and does not have a 1 above or below it

```

```

%account for the doubling of the matrix
if c<=nc %if the column is within the
    boundaries of the original matrix
    col_out=c; %assign col_out
else %if the column is larger than the original
    matrix, subtract to account for that
    col_out=c-nc;
end

%use the Replace function to replace the 0's
    with 1's
[A_master]=Replace(row,col_out,length,A_master)
    ;
disp('replaced')
break; %once these are found, break out of the
    loop

end
end
end

else %if you are near the end, don't do any replacements
    col_out=col;%just assign a value to col_out to make the
        function work
    disp('did not replace')

end

A_master=A_master(:,1:nc); %restrict A_master back to the

```

original size

## **16 x 16 RASJA - Arduino/Matlab scripts to update jet states**

The following scripts update the jet on-off states in real time. The Arduino sketch is uploaded to the Arduino microcontroller and runs a continuous loop to wait for the signal sent by Matlab. Once the Arduino sketch is uploaded, the script `send_matrix_to_arduino` is run to transmit the bytes serially to the Arduino and to the control circuit boards.

### **sketch\_jul30\_fwrite\_notiming.ino**

```
// serially read in 32 bytes at a time to send to shift
// registers .
// currently updating every 0.1s in Matlab

//Define which pins will be used for the Shift Register control
int dataPin = 2;
int latchPin = 3;
int clockPin = 4;

#include <SPI.h>

void setup()
{
  SPI.setBitOrder(MSBFIRST);
  SPI.setDataMode(SPI_MODE0);
```

```

SPI.setClockDivider(SPI_CLOCK_DIV16);
SPI.begin();

//Configure each IO Pin
pinMode(dataPin, OUTPUT);
pinMode(latchPin, OUTPUT);
pinMode(clockPin, OUTPUT);

Serial.begin(115200);
delay(1000);

int seq
    [32]={0,0,0,0,0,0,0,0,0,0,0,0,0,0,0,0,0,0,0,0,0,0,0,0,0,0,0,0,0,0,0,0};

int timeElapsed = 2000;
int timeOld = 0;
int interval = 100;

void loop()
{
    Serial.flush();
    Serial.println('K');
    for (int i = 0; i<32; i++)
    {
        while(Serial.available() == 0);
        {
            seq[i] = Serial.read();
        }
    }
}

```

```

    }
    digitalWrite(latchPin , HIGH);
    digitalWrite(latchPin , LOW);
    for (int i = 0; i<32; i++)
    {
        SPI.transfer(seq[i]);
    }
    digitalWrite(latchPin , HIGH); //necessary line to transmit
    to board
}

```

### **send\_matrix\_to\_arduino.m**

```

% This is the code developed in Matlab to control an array of
    256 jets
% via the arduino with a stored matrix of the random jet states
.
% in order to zero all jets , can simply replace Asum as:
% Asum =
    [0,0,0,0,0,0,0,0,0,0,0,0,0,0,0,0,0,0,0,0,0,0,0,0,0,0,0,0,0,0];

% Jet states are supposed to update every 0.1s

load tester_03212016_40min_30s_3p_limit4
figure(1);
imagesc(Asum);
colorbar;

delete(instrfindall);

```

```

clear s
fclose('all')
s = serial('/dev/tty.usbmodem411','BaudRate',115200)
fopen(s)

Azero = Asum;
[nr nc]=size(Azero);
kko=nr; %nr change to 1000 for test
timestep = 0;
tstart = tic

while timestep < kko

    rx = fgets(s);
    timestep = timestep + 1;

    fwrite(s,Azero(timestep,1))
    fwrite(s,Azero(timestep,2))
    fwrite(s,Azero(timestep,3))
    fwrite(s,Azero(timestep,4))
    fwrite(s,Azero(timestep,5))
    fwrite(s,Azero(timestep,6))
    fwrite(s,Azero(timestep,7))
    fwrite(s,Azero(timestep,8))
    fwrite(s,Azero(timestep,9));
    fwrite(s,Azero(timestep,10));
    fwrite(s,Azero(timestep,11));
    fwrite(s,Azero(timestep,12));
    fwrite(s,Azero(timestep,13));

```

```

    fwrite(s,Azero(timestep,14));
    fwrite(s,Azero(timestep,15));
    fwrite(s,Azero(timestep,16));
    fwrite(s,Azero(timestep,17));
    fwrite(s,Azero(timestep,18));
    fwrite(s,Azero(timestep,19));
    fwrite(s,Azero(timestep,20));
    fwrite(s,Azero(timestep,21));
    fwrite(s,Azero(timestep,22));
    fwrite(s,Azero(timestep,23));
    fwrite(s,Azero(timestep,24));
    fwrite(s,Azero(timestep,25));
    fwrite(s,Azero(timestep,26));
    fwrite(s,Azero(timestep,27));
    fwrite(s,Azero(timestep,28));
    fwrite(s,Azero(timestep,29));
    fwrite(s,Azero(timestep,30));
    fwrite(s,Azero(timestep,31));
    fwrite(s,Azero(timestep,32));

    pause(0.03); %adjusted to meet Fs = 0.1Hz
end

tstop = toc(tstart)
t_avg = tstop./kko
timestep = 0;

fclose(s);
delete(instrfindall);

```

## APPENDIX B - MEDIAN SMOOTHING FILTER

The following script is edited slightly from a function originally downloaded from the Mathworks FileExchange. It is similar to the MATLAB function `medfilt2`, which performs a spatial smoothing based on the local median within a specified region of neighboring values in a 2-dimensional array. Because `medfilt2` propagates NaN values throughout the array, we prefer to use the function `mediannan.m`, which performs a spatial smoothing of non-NaN values, and it ignores the NaNs so as not to propagate them throughout the array and leaves them as placeholders.

### **mediannan.m**

```
function M = mediannan(A, sz)

if nargin < 2
    sz = 5;
end
if length(sz) == 1
    sz = [sz sz];
end
if any(mod(sz,2) == 0)
    error('kernel size SZ must be odd')
end
margin = (sz - 1) / 2;
AA = nan(size(A) + 2 * margin);
AA(1 + margin(1) : end - margin(1), 1 + margin(2) : end - margin(2)) = A;
```

```

[iB jB]=ndgrid(1:sz(1),1:sz(2));
is=sub2ind(size(AA),iB,jB);
[iA jA]=ndgrid(1:size(A,1),1:size(A,2));
iA=sub2ind(size(AA),iA,jA);
idx = repmat(iA(:).',numel(is),1) + repmat(is(:)-1,1,numel(iA));

B = sort(AA(idx),1);
j = any(isnan(B),1);
last = zeros(1,size(B,2))+size(B,1);
[trash last(j)]=max(isnan(B(:,j)),[],1);
last(j)=last(j)-1;

M = nan(1,size(B,2));
valid = find(~isnan(A(:).')); % <- Simple check on A
mid = (last(valid)+1)/2;
i1 = sub2ind(size(B),floor(mid),valid);
i2 = sub2ind(size(B),ceil(mid),valid);
M(valid) = 0.5*(B(i1) + B(i2));
M = reshape(M,size(A));

end

```

## BIBLIOGRAPHY

- [1] G. Bellani and E.A. Variano. Homogeneity and isotropy in a laboratory turbulent flow. *Experiments in Fluids*, 55, 2014.
- [2] B.H. Brumley and G.H. Jirka. Near-surface turbulence in a grid-stirred tank. *Journal of Fluid Mechanics*, 183:235–263, 1987.
- [3] P. Burattini, P. Lavoie and R.A. Antonia. On the normalized turbulent energy dissipation rate. *Physics of Fluids*, 17, 2005.
- [4] A.H. Clark, M.D. Shattuck, N.T. Ouellette, and C.S. O’Hern. Onset and cessation of motion in hydrodynamically sheared granular beds. *Physical Review E*, 92, 2015.
- [5] E.A. Cowen and S.G. Monismith. A hybrid digital particle tracking velocimetry technique. *Experiments in Fluids*, 22:199–211, 1997.
- [6] E.A. Cowen, I.M. Sou, P.L. Liu, and B. Raubenheimer. Particle image velocimetry measurements within a laboratory-generated swash zone. *Journal of Engineering Mechanics*, 129(10):1119–1129, 2003.
- [7] J.O. Dabiri, S. Bose, B. Gemmeli, S.P. Colin, and J.H. Costello. An algorithm to estimate unsteady and quasi-steady pressure fields from velocity field measurements. *The Journal of Experimental Biology*, 217:331–336, 2014.
- [8] J. de Jong, L. Cao, S.H. Woodward, J.P.L.C. Salazar, L.R. Collins, and H. Meng. Dissipation rate estimation from piv in zero-mean isotropic turbulence. *Experiments in Fluids*, 46:499–515, 2009.
- [9] P. Doron, L. Bertuccioli, J. Katz, and T.R. Osborn. Turbulence characteristics and dissipation estimates in the coastal ocean bottom boundary layer from piv data. *Journal of Physical Oceanography*, 31:2108–2134, 2000.
- [10] B. Efron and R. Tibshirani. *An introduction to the bootstrap*. Chapman and Hall, 1993.
- [11] D.L. Foster, A.J. Bowen, R.A. Holman, and P. Natoo. Field evidence of pressure gradient induced incipient motion. *Journal of Geophysical Research*., 111, 2006.

- [12] E.J. Hopfinger and J.-A. Toly. Spatially decaying turbulence and its relation to mixing across density interfaces. *Journal of Fluid Mechanics*, 78(1):155–175, 1976.
- [13] J. Hunt and J. Graham. Free-stream turbulence near plane boundaries. *Journal of Fluid Mechanics*, 84:209–235, 1978.
- [14] B.A. Johnson. Turbulent boundary layers and sediment resuspension in the absence of mean shear. Master’s thesis, Cornell University, 2012.
- [15] E. Kit, J.S. Fernando, and J.A. Brown. Experimental examination of eulerian frequency spectra in zeromeanshear turbulence. *Physics of Fluids*, 7:1168–1170, 1995.
- [16] Q. Liao and E.A. Cowen. An efficient anti-aliasing spectral continuous window shifting technique for piv. *Experiments in Fluids*, 38:197–208, 2005.
- [17] H. Makita. Realization of a large-scale turbulence field in a small wind tunnel. *Fluid Dynamics Research*, 8:53–64, 1991.
- [18] T. McDougall. Measurements of turbulence in a zero-mean-shear mixed layer. *Journal of Fluid Mechanics*, 94(3):409–431, 1979.
- [19] S.P. McKenna. *Free-surface turbulence and air-water gas exchange*. PhD thesis, Massachusetts Institute of Technology Woods Hole Oceanographic Institution, 2000.
- [20] S.P. McKenna and W.R. McGillis. Observations of flow repeatability and secondary circulation in an osillating grid-stirred tank. *Physics of Fluids*, 16(9):3499–3502, 2004.
- [21] P. Medina, M.A. Sanchez, and J.M. Redondo. Grid stirred turbulence: Applications to the initiation of sediment motion and lift-off studies. *Physics and Chemistry of the Earth (B)*, 26(4):299–304, 2001.
- [22] R.A. Musa, S. Takarrouht, M.Y. Louge, J. Xu, and M.E. Berberich. Pore pressure in a wind-swept rippled bed below the suspension threshold. *Journal of Geophysical Research: Earth Surface*, 2014.
- [23] L. Mydlarski and Z. Warhaft. On the onset of high-reynolds-number grid-generated wind tunnel turbulence. *Journal of Fluid Mechanics*, 320:331–368, 1996.

- [24] Y.-H. Pao. Structure of turbulent velocity and scalar fields at large wavenumbers. *Physics of Fluids*, 8(6):1063–1075, 1965.
- [25] Krogstad P.-A. Pearson, B.R. and W. van de Water. Measurements of the turbulent energy dissipation rate. *Physics of Fluids*, 14(3):1288–1290, 2002.
- [26] A. Perez-Alvarado, L. Mydlarski, and S. Gaskin. Effect of the driving algorithm on the turbulence generated by a random jet array. *Experiments in Fluids*, 57(20), 2016.
- [27] B. Perot and P. Moin. Shear-free turbulent boundary layers. part 1. physical insights into near-wall turbulence. *Journal of Fluid Mechanics*, 295:199–227, 1995a.
- [28] B. Perot and P. Moin. Shear-free turbulent boundary layers. part 2. new concepts for reynolds stress transport equation modelling of inhomogeneous flows. *Journal of Fluid Mechanics*, 295:229–245, 1995b.
- [29] N. Peters. The turbulent burning velocity for large-scale and small-scale turbulence. *Journal of Fluid Mechanics*, 384:107–132, 1999.
- [30] S.B. Pope. *Turbulent Flows*. Cambridge University Press, 2000.
- [31] J.M. Redondo, X. Durrieu de Madron, P. Medina, M.A. Sanchez, and E. Schaaff. Comparison of sediment resuspension measurements in sheared and zero-mean turbulent flows. *Continental Shelf Research*, 2001.
- [32] H. Rouse and J. Dodu. Diffusion turbulente a travers une discontinuite de densite. *Houille Blanche*, 10:522–532, 1955.
- [33] M.A. Sanchez and J.M. Redondo. Observations from grid stirred turbulence. *Applied Scientific Research*, 59:243–254, 1998.
- [34] P.C. Sinclair. General characteristics of dust devils. *Journal of Applied Meteorology*, 8:32–45, 1968.
- [35] P.R. Spalart. Direct simulation of a turbulent boundary layer up to  $r = 1410$ . *Journal of Fluid Mechanics*, 187:61–98, 1988.
- [36] M.A.C. Teixeira and S.E. Belcher. Dissipation of shear-free turbulence near boundaries. *Journal of Fluid Mechanics*, 422:167–191, 2000.

- [37] M.A.C. Teixeira and C.B. da Silva. Turbulence dynamics near a turbulent/non-turbulent interface. *Journal of Fluid Mechanics*, 695:257–287, 2012.
- [38] H. Tennekes. Eulerian and lagrangian time microscales in isotropic turbulence. *Journal of Fluid Mechanics*, 67:561–567, 1975.
- [39] N.H. Thomas and P.E. Hancock. Grid turbulence near a moving wall. *Journal of Fluid Mechanics*, 82:481–496, 1977.
- [40] S.M. Thompson and J.S. Turner. Mixing across an interface due to turbulence generated by an oscillating grid. *Journal of Fluid Mechanics*, 67(2):349–368, 1975.
- [41] C.H. Tsai and W. Lick. A portable device for measuring sediment resuspension. *Journal of Great Lakes Research*, 12(4):314–321, 1986.
- [42] J.S. Turner. The influence of molecular diffusivity on turbulent entrainment across a density interface. *Journal of Fluid Mechanics*, 33:639–656, 1968.
- [43] T. Uzkan and W.C. Reynolds. A shear-free turbulent boundary layer. *Journal of Fluid Mechanics*, 28:803–821, 1967.
- [44] L.C. van Rijn. Sediment transport, part i: Bed load transport. *Journal of Hydraulic Engineering*, 110:1431–1456, 1984.
- [45] E.A. Variano. *Measurements of gas transfer and turbulence at a shear-free turbulent air-water interface*. PhD thesis, Cornell University, 2007.
- [46] E.A. Variano, E. Bodenschatz, and Cowen E.A. A random synthetic jet array driven turbulence tank. *Experiments in Fluids*, 37:613–615, 2004.
- [47] E.A. Variano and E.A. Cowen. A random-jet-stirred turbulence tank. *Journal of Fluid Mechanics*, 604:1–32, 2008.
- [48] E.A. Variano and Cowen E.A. Turbulent transport of a high-schmidt-number scalar near an air-water interface. *Journal of Fluid Mechanics*, 731:259–287, 2013.
- [49] T. von Karman. Mechanische Ähnlichkeit und turbulenz. *Nachrichten von der Gesellschaft der Wissenschaften zu Goettingen, Mathematik(5)*:58–76, 1930.

- [50] J. Westerweel. Efficient detection of spurious vectors in particle image velocimetry data. *Experiments in Fluids*, 16:236–247, 1994.